PhD dissertation by

Adur Lagunas Tabar

Supervisor:

Carlos Del Río Bocio

Application of Visual Hyperacuity to Imaging and Antenna Systems

Thesis submitted for the degree of Doctor of Philosophy in Telecommunication Engineering

Doctoral programme: Communications Technology

Universidad Pública de Navarra

Departamento de Ingeniería Eléctrica y Electrónica

Pamplona, 2017

Ezina, ekinez egina.

Universidad Pública de Navarra
Nafarroako Unibertsitate Publikoa

Agradecimientos

Desde estas líneas, me gustaría agradecer a toda la gente que de alguna u otra forma me ha acompañado en el camino recorrido para la realización de esta tesis doctoral.

En primer lugar, dar las gracias a Carlos por estar siempre ahí, por tu inagotable fuente de ideas, por la motivación aportada, por hacer de los problemas nuevas oportunidades y, en general, por tu ayuda y apoyo incondicional.

A Oier, por ser parte del inicio de este viaje que nos ha llevado hasta donde estamos, por aportar siempre diferentes puntos de vista, por todo el trabajo realizado y por echarme una mano siempre que ha hecho falta. Mila esker!

A todos los compañer@s de la universidad que han compartido cafés, pintxos, comidas y demás momentos durante todo este tiempo: gracias por hacer que seguir caminando fuera más fácil, más agradable y tuviera mucho más sentido.

A mi familia y amigos que, aunque nunca han sabido qué estaba haciendo exactamente, no han dejado de confiar en mí, escucharme y darme ánimos siempre que ha hecho falta.

Aita eta ama, mila esker nigan beti sinesteagatik eta emandako laguntza guztiarengatik.

Eskerrik asko, bihotz-bihotzez.

upna

Universidad Pública de Navarra
Nafarroako Unibertsitate Publikoa

Abstract

The Human Visual System carries out multiple tasks, such as focusing objects at different distances or capturing high dynamic range images. Nevertheless, the most remarkable function is connected with the high-resolution images it can generate thanks to visual hyperacuity: the capability of the human eye to resolve details beyond the acuity defined by the number, size and distribution of photoreceptors.

Even though it may at first seem a complex scheme, the visual system shows an impressive performance based on a simple architecture and obtains high-resolution images starting from a limited number of sensors. The main hypothesis of this research work is that the diffraction introduced by the optical system of the human eye could have a fundamental role in achieving visual hyperacuity.

The implementation of the visual hyperacuity concept may be of great interest in many technological fields, such as imaging or antenna systems, where the resolution is an important matter. This idea is of particular relevance for the systems working in the terahertz frequency range, where there exist technological constraints to use a large number of sensors. Besides, the achievement of high angular resolutions in antenna systems usually involves the use of large size devices which can generate diverse problems. The application of the visual hyperacuity enables the use of smaller aperture antennas without a meaningful loss in terms of angular resolution.

This doctoral thesis presents a method that aims to simulate and implement the visual hyperacuity in the human eye by introducing of a controlled distortion to improve the final resolution of images or signals when the number of available sensors is limited. Likewise, a detailed study is developed, in order to show its potential and the possibilities of the method for imaging applications and antenna systems.

upna

Universidad Pública de Navarra
Nafarroako Unibertsitate Publikoa

Resumen

El Sistema Visual Humano es capaz de llevar a cabo múltiples tareas, tales como enfocar objetos a diferentes distancias u obtener imágenes con un amplio rango dinámico. Sin embargo, la función más impresionante está relacionada con las imágenes de alta resolución que es capaz de generar gracias a la hiperagudeza visual: la capacidad del ojo humano de resolver detalles más allá de la agudeza definida por el número, el tamaño y la distribución de los fotorreceptores.

Aunque en un principio pueda parecer complicado, el sistema visual está basado en una arquitectura relativamente sencilla y obtiene imágenes de alta resolución partiendo de un número limitado de sensores. La hipótesis principal de este trabajo de investigación se basa en que la difracción introducida por el sistema óptico del ojo humano desempeña un papel fundamental en la obtención de la hiperagudeza visual.

La implementación del concepto de la hiperagudeza resulta de gran interés para diversas aplicaciones tecnológicas, como los sistemas de captación de imágenes o antenas, donde la resolución es un aspecto importante. Esta idea tiene especial relevancia para los sistemas que trabajan en el rango de frecuencias de los terahercios, donde existen limitaciones tecnológicas para utilizar un elevado número de sensores. Por otro lado, la obtención de altas resoluciones angulares en los sistemas de antenas suele implicar el uso de dispositivos de grandes dimensiones que pueden generar problemas de diferente naturaleza. La aplicación de la hiperagudeza visual posibilita el uso de antenas con aperturas menores sin suponer una significante pérdida en términos de resolución angular.

En esta tesis doctoral se presenta un método que pretende simular e implementar la hiperagudeza visual del ojo humano mediante la introducción de una distorsión controlada que mejora la resolución final de las imágenes o señales cuando se dispone de un limitado número de sensores. Asimismo, se desarrolla un estudio cuyo objetivo principal es mostrar su potencial y las posibilidades que este método ofrece para aplicaciones relacionadas con sistemas de imágenes y antenas.

List of Figures

List of Tables

Universidad Pública de Navarra
Nafarroako Unibertsitate Publikoa

Acronyms

APS	Active-Pixel Sensor
BTTB	Block Toeplitz with Toeplitz Blocks
BW$_{-3dB}$	3 dB Beamwidth
CCD	Charge-Coupled Device
CFA	Color Filter Array
CMOS	Complementary Metal-Oxide Semiconductor
DFT	Discrete Fourier Transform
DSLR	Digital Single-Lens Reflex
DSP	Digital Signal Processing
FFT	Fast Fourier Transform
FOV	Field of View
FT	Fourier Transform
HDR	High Dynamic Range
HDRI	High Dynamic Range Imaging
HR	High Resolution
HVS	Human Visual System
LDR	Low Dynamic Range
LPF	Low-Pass Filter
LR	Low Resolution
LTI	Linear Time-Invariant
MAR	Minimum Angle of Resolution
MSE	Mean Squared Error
PSF	Point Spread Function
PSNR	Peak Signal-to-Noise Ratio
SAR	Synthetic Aperture Radar
SNR	Signal-to-Noise Ratio
SR	Super-Resolution
SVD	Singular Value Decomposition
TSVD	Truncated Singular Value Decomposition

Index of Contents

Introduction

Motivation and Objectives

It is widely known that the human eye is able to carry out many impressive functions: it presents a high dynamic range with a high sensitivity in low light conditions and avoiding saturation when working under strong lighting conditions; it can focus objects at different distances without any apparent difficulty; but, the most remarkable characteristic is the high-resolution images it can generate. This performance is obtained thanks to visual hyperacuity, which is the capability of the human visual system to resolve details beyond the acuity defined by the number, size and distribution of photoreceptors. In other words, it could be said that thanks to visual hyperacuity, the human eye outperforms artificial imaging systems with comparable optical and sensor characteristics.

The phenomenon of hyperacuity was discovered many years ago, but there are multiple different theories and approaches that attempt to explain it. From our point of view, even though it may at first seem a complex scheme, the visual system shows an impressive performance based on a simple architecture and obtains high-resolution images starting from a considerably low number of sensors. The main hypothesis of this research work is based on the assumption that the diffraction introduced by the optical system of the human eye could have a fundamental role in achieving visual hyperacuity.

The application of the visual hyperacuity concept in other technological fields may be of high interest since it can provide diverse advantages and benefits. One of the most obvious and direct area of application is oriented to imaging systems and technologies, where the resolution of images is a matter of great importance. In most cases, the maximum resolution that these systems can achieve is defined by the number, size and separation of the sensors. Nevertheless, there exist technological limits when reducing the size of the sensors endlessly and, in some instances, it is not possible to use a high number of sensors. Therefore, breaking the link between the number of sensors and the final image resolution of a system could be particularly interesting.

Besides, in connection with antenna systems, the achievement of high angular resolutions usually involves the use of antennas with large apertures, which result in antenna systems of considerable dimensions. The use of so oversized devices can generate challenges in relation to weight, power supply or mechanical scanning difficulties, for example, that need to be considered at the design, implementation and construction phases, but also during its operation lifetime. The application of visual hyperacuity concepts to antenna systems could significantly relax these problems and constraints, because it is possible to improve the angular resolution by means of post processing techniques that would allow the use of less directive—smaller—antenna systems.

Based on the above described principal hypothesis, the general purpose of this thesis is to develop a method that aims to explain and simulate the visual hyperacuity of the human eye, while suggesting some of its possible technological applications. Based on this general objective, more specific and concrete goals have been generated:

- Design, implement and test a method which takes advantage of the introduction of a controlled diffraction to improve the final resolution of signals and images.
- Compare the humane eye against conventional imaging devices, finding the most remarkable similarities and differences in relation to the optical system and sensors.
- Describe the possible benefits of diffraction to achieve high-resolution signals and images when the number of available sensors or samples is reduced, far from being a limiting factor.
- Explain and demonstrate the advantages of the application of the visual hyperacuity simulation method to imaging systems in general and THz imaging more specifically.
- Analyze the application of the visual hyperacuity simulation method to improve the angular resolution of antenna systems and its associated technological benefits, such as the reduction of the antenna size or the decrease of the required sampling rate.

By meeting these objectives, this research work aims to bring new points of view and fresh approaches in relation with the design, the implementation and the main characteristics of imaging and antenna systems when it comes to signal or image resolution.

Thesis Organization

The structure of the document is organized in five main chapters which contain the logical evolution of the research work carried out. Due to the multidisciplinary nature of the thesis, each chapter will have its own state of the art and introduction, but at the same time, they are linked coherently in a progressive way.

The first chapter is devoted to describing the anatomy and physiology of the human eye, mainly focusing on the optical system and the photoreceptors (cones and rods), for subsequent comparison with conventional imaging systems. Afterwards, the concept of visual hyperacuity is introduced to conclude with the principal hypothesis of this investigation work: the diffraction introduced by the optical system of the human eye could play a key role in achieving visual hyperacuity.

Chapter 2 can be considered one of the most important section of this thesis, for the reason that it describes the visual hyperacuity simulation method in detail, emphasizing different aspects of each step involved in the proposed scheme: diffraction, sampling and the inverse problem. Finally, the chapter concludes with some tests based on the previously described method.

The following chapter covers the potentials of the visual hyperacuity for imaging systems and applications. First of all, some of the most relevant imaging techniques are described, such as Super-Resolution or High Dynamic Range Imaging, relating them with the hyperacuity simulation method. Then, the emerging applications of THz imaging are described, explaining how hyperacuity could help to overcome many current technological limitations and difficulties. The last sections of the chapter describe two implementations of the method: the first approach based on a local kernel function and, the other, a methodology based on Fourier Transforms.

Chapter 4 is oriented to analyze the application of visual hyperacuity to antenna systems, mainly connected with the angular resolution. It aims to examine the possibility of reducing the aperture and, therefore, the size of a given antenna, as well as the possibility of decreasing the sampling rate of the system without a significant loss of angular resolution.

The last chapter brings together the most important conclusions and lessons learned from the development of this research work and makes some suggestions for future work and research lines.

Finally, the document closes with an appendix that provides some tests of the visual hyperacuity simulation method, from the modification of multiple parameters to the application of different deconvolution methods.

upna

Universidad Pública de Navarra
Nafarroako Unibertsitate Publikoa

Chapter 1

The Human Eye. Visual Hyperacuity

upna

Universidad Pública de Navarra
Nafarroako Unibertsitate Publikoa

1.1. Introduction

The visual perception is the ability of humans and other animals to generate and interpret colored and moving images. This basic physiological capacity is carried out by the visual system and mainly thanks to a sense organ: the human eye. Despite the apparent complexity of the eye when analyzing its anatomy and physiology, it operates in a relatively simple way: the light enters the eye through an aperture (the pupil) and an optical lens system (the cornea and crystalline) responsible for projecting it over the retina where photoreceptors (cones and rods) are placed. The image projected over these sensory cells is sent in the form of electrical signals to the brain where the visual perception is generated.

Given this main function, the human visual system can be considered a biological imaging system totally comparable with conventional imaging devices, such as digital cameras with CCD or CMOS sensors. On the basis of this comparison, it can be said that the human eye and digital cameras have many similarities when analyzing the structure of the optical system, RGB-type color sensors or peak sensor densities. However, the eye largely outperforms digital cameras with similar optical and sensor characteristics when evaluating features related to sensitivity, dynamic range or angular resolution.

Among many others, the most impressive function of the human eye is the high-resolution images it can obtain. This feature is known as visual hyperacuity, which can be defined as the capability of the eye to resolve details beyond the acuity defined by the number, size and distribution of photoreceptors. Even if hyperacuity has been known for a long time, there are significant differences when trying to explain how it is achieved, existing multiple explanations and complex approaches. Nevertheless, our central hypothesis is based on a simple scheme: the diffraction introduced by the optical system of the human eye plays a key role in achieving visual hyperacuity.

1.2. Anatomy and Physiology of the Human Eye

The eye is the vital part of the human body sensible to light, a specialized sense organ capable of receiving visual images which are carried to the brain. In short, it allows vision, one of the most fundamental of our senses, and generates moving, colored and three dimensional images.

The eye is fitted with an auxiliary structure for its correct performance [1], formed by diverse elements: the orbit is a cavity of the scull which encloses the eye to protect it from mechanical injury; the eyelids are responsible for remaining the front surface of the eyeball (the cornea) moist and they also have an additional function of preventing injuries from foreign objects; the conjunctiva is an outer covering and helps lubricate the eye by producing mucus and tears, although less than the lacrimal glands, which create secretions to keep the eye humid. The eye movement mechanism is governed by six extraocular muscles inserted into the sclera: four rectus muscles—superior, inferior, medial and lateral—and the superior and inferior oblique muscles (see Figure 1.1). These muscles produce movements to rotate the eyeball in orbits, while allowing the image to be focused on the fovea of central retina, controlling precisely the direction of the gaze.

Focusing on the eye itself, the eyeball is shaped as a semi-sphere, rather it is the result of fusing a small strongly curved sphere—anterior segment formed by cornea, iris and lens—and a larger posterior sphere composed of the sclera, choroid, retina and the vitreous. The ring joining both spheres is called the limbus. Looking at the eye from the front, one can see the white sclera surrounding the cornea, under the cornea is located the iris, the structure that determines the color of the eye, and in its central section appears the pupil, dark because the light passing into the eye is absorbed and not reflected.

The eye has a fairly constant vertical diameter of 24 mm (varying among normal individuals by 1-2 mm) and it is covered with three layers enclosing the aqueous humor, lens and vitreous body. The external coat consists of the cornea and the sclera. Middle layer is formed by the choroid, the ciliary body and the iris and contains the main blood supply. The innermost coat is the retina that lies on the choroid. Inside the cavities covered by these coats there are other elements: the crystalline lens, connected to the ciliary body by fine fibers; the aqueous humor, a transparent fluid between the cornea and the lens and iris; the vitreous body, a clear jelly that fills the cavity enclosed by the sclera, the ciliary body and the lens. Figure 1.2 provides better insight into the human eye structure.

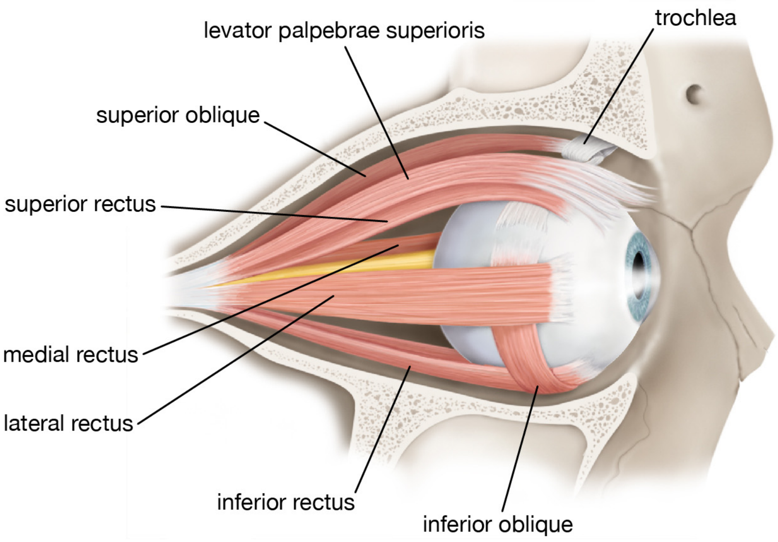

Figure 1.1. Illustration of the muscles of the right eye.

Source: Encyclopædia Britannica, Inc.

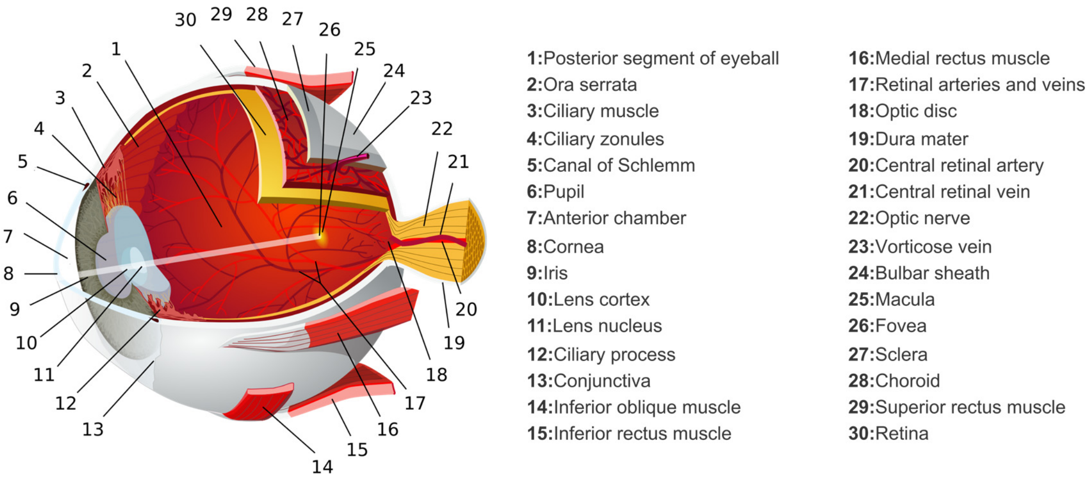

Figure 1.2. Schematic diagram of the human eye.

Source: modified from Wikimedia Commons (Licensed under the CC BY-SA 3.0).

1.3. Optical System of the Human Eye

The main function of the optical system in the eye is to refract light to produce or project an inverted and focused image of the visual field on the retina, where photoreceptors (cones and rods) are located. The complete system acts as convex lens, but refraction occurs at four separate surfaces: anterior and posterior surfaces of the cornea and of the crystalline lens. Each of these surfaces change the direction of propagation of light rays toward the visual axis, converging the incoming light and projecting it onto the retina.

The crystalline lens is attached by the zonular fibers to the ciliary muscle which can contract or loosen changing the shape and, consequently, the refractive power of the lens. This mechanism of accommodation controls the view of objects at varying distances, always projecting them on the retina. Accommodation is a reflex act (involuntary) and the stimulus for accommodation is the nearness of the object but, nevertheless, the way in which this nearness is converted into a stimulus seems not to be clear. According to [2], the cornea itself has an

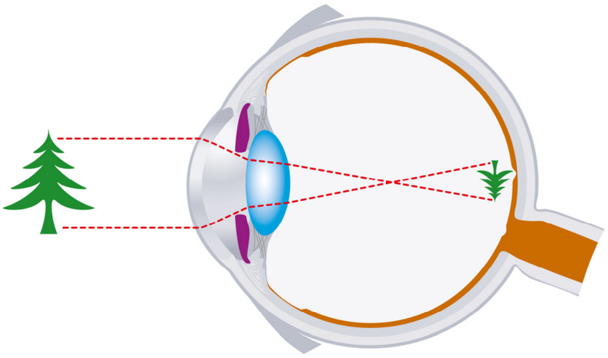

Figure 1.3. Diagram of the optical system of the human eye.

average refractive power of 42.4 diopters. Besides, in its non-accommodative state, the crystalline lens contributes about 15-20 diopters of the approximately 60 diopters of convergent refractive power of a normal human eye [3], for a normal focal length of 16.7 mm. When accommodation is produced to focus on nearby objects, the ciliary muscle contracts the lens—it becomes more spherical—and its refractive power increases.

The light entering the eye is controlled and restricted by the aperture in the iris, the pupil. It appears black because the light rays are absorbed by the tissues inside the eye and no energy is reflected. The state of pupil—the aperture—is determined by the degree of illumination: in low light conditions, the pupil aperture increases to capture the incoming energy (mydriasis). Instead, when under strong lighting conditions, the pupil is closed to prevent photoreceptors from saturation (miosis). This physiological response of dilation and constriction is known as pupillary response and occurs together with accommodation. The aperture of the pupil is controlled by the muscles of the iris: constriction of the pupil is produced by shortening the circular ring of fibers (the sphincter) and dilation is brought about by shortening of the fibers oriented radially. The pupil size in adults can vary from 2 mm in diameter in bright light to 8 mm in the dark, approximately.

1.4. Photoreceptors on the Retina: Cones and Rods

The retina is a filmy piece of tissue (about 0.5 mm thick) which covers the inside of the eyeball. This inner coat of the eye is considered part of the brain [4], since it includes light-sensitive sensory neurons and intricate neural circuits responsible for the first stages of image processing, permitting a good deal of image assembly to take place in the eye itself. Nevertheless, the final perception of sight is done in the brain.

Figure 1.4. Illustration of the retina: light enters from the left penetrating the retina before reaching photoreceptors on the right [4].

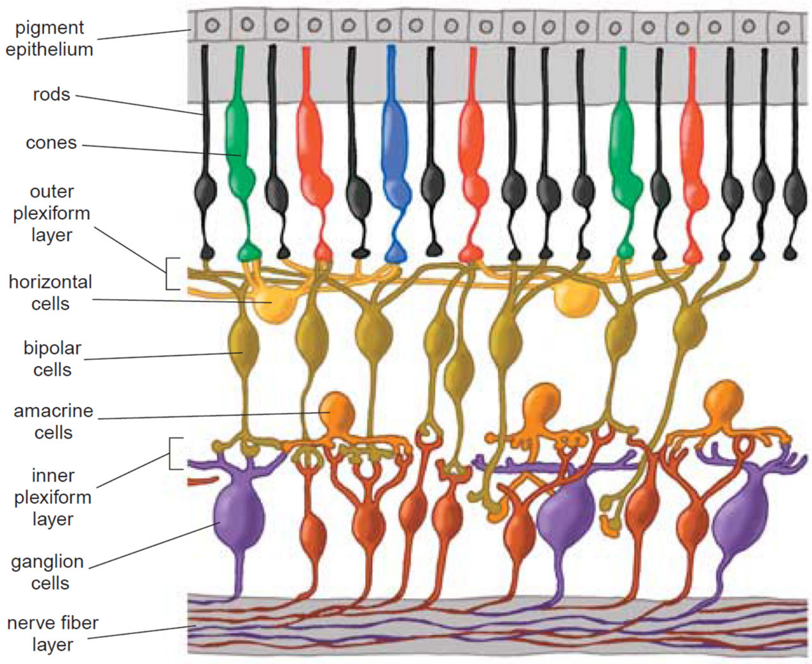

Figure 1.5. Rendering of the layers of the retina. Photoreceptors are at the top, close to the pigment epithelium [4].

Light enters the eye through the pupil, the photons travels across the vitreous fluid of the eyeball and penetrate the retina before reaching the photoreceptors. Contrary to expectations, the sensory cells are placed at the very back of the retina, meaning that light rays must pass through the entire retina before exciting pigment molecules. The pigment-bearing membranes of photoreceptors are in contact with the eye's pigment epithelial layer, a very dark tissue behind the retina full of melanin granules responsible for absorbing strayed photons, to prevent their back reflection into the photoreceptors and protect these cells from overexposure to light (see Figure 1.5). The signals captured by photoreceptors pass through a series of neural connections toward the surface of the retina, where the ganglion-cell nerve-fiber layer relays the processed information to the optic nerve, the responsible for sending an electrical signal into the brain for further processing and visual perception.

Looking at the sensory cells, all vertebrate eyes contain at least two types of photoreceptors: cones (for daylight, colored vision) and rods (for low-light vision), as can be observed in Figure 1.6. However, the eyes of different animal species evolved differently trying to adapt to the different environments where they live. Primates (including humans) and raptors have front-projecting eyes, which allow the perception of depth (binocular vision). Moreover, their eyes are specialized for daylight vision and can discriminate fine details and color thanks to a highly cone-rich spot devoid of rods called fovea, responsible for sharp central vision. The fovea lies in the center of the macula—an oval-shaped pigmented area near the center of the retina—and it is an area where the maximum density of cone photoreceptors is concentrated (Figure 1.7).

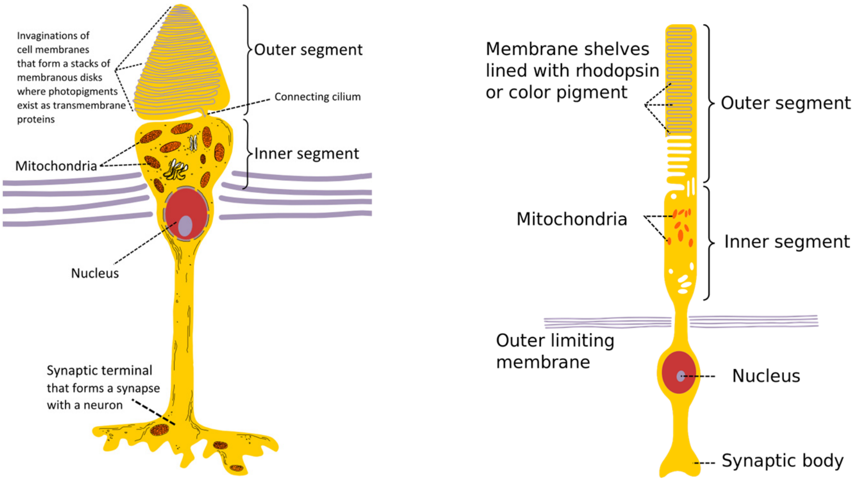

Figure 1.6. Anatomy of a cone cell (left) and a rod cell (right).

Source: Wikimedia Commons (Licensed under the CC BY-SA 3.0). Author: Ivo Kruusamägi.

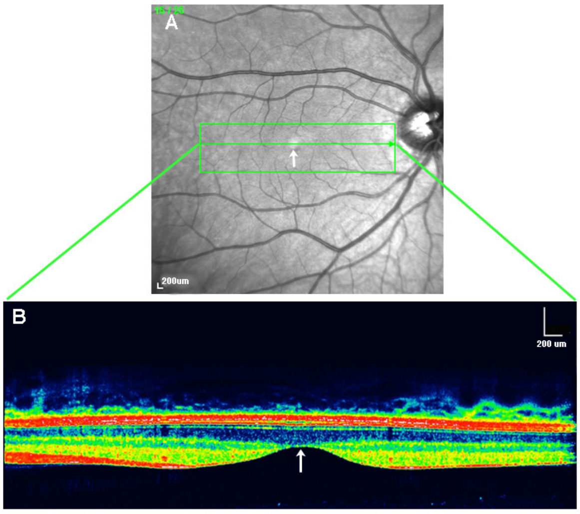

Figure 1.7. (A) Photography of a normal human macula, optic nerve and blood vessels around the fovea. (B) Optical coherence tomography image of the same macula, where the fovea is marked with an arrow [5].

As previously mentioned, two basic types of photoreceptors exist in the human retina: cones and rods. The cone vision is oriented to color vision in bright conditions (photopic vision), adapting photoreceptors to the surrounding brightness and the circuitry in the retina modulates the eye's response. In a similar way, rods and the neural circuits to which they are connected are adapted to lower intensities of light (scotopic vision). Nevertheless, cones and rods report rather different image properties: cones, detecting bright signals, can detect more abrupt and rapid light fluctuations; rods, dealing with dim light signals, usually respond to slow variations.

Related to the frequency response, rods are sensitive to blue-green light and present a peak sensitivity around 500 nm wavelength of light. Cones, in contrast, are sensible to three different wavelengths and provide the basis of color perception in the human visual system (HVS). This 3-cone mechanism is also called trichromatic vision (Red, Green and Blue: RGB). In this way, we can classify cones as follows:

Cone Type	Wavelength Sensitivity	Absorbance Peak	Light Color
L-Cones	*Long*	*564 nm*	**Red**
M-Cones	*Medium*	*534 nm*	**Green**
S-Cones	*Short*	*420 nm*	**Blue**

Table 1.1. Human eye cone types, wavelength sensitivities and absorbance peaks.

When looking at the distribution of rods and cones in the human retina, they are organized in a quasi-exact mosaic [5]. It is important to analyze the spatial distribution of different sensory cell types in the retina: in the fovea, cones are packed in a semi-hexagonal lattice structure. Outside the fovea, rods split this hexagonal structure forming a sort of rings surrounding cone cells (observe Figure 1.9).

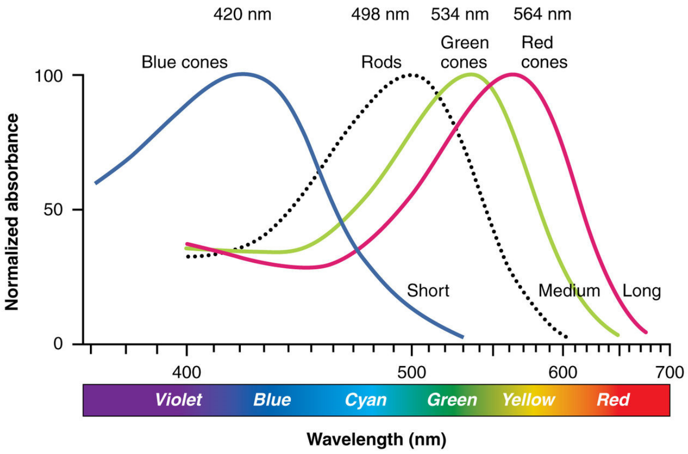

Figure 1.8. Normalized human eye photoreceptor absorbances for different wavelengths of light.

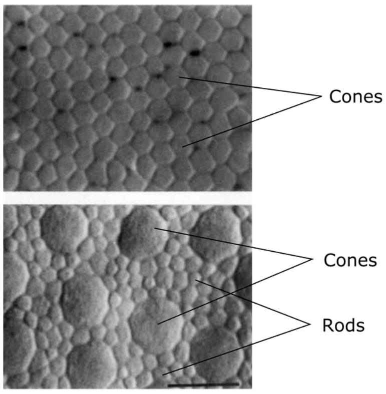

Figure 1.9. Cross sections of the human retina: cones in the fovea (top) and cones and rods in the near periphery (bottom) [6].

In terms of density (Figure 1.10), the average human retina contains 4.6 million cones and presents the maximum density in the fovea centralis in an area as large as 0.032 degrees [6], but the density decreases quickly with increasing eccentricity outside the fovea to an almost constant and insignificant value into the peripheral retina. Besides, the average number of rods in the retina is about 92 million. The highest rod densities are placed at a ring at the eccentricity of the optic disc, but it becomes nearly null in the foveal pit defining a rod-free zone with an average diameter of 0.350 mm (1.25 degrees). Rod density decreases slowly from the ring to the far periphery of the retina. The optic nerve is free of photoreceptors and, therefore, it creates a blind spot in the area through which it leaves the eye orbit via the optic canal.

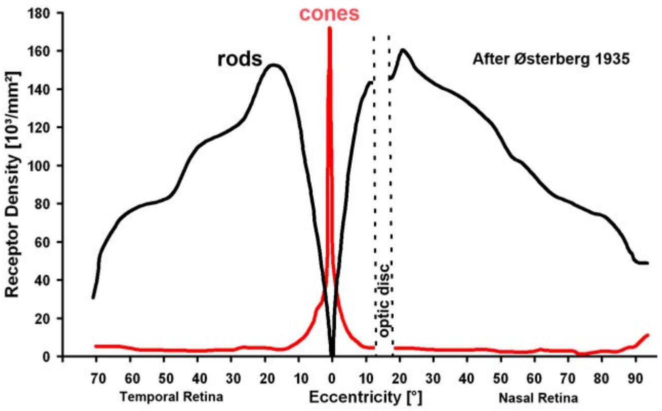

Figure 1.10. Density of rods and cones along the horizontal meridian on the retina [5].

1.5. Human Visual System vs. Conventional Imaging Systems

The HVS is considered a biological imaging system since it gives the ability to process and generate images. In this regard, it might be worth comparing it against conventional imaging systems, such as digital cameras. This analysis can be approached from different perspectives:

a) The optical system.
b) The image sensor.
c) Angular resolution.

1.5.1. Analogies of the Optical System

The optical system of the human eye and common digital cameras have multiple similarities and coincidences (Figure 1.11). In both systems light enters through an aperture set by the iris, which is called pupil in the eye. For preventing the light from entering the imaging system from any direction other than the aperture the eye uses the sclera, while in digital cameras this role

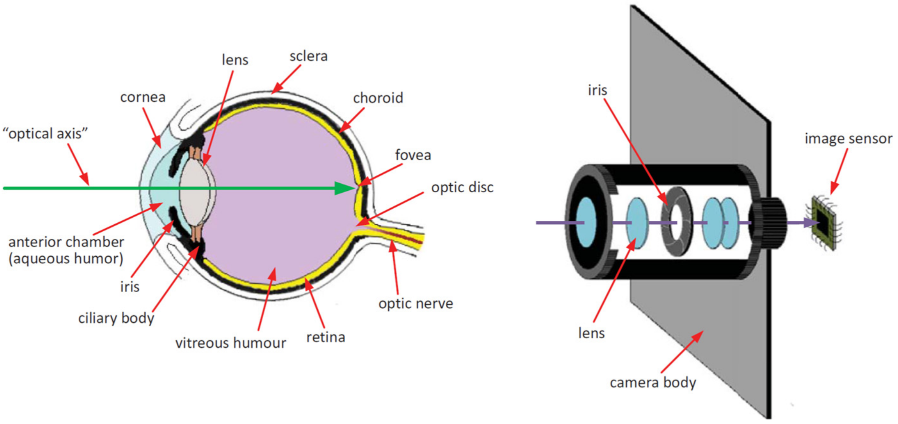

Figure 1.11. Diagram of the human eye (left) vs. optical system of a digital camera (right).

is played by the camera body. Refraction of light is performed by a lens system—being possible to change the focal distance—and the image is projected upside down on the retina (eye) or the image sensor (digital cameras). Finally, photons are converted into electrical signals by photoreceptors (cones and rods) in the eye and digital sensors in cameras, and subsequently sent to the brain by the optic nerve (or wires) to be processed.

In terms of physical dimensions, the aperture of an adult pupil can variate from 2 mm (contracted) to 8 mm (dilated) in diameter depending on lighting conditions. Considering the commonly quoted focal length of 16.7 mm, it is easy to calculate the f-number N of the human eye based on equation 1.1,

$$N = \frac{f}{D} \tag{1.1}$$

where f corresponds to the focal length and D is the diameter of the entrance pupil (effective aperture). Using this formula and the aperture values previously established, the human eye can be defined as an $f/8.3$ lens for bright light conditions and as an $f/2.1$ lens in dimly light environments [7]. Comparing against standard f-stop scale of modern lenses in digital cameras these values fall within the normal range.

1.5.2. Comparative Analysis of Sensors

Actual digital camera image sensor technology is mostly based on Charge-Coupled Devices (CCD) and Complementary Metal-Oxide Semiconductors (CMOS). The CCD was developed in 1969 at AT&T Bell Labs by George Smith and Willard Boyle (in 2009 they were awarded the Nobel Prize of Physics). CCD devices offer high image quality and flexibility—in return the size of the system tends to be greater—and it makes this technology suitable for high-quality imaging applications, normally oriented to professional, medical and scientific purposes. On the other hand, active-pixel sensors (APS), which include CMOS sensors, where established by Tsutomu

Nakamura in 1985 [8], and more broadly defined by Eric Fossum in 1993 [9]. When comparing with the performance of CCD imaging technologies, CMOS imagers offer superior characteristics related to integration, power dissipation and system size, but at the cost of image quality (mostly in low light), making it fit for high-volume, space-constrained applications with low quality requirements. CMOS technology is more focused in consumer cameras (smartphones, webcams, digital pocket cameras) with lower quality standards and professional digital cameras: digital single-lens reflex cameras (DSLR).

In relation to the image capturing process of digital cameras, an image of the visual field is projected through the lens onto the sensor (photoactive region), which is a square grid array of pixelated metal oxide semiconductors. Each pixel accumulates a signal charge proportional to the local light intensity acting as a spatial sampling function and capturing a 2D image of the scene projected onto the focal plane, where the sensor is positioned. When the exposure time is complete, the CCD sensor transfers sequentially the charge packet of each pixel to a common external structure (a printed circuit board) for further processing: convert charge to a voltage, buffer and send it off-chip. The main difference between these technologies is that a CMOS sensor performs the charge-to-voltage conversion locally in each pixel and most functions are integrated into the chip. This variation on readout techniques (see Figure 1.12) directly affects the sensor architecture, capabilities and limitations [10].

To capture color images, digital camera sensors make use of a Color Filter Array (CFA) known as Bayer filter, for arranging RGB color-sensitive filters on a square grid of photosensors. The Bayer array sensor strategy consists of alternating green (G), red (R) and blue (B) color filters, but using twice as many green elements (50 %) as red (25 %) or blue (25%), trying to mimic the physiology and the distribution of sensors in the human eye (Figure 1.13). The RGB values obtained from these photosites are then combined in an intelligent way to create full color pixels by means of a process called demosaicing. Even if the Bayer filter is nearly universal on digital

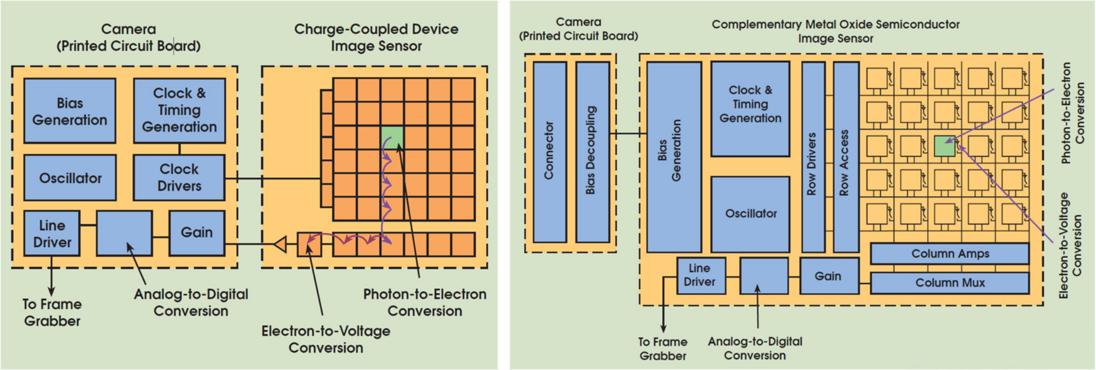

(a) (b)

Figure 1.12. Sensor architecture schematics: (a) CCD sensor and (b) CMOS sensor [10].

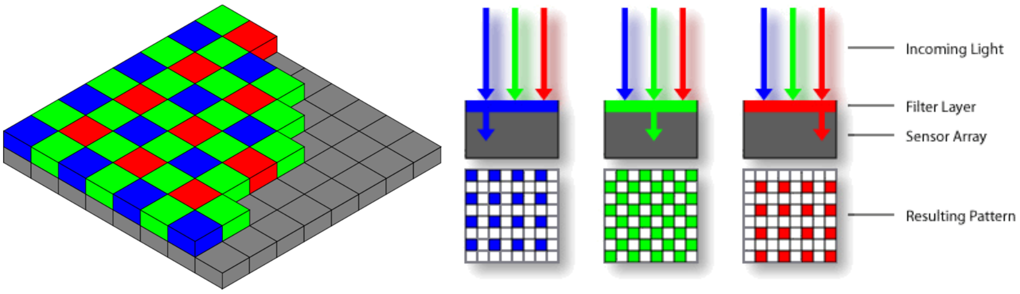

Figure 1.13. Schematic of Bayer filter overlain on a sensor (left). Side-view of color photosites and resulting RGB patterns (right).

camera applications, there are also multiple alternatives and variations (modifications of the Bayer filter mosaic).

At first glance, the sensing method of digital cameras appears to have close similarities with the image capturing mechanism of the human eye. However, it is worth analyzing some aspects more deeply, to draw a more detailed comparison.

- ***Photon Capturing and Dynamic Range***

The European Machine Vision Association (EMVA) proposed the EMVA Standard 1288 [11], which defined a unified method to measure and compute specification parameters and characterization data for conventional digital cameras or image sensors. The company Point Grey compared multiple color single lens camera models with CCD and CMOS sensors, adopting the EMVA 1288 standard for testing and published the latest results in the Q2 2016 Color Camera Sensor Review [12]. This document analyzes multiple camera parameters as the quantum efficiency (capacity to convert incoming light into an electrical signal), dynamic range, saturation capacity, temporal dark noise and the absolute sensitivity threshold.

According to the EMVA 1288 Standard, the number of photons received by a pixel or sensor is proportional to its area A, the exposure time t_{exp} and the irradiance E on the sensor surface area in W/m^2, as follows:

$$\mu_p[\text{photons}] = \frac{AEt_{\text{exp}}}{h\nu} = \frac{AEt_{\text{exp}}}{hc/\lambda}, \tag{1.2}$$

using the quantification of the energy of electromagnetic radiation in units of $h \cdot v$, where h=6.6260755·10^{-34} J·s is the Planck constant and $v=c/\lambda$ the frequency related to the wavelength λ and the speed of light c=2.99792458·10^8 m/s.

Supposing the same irradiance E and exposure time t_{exp} when comparing different sensors, the only factor affecting the number of photons captured by a pixel is the area A of the sensor itself. In the particular case of the human eye, the average size of photoreceptors or cones in the fovea—the area over the retina that deals with sharp central vision—is about 1.5 µm diameter [5], which is quite small in comparison with the pixel sizes of conventional cameras shown in the review (from 2.2 to 9.9 µm). Comparing the area of a cone (assuming a circular shape 1.77 μm^2) with the area of the smallest pixel size of a digital camera (4.84 μm^2) extracted from [12], the area of a human eye photoreceptor would be 2.74 times smaller, reducing by the same factor the photon flux captured by each sensor.

This could also limit the dynamic range of the HVS (the ratio of a pixel's saturation level to its signal threshold) if we define it as in equation 1.3, since saturation capacity is a magnitude related to the pixel size:

$$DR = \frac{u_{p.sat}}{u_{p.\min}} \tag{1.3}$$

where $u_{p.sat}$ is the saturation irradiation and $u_{p.\min}$ represents the minimum detectable irradiation or absolute sensitivity threshold. However, the human eye presents an extraordinary dynamic range and detects subtle contrast variations [13], being able to perceive information from very low-light conditions up to the brightness of daylight. Different sources [14], [15], define a detectable luminance range of cone cells for photopic vision (chromatic or color perception) of 10^8 or 160 dB when expressed on a logarithmic scale as it is shown in equation 1.4.

$$DR_{dB} = 20\log_{10}(DR) \tag{1.4}$$

This value overcomes largely the multiple dynamic ranges observed in the camera review, presenting values from 53 to 73 dB approximately, even if the sensors in the human eye are considerably smaller in area. In more specific scientific imaging applications, CMOS sensors with dynamic ranges up to 120 dB can be found, which are achieved by means of different High Dynamic Range (HDR) imaging techniques [16]–[18]. Nonetheless, these values are nowhere near to the ones obtained by the human eye.

- ***Sensor Resolution***

The resolution achieved by a CCD or CMOS image sensor is determined by the size of its detectors (pixels) and the total size or area of the image sensor itself. However, there are technological challenges and constraints in relation to reducing the pixel size below some threshold, such as limits established by diffraction—which is considered further below—and electronical constraints connected to sensitivity (defined by ISO), understood as the capacity to distinguish information from noise. Current high-performance digital imaging technologies work with minimum pixel sizes of 1-2 µm. Therefore, actual technology tends to increase the number of pixels and the image sensor size (full-frame DSLR sensor size is 36×24 mm), enlarging the total area where the image is captured and reaching image resolutions up to 30, 40 or even 50 megapixels.

The analysis of the sensor resolution in the human eye seems to be a little more complicated. While in digital cameras pixels are uniformly distributed in a square matrix-like layout—ensuring a constant resolution over the entire image sensor—, cones in the retina are not distributed in a regular manner. As explained in detail above, the human eye contains about 4.6 million cones (equivalent to 4.6 megapixels), which reach a density peak in the fovea. However, this density decreases quickly when approaching peripheral retina, where there are practically not cones, but rods. This irregular distribution of photoreceptors avoids a constant resolution over the image captured by the HVS: the maximum resolution is obtained in the foveal visual angle, but outside the center of the gaze, the visual ability and resolution decrease drastically (peripheral vision) being difficult to focus objects and only large-scale contrast and minimal color is detected (see Figure 1.14).

Some authors [19], establish a maximum density of 147,000 cones/mm^2 in the central part of the fovea. Others [6], estimate peak foveal cone density averages of 199,000 cones/mm^2, which is a highly variable value between individuals (100,000-324,000 cones/mm^2). These cone densities are responsible for color vision and highest visual acuity in the foveal visual angle. These numbers can be compared against single lens color cameras analyzed in the Q2 2016 Color Camera Sensor Review [12], calculating sensor densities for cameras with similar pixels characteristics in terms of size. Table 1.2 shows the results in pixels per square millimeter for different CCD and CMOS image sensors. From these data, it may be said that the maximum cone density values in the retina and pixel densities used in conventional CCD or CMOS sensors are fairly similar.

Figure 1.14. Representation of visual detail using a single glance of the eyes.

Source: Cambridge in Colour.

SENSOR	SENSOR SIZE	SENSOR TIPE	MAX RESOLUTION	PIXEL SIZE	PIXEL DENSITY (pixels/mm^2)
Aptina MT9P006	1/2.5”	CMOS	2592 × 1944	2.2 µm	≈ 207000
Sony IMX036	1/2.8”	CMOS	2080 × 1552	2.5 µm	≈ 160000
Sony IMX136	1/2.8”	CMOS	1920 × 1200	2.8 µm	≈ 128000
Sony ICX808	1/1.8”	CCD	2016 × 2016	3.1 µm	≈ 104000
Sharp RJ32S3AA0DT	2/3”	CCD	2448 × 2048	3.45 µm	≈ 84000

Table 1.2. Pixel densities of single lens color cameras.

Source: 2016 Q2 Color Camera Sensor Review (Point Grey).

1.5.3. Angular Resolution

The concept of resolution in relation to images can be interpreted from different perspectives: some theories define it as the number of pixels or dots contained in an image, using the term resolution just for a pixel count in digital imaging. Others, however, link the resolution to the level of detail in a picture, understanding it as the capability of the sensor to observe or capture clearly objects (information) as small as possible.

The angular resolution or resolving power is the ability of an imaging device to resolve (see separately) two different point sources at a small angular distance; i.e., the minimum distance between objects to be distinguished in an image. Westheimer [20] defined visual acuity as the limit of the ability to discriminate spatial partitioning in the eye’s object space. Other authors [21], proclaimed that there are multiple ways to understand the acuity parameter of the human eye but, in order to avoid confusion, we will define the acuity as the capability to discriminate two punctual sources placed close to each other, when observing from a certain distance.

This angular resolution or acuity is not just about the total number of pixels of an image, but also about the degree of detail that an imaging device—or the eye—is capable of distinguishing and capturing. Therefore, the size and the separation between adjacent pixels must also be considered. Moreover, since it establishes the minimum distance between objects to be resolved, it can also be determined by the minimum angle formed with respect to the observer (imaging device, eye).

This minimum angle can be determined from the perspective of geometrical optics—ray optics—considering light propagation in terms of rays. If two punctual sources must be resolved, each of them should be detected at least by a pixel sensor, between which a non-excited pixel should be placed. In other words, we could easily calculate the angular resolution of an image sensor translating the separation between two non-contiguous pixel sensors outside the imaging device at a certain distance.

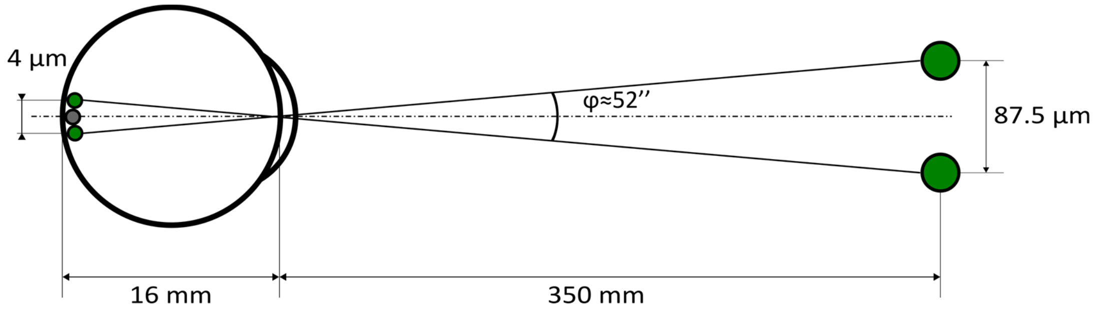

Figure 1.15. Scheme of the angular resolution of the human eye from the perspective of geometrical optics.

If we analyze the size and distribution of photoreceptors in the human eye, considering that the smallest size of a cone cell in the fovea is about 1.5 µm diameter—with approximated edge-to-edge separation of 0.5 µm [5]—it is possible to establish a separation between cone centers close to 2 µm. As previously explained, when two external point sources are to be solved, the retinal image must have at least an unexcited cone between the stimulated ones. Therefore, the minimum distance between two non-contiguous cones is of approximately 4 µm. Assuming a focal length of 16 mm for the human eye, we could easily calculate the angular resolution of the retinal image translating the separation of two non-contiguous cones outside the eye up to a normal reading distance (e.g., 350 mm). By performing simple mathematical calculations, the obtained resolution step is of 87.5 µm (see Figure 1.15).

If this concept of angular resolution is applied to conventional imaging devices, it is apparent that it is not possible to resolve smaller angular steps than the above defined, determined by the size and the separation of pixels in the image sensor. Analogously, under these circumstances, the human eye would not be able to resolve angular steps smaller than 87.5 µm. Nevertheless, we are capable of seeing beyond that limit, even though, a priori, we should not be able to resolve objects bellow this sampling frequency threshold (e.g., common human hair is nearly 50-60 µm thick and it is clearly visible and even resolved at larger distances).

The angle calculated from the resolution step observed in Figure 1.15 is of 52 seconds of arc, which is close to 1 minute of arc, the value considered by the scientific community as the acuity or resolving capacity of the human eye and known as the Minimum Angle of Resolution (MAR). However, there is ample evidence to indicate that the human eye can see below that resolving power: some authors [22] reported accuracies of 30-25 seconds of arc; others [23], [24], published results reaching accuracies of a few seconds of arc by measuring the ability to discern a misalignment among two line segments or gratings (Vernier acuity). Figure 1.16 shows some examples of how the eye can perceive details with a precision higher than the MAR.

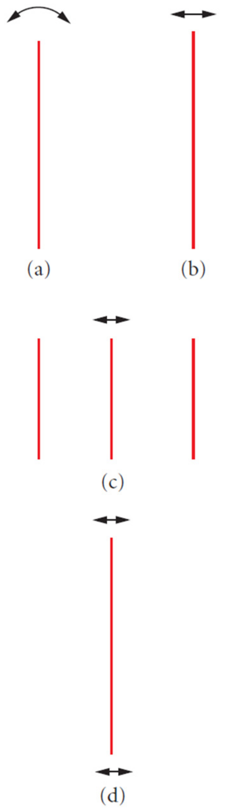

Figure 1.16. Configuration of lines in which location differences can be detected with a precision higher than the MAR. (a) orientation deviation from the vertical; (b) Vernier acuity; (c) bisection of a spatial interval; (d) deviation from straightness [20].

1.5.4. Summary of the Comparison

From this comparative study of the human eye and conventional digital cameras, it is possible to draw the following specific conclusions and findings:

1. The optical system of the HVS and digital cameras presents strong similarities when considering the general structure, physical dimensions, the light capturing mechanism or the properties of the lens.
2. The photoreceptors in the eye (cones) are specialized in red, green and blue (RGB) light wavelengths. Digital cameras employ the same strategy by using a CFA mosaic to split the light into primary colors.
3. The area of a cone is considerably small in comparison with pixel sensors of digital cameras and it could be limiting the photon flux captured by each sensor.
4. The dynamic range of the eye largely outperforms the values obtained from digital cameras with similar characteristics.
5. The peak cone density in the foveal retina and pixel densities values used in CCD or CMOS sensors can be considered comparable.

6. In terms of angular resolution and capabilities to resolve fine details, the human eye widely exceeds imaging devices with similar pixel sizes and separations.

In general, it can be said that multiple analogies exist between digital cameras and the HVS. However, there are some aspects related to dynamic range or angular resolution, for example, which cannot be explained by assuming the operation principles of conventional cameras.

Even though the human eye has a considerably low number of a reduced size sensors, the visual system shows an impressive performance with a very robust and simple architecture: a wide dynamic range, high sensitivity to see objects under low-light conditions or controlling the incoming light to prevent saturation. But in this regard, the most relevant feature is the high-resolution images it can obtain. This quality is known as visual hyperacuity and allows the human vision system to outperform artificial imaging systems with similar optical and sensor characteristics. This concept is explained in more detail in the following section.

1.6. Human Eye Visual Hyperacuity

The resolving power of the eye has for a long time been a subject of keen interest, since it has been known that the human eye could obtain spatial discriminations below the commonly established limit of visual acuity. Hartridge reported that the resolving power of the eye greatly exceeds 60 seconds of arc in 1922 [25]. However, it was Gerald Westheimer who introduced the term of hyperacuity in 1975 [20], aiming to define in some way the capacity of the eye to resolve the localization of points below the regular acuity threshold of 1 minute of arc related to the MAR. In other words, hyperacuity was defined as an additional class of visual threshold based on locating relative object position. This concept does not contravene the laws of optics, but suggests the existence of some sophisticated processing performed by the neural network and the brain. This extraordinary capacity of the human eye has been reported to achieve angular resolutions of 1 second of arc and even lower [26].

From the perspective of signal (or image) sensing, we can understand the hyperacuity as the capability of the human eye to resolve details beyond the understandable acuity defined by the number, size and distribution of photoreceptors. We could say that hyperacuity goes beyond the limits set by the retinal “pixels”, or stated another way, transcends sampling limits set by these discrete receiving elements. It is important to highlight that the visual hyperacuity does not imply the idea of image super-resolution. This concept involves techniques that construct high-resolution images from several observed low-resolution images through increasing high-frequency spectral components and reducing degradations produced by the low-resolution image capturing process [27], [28].

Although the existence of hyperacuity has been proven, there are significant differences when trying to determine how the human eye can achieve so high resolving power since different explanations have been proposed. Some theories attribute this skill to the capabilities of the brain, regarding cognitive resolution of points. Even if this mechanism exists in the HVS, it seems difficult to understand it from the point of view of information theory: new data points cannot be reconstructed from information that has not been captured.

There are also theories linking the hyperacuity and the micromovements of the eye, stating that these movements could be helping to fill empty spaces between cones [29], [30]. Nevertheless, others [31] explained that these micromovements improve the acuity in peripheral vision, but not in central vision. Following this line, microsaccade movements of the eyes could enhance spatial detail [32]–[34] and there are also those who assert that the information can be gathered due to small and quick vibrations of the human eye, thanks to temporal interpolation by combining slightly different images [35]. However, given the randomness and the high frequency of these micromovements, it results difficult to believe that the human eye could determine its spatial position at any time. Moreover, the eye requires of a certain interval of time to adapt the photoreceptors (cones and rods) to different visual conditions and there is an excitation-relaxation time that could exclude the idea of using micromovements to improving the visual acuity by combining images.

There are also interpretations based on the randomness of these eye dynamics, which argue that it can be modelled by a stochastic process [36]–[38] and authors [39] suggesting that the problem must be faced globally instead of locally since, from the view of the information theory, it has been established the relation between each photoreceptor and the points of the scene.

As it can be seen, there are multiple theories about the explanation of visual hyperacuity but it seems difficult to come to an agreement, even if its existence have been demonstrated.

1.7. Diffraction and Hyperacuity

Diffraction is the combination of various phenomena that take place when a wave encounters an obstacle or a slit. The effects of diffraction are present in every optical system, limiting the maximum achievable resolution in conventional imaging devices.

Sommerfeld was who first coined the term diffraction in 1954, defining it as "*any deviation of light rays from rectilinear paths which cannot be interpreted as reflection or refraction*" [40]. Later, in 1678, Huygens [41] found a method to predict the propagation of a wavefront through the free space based on the wave theory of light, stating that every point on the wavefront can be considered a new point source (Figure 1.17). In 1818, the French engineer and physicist Agustin-Jean Fresnel calculated with high accuracy diffraction patterns, taking some arbitrary

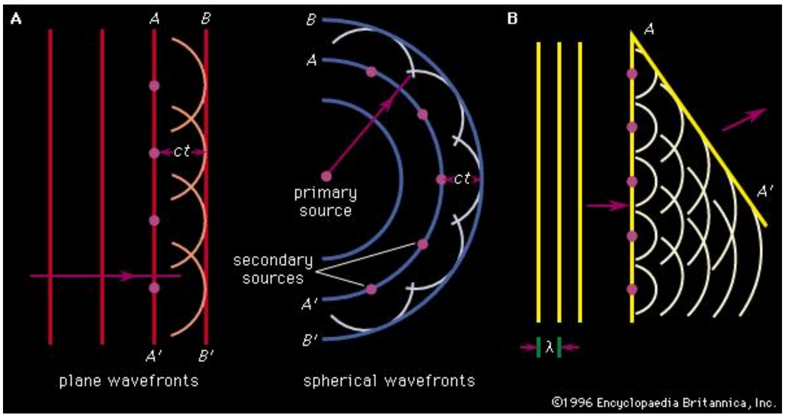

Figure 1.17. Application of Huygens' principle to plane and spherical wavefronts.

Source: Encyclopædia Britannica, Inc.

assumptions and founded on the Huygens principle and the concept of interference introduced by Thomas Young. Nonetheless, the most important theory came from James Maxwell in 1860, who identified light as an electromagnetic wave and developed the well-known equations, creating a consistent theory about electromagnetism, classical optics and electric circuits.

1.7.1. Mathematical Modeling of Diffraction

The different approaches explained bellow are approximations which consider light as a scalar phenomenon, neglecting that electromagnetic fields are vectors (as explained in Maxwell's equations). However, at microwave frequencies these approximations produce highly precise results, provided that some conditions are satisfied:

- The dielectric medium is linear, isotropic, homogeneous, nondispersive and nonmagnetic.
- The diffracting aperture is large enough compared with the wavelength.
- The diffracting fields must not be observed too close from the aperture.

- ***The Rayleigh-Sommerfeld Formulation of Diffraction*** [42]

Gustav Kirchhoff developed the first mathematical approximation of Huygens-Fresnel Theories in 1882, but a more accurate approach was subsequently made by Sommerfeld, called the Rayleigh-Sommerfeld diffraction theory.

A monochromatic scalar field can be written as:

$$u(P,t)=A(P)\cos[2\pi\upsilon-\phi(P)] \tag{1.5}$$

where $A(P)$ and $\o(P)$ are the amplitude and phase of the wave at a position P, and υ represents the optical frequency. It can also be expressed as:

$$u(P,t) = re\left\{U(P)e^{-j2\pi\upsilon t}\right\} \tag{1.6}$$

being $U(P)$ a complex function of position called phasor,

$$U(P) = A(P)e^{j\phi(P)}\,. \tag{1.7}$$

In accordance with Figure 1.18 and assuming a source producing a spherical wave at P_2 such as $U(P_2)=A$, the phasor at P_0 is given by:

$$U(P_0) = \frac{A}{j\lambda}\iint_{\Sigma}\frac{e^{jk(r_{21}+r_{01})}}{r_{21}r_{01}}\cos(\vec{n},\vec{r}_{21})ds \tag{1.8}$$

This result is the Rayleigh-Sommerfeld diffraction formula, which defines the phasor at a certain point at one side of an aperture, when a spherical wave source is placed in the other side.

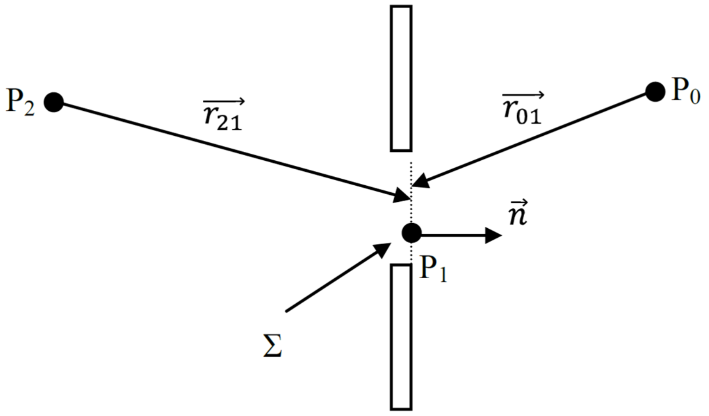

Figure 1.18. Point source illumination of a plane screen.

- ***The Fresnel Approximation*** [42]

In this instance, supposing that the diffraction aperture is located in the plane (ξ,η) which is illuminated in the positive *z* direction as shown in Figure 1.19, the wavefield at the point P_0 in the plane (x,y)—parallel to the plane (ξ,η)—is given by:

$$U(P_0) = \frac{1}{j\lambda}\iint_{\Sigma}U(P_1)\frac{e^{jkr_{01}}}{r_{01}}\cos(\theta)ds \tag{1.9}$$

which is the mathematical formulation of the Huygens-Fresnel principle. As long as $\cos(\theta) = z / r_{01}$, equation 1.9 can be expressed using a rectangular coordinate system:

$$U(x,y) = \frac{z}{j\lambda}\iint_{\Sigma}U(\xi,\eta)\frac{e^{jkr_{01}}}{r_{01}^{\ 2}}d\xi d\eta \tag{1.10}$$

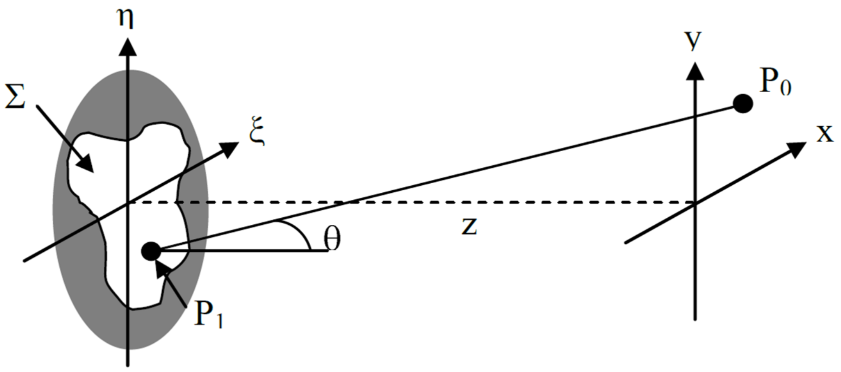

Figure 1.19. Scheme of variables for the Fresnel approximation.

where r_{01} is given by:

$$r_{01} = \sqrt{z^2 + (x-\xi)^2 + (y-\eta)^2} \tag{1.11}$$

Using the binomial theorem for algebraic expansion of powers, r_{01} can be approximated by:

$$r_{01} \approx z\left[1 + \frac{1}{2}\left(\frac{x-\xi}{z}\right)^2 + \frac{1}{2}\left(\frac{y-\eta}{z}\right)^2\right]. \tag{1.12}$$

Performing some mathematical operations, we can express equation 1.10 as follows:

$$U(x,y) = \frac{e^{jkz}}{j\lambda z} e^{j\frac{k}{2z}\left(x^2+y^2\right)} \int\int_{-\infty}^{\infty} \left\{ U(\xi,\eta) e^{j\frac{k}{2z}\left(\xi^2+\eta^2\right)} \right\} e^{-j\frac{2\pi}{\lambda z}(x\xi+y\eta)} d\xi d\eta \tag{1.13}$$

which is clearly recognizable to be the Fourier Transform of the product of the phasor $U(\xi,\eta)$ at the aperture and a quadratic phase exponential.

The Fresnel diffraction equation is an approximation, which is applicable in the near-field region of the aperture.

- ***The Fraunhofer Approximation*** [42]

The Fraunhofer diffraction equation is used to model the diffraction of waves when the diffraction pattern is observed in the far field of the aperture (e.g., the focal plane of an imaging system).

The approximation is based on the fact that when

$$z \gg \frac{k(\xi^2+\eta^2)_{\max}}{2}, \tag{1.14}$$

then,

$$e^{j\frac{k}{2z}(\xi^2+\eta^2)} \approx 1 \tag{1.15}$$

and therefore,

$$U(x,y)=\frac{e^{jkz}}{j\lambda z}e^{j\frac{k}{2z}\left(x^2+y^2\right)}\int\int_{-\infty}^{\infty} U(\xi,\eta)e^{-j\frac{2\pi}{\lambda z}(x\xi+y\eta)}d\xi d\eta \tag{1.16}$$

which is known as the Fraunhofer approximation and it is the Fourier Transform of the distribution in the aperture itself.

1.7.2. Diffraction in Optical Systems

The phenomenon of diffraction exists in the optical system of every imaging device and it is considered to be the main limiting factor to achieve the maximum resolution. Theoretically, a point source emits a spherical wave close to the source but, as these wavefronts propagate, they appear more planar and become a plane wave in the far field (see Figure 1.20). When this infinite plane wavefront goes through an aperture, it is spatially windowed producing diffraction. In this case, it will be assumed that the aperture of the optical system is uniformly illuminated and the produced diffraction corresponds to the Fraunhofer diffraction pattern—the focal plane is placed in the far field of the aperture—.

The main effect of diffraction is transforming point sources into blobs, which depend on the shape of the aperture, since it corresponds to the intensity profile of the aperture's Fraunhofer diffraction pattern. This spatial distribution of energy is defined by the Point Spread Function (PSF) and describes the response of an imaging system to a point source: the impulse response of an optical system.

The PSF or intensity pattern produced by a circular aperture is known as the Airy Disk, which was first studied by George Biddell Airy, who wrote the full theoretical treatment explaining this

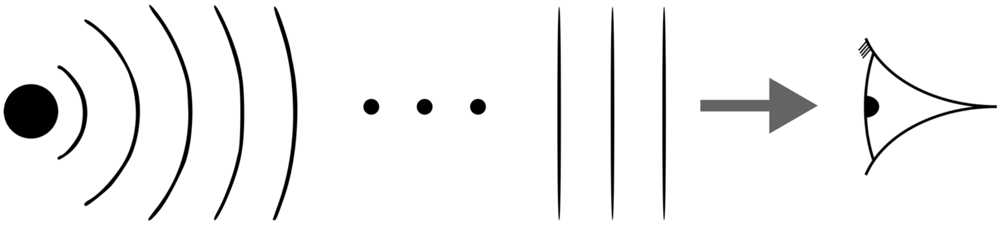

Figure 1.20. Transformation of spherical waves into plane waves in the far field.

phenomenon in 1835 [43]. If we assume a circular aperture of radius *a*, the intensity pattern produced at the focal plane located at a distance *F* from the aperture is given by:

$$I(\theta) = I_0 \left(\frac{2J_1(ka\sin\theta)}{ka\sin\theta} \right)^2 \tag{1.17}$$

$$I_0 = \frac{P_0 \pi a^2}{\lambda^2 F^2} \tag{1.18}$$

$$k = \frac{2\pi}{\lambda} \tag{1.19}$$

where I_0 corresponds to the maximum intensity at de center of the disk, J_1 is the Bessel function of the first kind and order one, θ defines the angle formed by the axis perpendicular to the aperture and the line between the observation point and the center of the aperture, P_0 is the incident power, λ is the wavelength and k the wave number (see Figures 1.21 and 1.22).

1.7.3. Diffraction-Limited Imaging Systems. The Rayleigh Criterion

As explained in previous sections, the pixels on the sensor of imaging devices based on CCD and CMOS technologies are uniformly distributed in a square matrix-like layout. The resolution achieved by a particular device depends to a great extent on the size of these light-sensitive

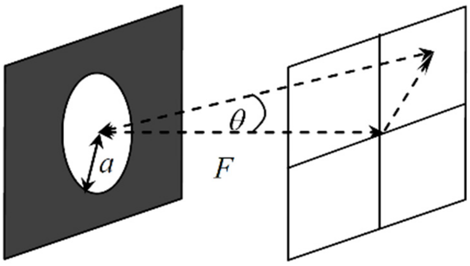

Figure 1.21. Scheme of variables in an Airy Disk.

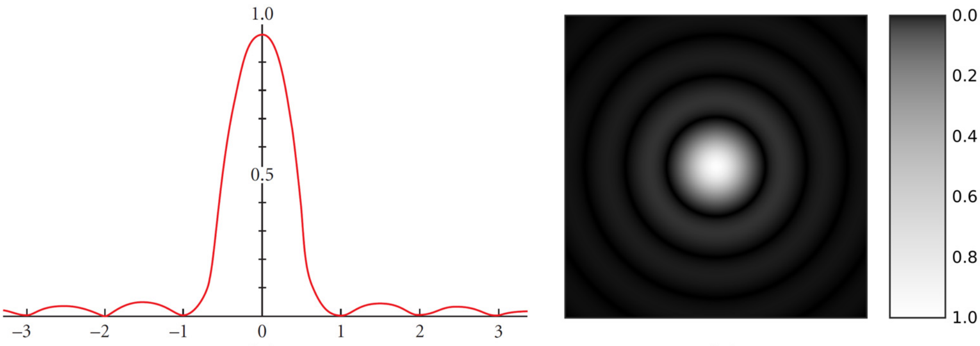

(a) (b)

Figure 1.22. (a) Intensity distribution of an Airy Disk. (b) Computer-generated Airy Disk.

cells, where the smaller the pixels are the higher resolution is obtained. However, the size of pixels cannot be reduced endlessly due to a practical limit established in connection to diffraction. As stated above, the diffraction introduced by the optical system transforms point sources into blobs when light is projected on the sensor (the focal plane). Since the intensity value captured by each pixel is the result of integrating the incoming power into its area during the exposure time, the captured image depends directly on the relationship between the diffraction blob and the pixel size. If a focused and clear (not blurred by diffraction) image must be captured, the blob must be small and sharp enough to fit most of its energy concentrated in the main lobe into a single pixel and, in this way, the distortion produced by diffraction will not affect neighboring pixels (Figure 1.23). Therefore, we can say that diffraction establishes the upper achievable resolution limit and these devices are said to be diffraction-limited imaging systems. In case that the diffraction blobs were bigger than the area of a pixel, a single point source would excite more than one sensory cell, producing a blurred image over the sensor.

The separation between pixel sensors in diffraction-limited system is established by means of Rayleigh criterion: two points (or lines) are just resolved if the peak center value of the PSF generated by one point lies exactly on the first zero of the PSF created by the second point (Figure 1.24).

In terms of angular resolution, the minimum angle that satisfies the Rayleigh criterion is given in radians by:

$$\theta = \frac{1.22\lambda}{a} \tag{1.20}$$

where λ is the wavelength of light and a the diameter of the circular aperture (both in the same units of length).

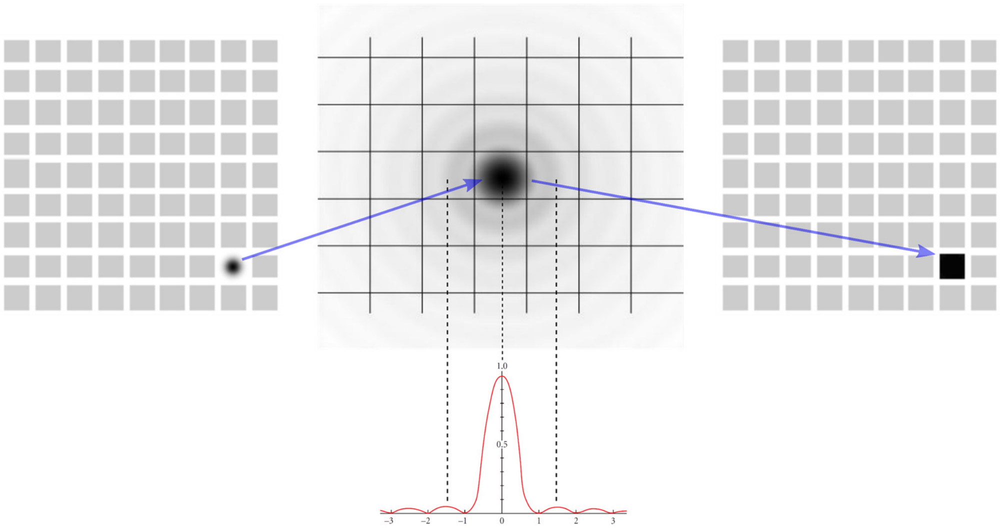

Figure 1.23. Diffraction-limited systems: diffraction pattern fits most of the energy into a single pixel.

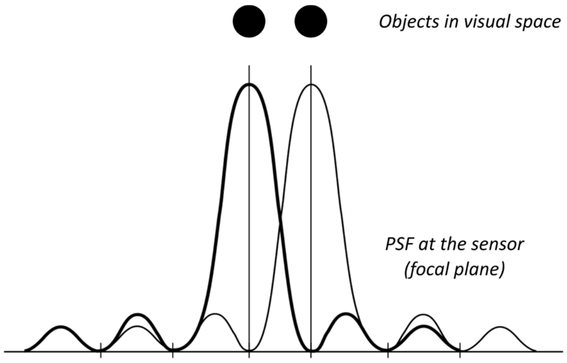

Figure 1.24. The Rayleigh criterion.

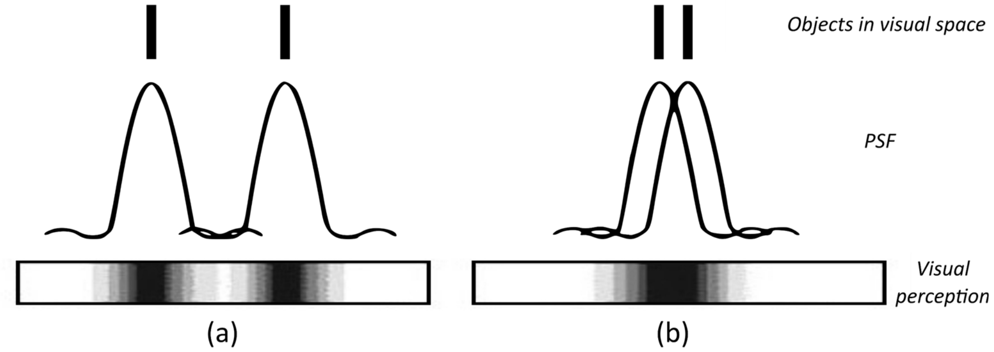

Figure 1.25. Rayleigh criterion representation between two lines: (a) resolved; (b) unresolved.

If two objects (point sources) are placed at this angular distance or larger, then they will be resolved. Nevertheless, if the distance between objects is smaller, the perception is that of one uniform distribution and they will be perceived as just one object (see Figure 1.25).

1.7.4. Diffraction in the Human Eye

In section 1.5.3 it has been calculated the angular resolution for the human eye—from the perspective of geometrical optics—analyzing the size and distribution of cones on the retina, and obtaining a resolution step of 87.5 µm. Nevertheless, in these calculations no consideration has been given to the effect of diffraction.

In connection with the resolving power, diffraction is in general considered a limiting factor because the Rayleigh criterion determines the minimum separation between sensors for a given diffraction pattern (PSF). Let us say that it could be possible to assume the human eye working according to the principles of diffraction-limited systems. Supposing that the aperture of the pupil variates from 2 mm (contracted) to 6 mm (dilated) in diameter, a focal distance of 17 mm and the wavelength of the visible spectrum of 550 nm, we can calculate the radial distance of the Airy disc produced in the human eye from de following equation:

$$x = 1.22\frac{\lambda F}{a} \tag{1.21}$$

where λ is the wavelength, F the focal distance and a the diameter of the circular aperture (the pupil).

The values derived from this formula show that the radial distance of the Airy Disk is of 1.92 µm when the aperture is 6 mm (low light) and 5.76 µm for an aperture of 2 mm (daylight). Therefore, a point source produces a spot from 3.84 to 11.52 µm wide over the retina. If we consider that the size of a cone cell in the fovea is about 1.5 µm diameter with a separation between cones of 0.5 µm (separation between cones centers of 2 µm) [44], it seems obvious that the blobs produced by diffraction in the human eye are considerably bigger than the area of a single cone: the energy is spread over multiple cells both for minimum and maximum aperture sizes (see Figure 1.26).

It seems to be clear that the human eye does not even come close to meeting the Rayleigh criteria: the energy coming from a single point source is spread over a relatively large area, exciting multiple neighboring pixels and projecting a blurred image over the retina because of diffraction. In conclusion, we can say that it is difficult to believe that the human eye works as a diffraction-limited system.

1.7.5. Other Causes Contributing to Blur the Retinal Image

As it has been mentioned above, the retinal image seems not to be clear and sharp, but strongly blurred because of the effect of diffraction of light produced by the entrance aperture (the pupil). On top of this, there are other factors that could also be contributing to blur even more the captured image.

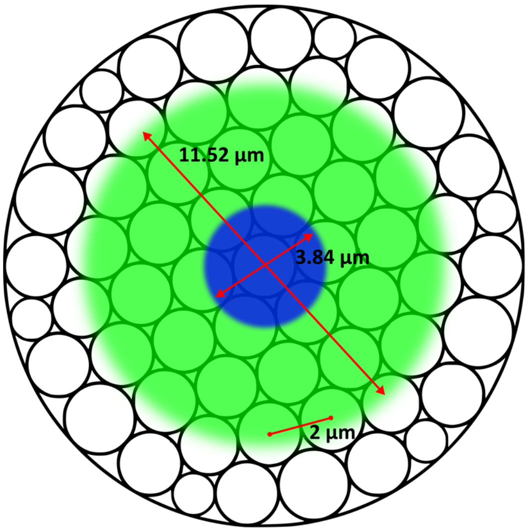

Figure 1.26. Scheme of the semi-hexagonal lattice structure of cones on the retina and the size of the Airy Disk for an aperture of 2 mm (green) and 6 mm (blue).

The photoreceptors (cones) on the retina, apart from the frequency response, they also produce some chemical responses which react to the arrival of photons [45]. These chemical reactions associated to the photon capturing mechanism create some degree of coupling between contiguous receptors, and it could be increasing the blurring effect.

On the other hand, during visual fixation different movements exist in the HVS: tremor, drifts and microsaccades [46]. Tremor seems to be the smallest movement in the eye with amplitudes about the diameter of a cone and approximated frequencies of 90 Hz. These movements are difficult to determine accurately, since they are thought to be aperiodic wave-like motions and independent in the two eyes [47]. Drifts, otherwise, have larger ranges of motion and lower frequencies and occur simultaneously with tremor [48]. At last, during voluntary fixation occur microsaccades, that are small and fast movements with amplitudes of hundreds of photoreceptor widths [49] and durations close to 25 ms [50]. Some theories claim that these random involuntary eye movements (tremor, drift and microsaccades) could be helping to achieve visual hyperacuity but, from our point of view, they could just contribute to generate blurrier images.

The last factor would be related to the temporal integration behavior of the HVS, which seems to be an important aspect for stereoscopic vision [51]. This integration time of the eye can be also understood from the perspective of photoreceptors capturing signals in a capacitor-like behavior. Since it has been reported that the integration time of the detection process can be larger than the period of microsaccade movements [32], it could also be defocusing the image.

Summarizing, we could say that even diffraction is the main contributor to blur the image projected over the retina, there are other additional factors that could be adding an extra blurring effect before the image is captured by the HVS.

1.7.6. Diffraction Enabling Hyperacuity

As formerly explained, there exist multiple theories that attempt to explain visual hyperacuity, some of them based on microsaccade movements or the integration behavior of the HVS and others founded on interpolation techniques combining different images. Nevertheless, from our perspective, both microsaccades and the integration time along with the diffraction effect produced by the entrance aperture (the pupil) could be contributing to produce a strong blurring effect on the image projected onto the sensor (the retina).

Even though diffraction is commonly seen as a problem and a limiting factor with regard to the maximum resolution achieved by imaging systems, it could have a key role on explaining the visual hyperacuity.

This concept may seem contradictory but, nevertheless, there are publications explaining the chance of going beyond the supposed limit set by diffraction when talking about resolution improvement [52]–[54]. Following this direction, other approaches raised the idea that the blurring produced in the human eye on account of diffraction could be enabling hyperacuity: [55] affirms that spatial smoothing does not hurt the possibility of extracting information and it could be effectively used under certain conditions, while [56] demonstrates how point-diffracted data can apparently be super-resolved by making use of certain methods. Additionally, [21] considers that the introduction of a pre-blurring stage prior to spatial sampling of an image can improve the ability to localize some image features and increases the capacity to detect movements, which is known as motion hyperacuity.

As previously said, the introduction of a controlled distortion—understanding it as the diffraction introduced by the optical system—can be the key issue to achieve visual hyperacuity or, in other words, exceed the angular resolution or acuity set by the number, size and separation of photoreceptors. From now on, possible distortions produced by other phenomena as microsaccade movements or chemical coupling reactions will be omitted, since its effect can be assumed as an increase of distortion that can be reproduced with the use of stronger diffraction patterns or PSF.

As a preliminary remark, it can be said that diffraction spreads information over a wider area and generates a spatial diversity that could be of great advantage. The energy coming from a single point source is spread over a bigger area, which means that this incoming energy will be captured by multiple neighboring sensory cells. This concept breaks the established relation that links each photoreceptor with a unique point in the observed scene and generates a more robust system, improving the system sensitivity and increasing the Signal-to-Noise Ratio (SNR) because multiple sensors receive information from the same point source. Moreover, the spreading of light could also contribute to capture or sense fine details that would be spatially located between detectors, that could not be detected in absence of diffraction (Figure 1.27 depicts this idea in a more visual form). Another possible potential advantage of the introduction of a known

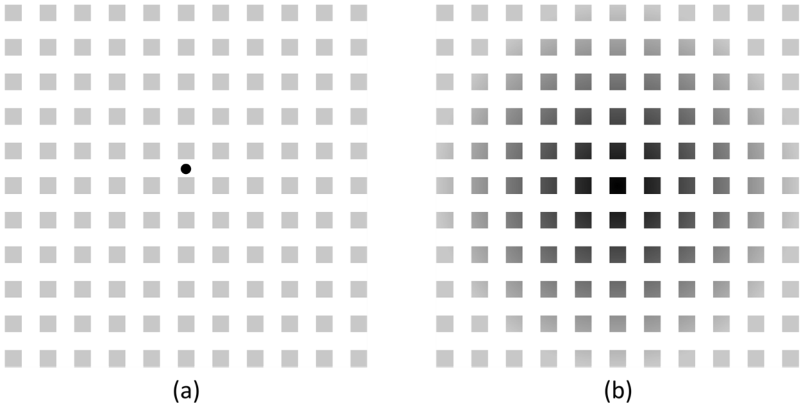

Figure 1.27. A point source that cannot be detected initially (a) is detected thanks to the spreading of light produced by diffraction (b).

blur is that it can be understood as an anti-aliasing filter for the effective sampling performed by the discrete distribution of photoreceptors. Diffraction produces a low-pass filtering (LPF) and the abrupt transitions of the observed image (high frequencies) are converted into smooth and slowly-varying functions (lower frequencies), relaxing the signal sampling requirements. This concept could be related to the reduced number of sensors used in the HVS for the sharp central vision where hyperacuity is produced. Moreover, the most relevant information of signals and images is kept in the lower frequencies and no critical data would be lost.

Therefore, starting from the hypothesis that a strongly blurred image is projected over the retinal photoreceptors, the neural network in the human brain should just solve an inverse problem or deconvolution, which seems not to be so complicated as simple mathematical operations are involved. At this point, the capability of the human eye to solve in an effective way the inverse problem cannot be questioned, understanding it as the ability to recover a clear and sharp image from a distorted, blurred one.

As a final comment, we can say that the HVS can be considered a diffraction-enhanced system, on the grounds that it is taking advantage of diffraction to achieve visual hyperacuity far from conventional imaging devices, widely known to be diffraction-limited.

1.8. Conclusions

This chapter analyzes the human visual system and more precisely the human eye, starting from anatomical and physiological aspects and, later on, comparing it against conventional imaging systems. As a result of this analysis, it can be assumed that both systems present some analogies and similarities. First, both optical systems seem to be comparable in terms of structure and dimensions (aperture, focal length, etc.). On another note, cone photoreceptors in the eye are specialized in red, green and blue (RGB) light wavelengths, while digital cameras make use of Bayer filters and other CFA for splitting the light in RGB channels showing an equivalent scheme. Additionally, the cone density in the fovea and pixel densities values used in CCD or CMOS sensors are reasonably comparable.

In contrast, there are some significant dissimilarities too: the average area of a cone is considerably smaller than the area of pixel sensors used in digital cameras, which could be limiting the photon flux captured by each sensory cell. Nevertheless, the human eye presents greater sensitivity in low-light conditions and good mechanisms to avoid saturation, largely outperforming the dynamic range of digital cameras. But the most remarkable feature is the capability of the human eye to resolve details in terms of angular resolution widely exceeding imaging devices with equivalent pixel sizes and separations. This amazing capability of the human eye to break the limits of resolution defined by the number, size and distribution of the photoreceptors is known as visual hyperacuity. Even if multiple theories have been developed trying to find an explanation of hyperacuity, it seems to be difficult to reach an agreement.

The phenomenon of diffraction exists in the eye like in all optical systems and the energy coming from a single point source is spread over a wide area, projecting a blurred image over the sensors and contravening the Rayleigh criteria. Therefore, it is difficult to believe that the eye works as a diffraction-limited system. From our point of view, this blurring effect produced by diffraction could be the key issue to achieve visual hyperacuity: the spreading of light over a wider area generates spatial diversity, creating a more robust system, improving the SNR and making possible to detect fine details. At the same time, it works as an anti-aliasing filter and relaxes the sampling requirements: it allows the use of a reduced number of sensors.

Taking this premise into account, it is reasonable to think that the human visual system may be performing some inverse filtering to remove the blur introduced by diffraction, a process that could perfectly be carried out by the neural network of the human brain.

Chapter 2

Visual Hyperacuity Simulation Method

2.1. Introduction

As stated in the previous chapter, the main hypothesis of this research work is based on the following statement: the diffraction produced by the optical system of the human eye plays a decisive role in achieving visual hyperacuity, which can be defined as the ability of the human eye to break the limits of resolution established by the number, size and separation of the photoreceptors.

On this assumption, it has been developed a method that aims to simulate the visual hyperacuity: the main objective is to improve the final image resolution when the number of available sensors is limited by means of the introduction of a controlled diffraction at the entrance of the system.

Figure 2.1 provides a graphic description of the proposed method: observe how a small detail may not be captured when the number of sensors is reduced (a). The introduction of a controlled diffraction (blur) spreads the information over a wider area and it makes possible to capture the information, despite the limited number of detectors (b). Next, we can perform an interpolation process creating new data points between the existing ones (c). Eventually, an inverse filter is applied to remove the blur introduced by diffraction, obtaining a sharp image with an enhanced resolution when comparing with the number of sensors used for image capturing.

This chapter provides a detailed description of the visual hyperacuity simulation method that, although it may look simple and straightforward at first sight, each stage requires further attention and analysis. The most critical step corresponds to the last one, due to the fact that the inverse problem is usually ill-posed and generates problems associated to stability and noise-amplification. Therefore, this stage requires further in-depth study and multiple methods or approaches are described. Mention that the use of 1D signals or 2D images has been used indistinctly, since it is not of great significance.

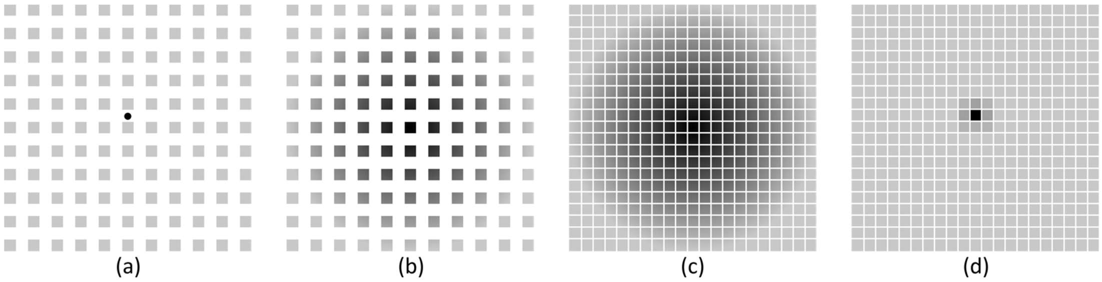
(a) (b) (c) (d)

Figure 2.1. Graphic representation of the visual hyperacuity simulation method.

2.2. Diffraction

The introduction of a controlled diffraction in a first stage produces the spreading of light coming from a point source in a wider area. The consequence of this expansion of energy is transforming sharp points into larger size blobs, generating a blurring effect over the whole image. Figure 2.2 shows the effect of a PSF approximating the diffraction produced by a circular aperture.

The following sections discuss multiple aspects linked to the introduction of a specific distortion in signals or images.

(a) (b)

Figure 2.2. (a) Original test image. (b) Image blurred because of diffraction.

Original image: Michael Kenna.

2.2.1. Mathematical Model for Image Blurring

Vogel [57] suggests a mathematical method which describes the introduction of a blur in an image, starting from the general model proposed by [58], a valid equation for modeling the diffraction of light when it is propagated from the source through a medium:

$$g(x,y)=\iint_{\mathbb{R}^2} k(x,x',y,y')f(x',y')dx'dy' \tag{2.1}$$

where f is the light source or object (in optics), the kernel function k is the PSF and g can be defined as the blurred continuous image, which represents an energy density or, analogously, the number of photons per unit area.

The image is usually captured with sensors that consist of a square matrix of pixels Ω_{ij} $(0 \le i \le n_x - 1, 0 \le j \le n_y - 1)$ used for photon counting. The energy captured by an individual array element (pixel) can be defined by

$$g_{ij}=\iint_{\Omega_{ij}} g(x,y)dxdy\,. \tag{2.2}$$

If it is assumed that each pixel Ω_{ij} has an area of $\Delta x \times \Delta y$ and (x_i, y_i) is the midpoint we obtain a discrete model as follows:

$$g_{ij} = \sum_{\mu=0}^{n_x-1} \sum_{\upsilon=0}^{n_y-1} k(x_i, x_\mu, y_j, y_\upsilon) f(x_\mu, y_\upsilon) \Delta x \times \Delta y \,. \tag{2.3}$$

When the blurring process is considered invariant under spatial translation, the PSF can be represented by means of a function of two variables, instead of four variables:

$$k(x, x', y, y') = k(x - x', y - y')\,, \tag{2.4}$$

and equation 2.1 is reduced to:

$$g(x, y) = \int_0^1 \int_0^1 k(x - x', y - y') f(x', y') dx' dy'\,, \tag{2.5}$$

considerably simplifying mathematical computations.

By analyzing equation 2.5, it can be observed a convolution form, given the source $f = f(x, y)$ and the PSF $k = k(x, y)$, and therefore, the blurred continuous image *g* can be computed using the convolution theorem:

$$g = F^{-1}\left\{F\{k\} F\{f\}\right\}, \tag{2.6}$$

where the continuous Fourier Transform of a function *f* defined on $\mathbb{R}^d$ (*d*=2 for 2D imaging) is defined as:

$$F\{f\}(\omega) = \int_{\mathbb{R}^d} f(x) e^{-i2\pi x^T \omega} dx\,, \quad \omega \in \mathbb{R}^d\,. \tag{2.7}$$

The inverse continuous function of the Fourier Transform is given by

$$F^{-1}\{g\}(x) = \int_{\mathbb{R}^d} g(\omega) e^{i2\pi x^T \omega} d\omega\,, \quad x \in \mathbb{R}^d\,. \tag{2.8}$$

From equation 2.6, it can be derived the Fourier inversion formula:

$$f = F^{-1}\left\{\frac{F\{g\}}{F\{k\}}\right\}. \tag{2.9}$$

However, if $F\{k\}$ takes values of zero, this formula is not valid (division by zero). Moreover, if it takes values close to zero, the reconstructed *f* is unstable in relation to perturbations in the data *g*. This is the case when the problem is ill-posed or, in other words, when any of the conditions for well-posedness explained below is violated:

An operator equation $K(f) = g$, $K: H_1 \rightarrow H_2$, it is well posed if:

i. For each $g \in H_2$ there exists a solution $f \in H_1$.

ii. The solution *f* is unique.

iii. The solution is stable with respect to perturbations in *g*, which means that if $Kf_* = g_*$ and $Kf = g$, then $f \to f_*$ if $g \to g_*$.

2.2.2. The Point Spread Function

As explained in Chapter 1, the intensity pattern (PSF) produced by a circular aperture *a* at a focal distance *F* is an Airy Disk described by:

$$I(\theta) = I_0 \left(\frac{2J_1(ka\sin\theta)}{ka\sin\theta} \right)^2 = I_0 \left(\frac{2J_1(x)}{x} \right)^2 \tag{2.10}$$

$$x = ka\sin\phi \tag{2.11}$$

In unidimensional approaches, the diffraction pattern created by a slit aperture can be approximated by a square *sinc* function, such as the following one:

$$\operatorname{sinc}^2(x) = \left(\frac{\sin(x)}{x} \right)^2 . \tag{2.12}$$

This function shows a very similar distribution to the Airy pattern in the time-space axis and a comparable behavior for signal processing when analyzing the case in 1D, considering that a slit aperture is equivalent to a circular aperture. However, things are different in 2D, where the equivalent aperture of a slit can be understood as a square shape aperture. Therefore, the 1D

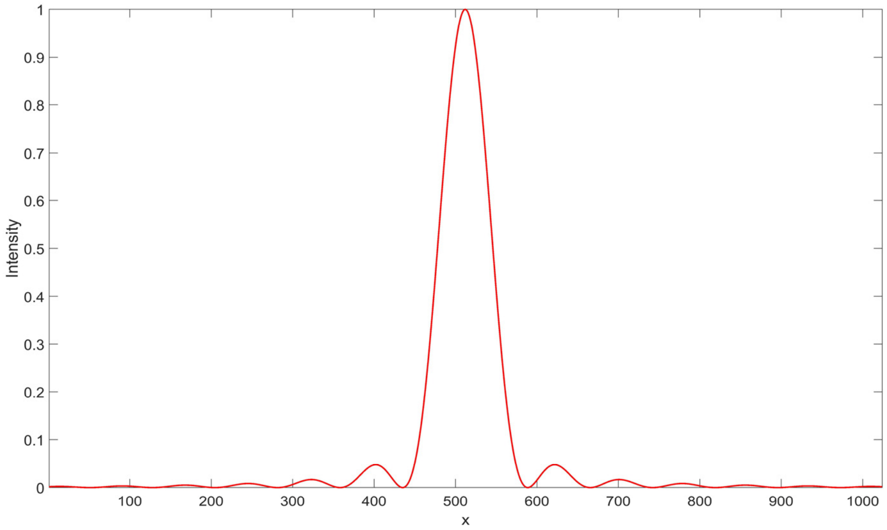

Figure 2.3. Square sinc type intensity profile of a slit aperture.

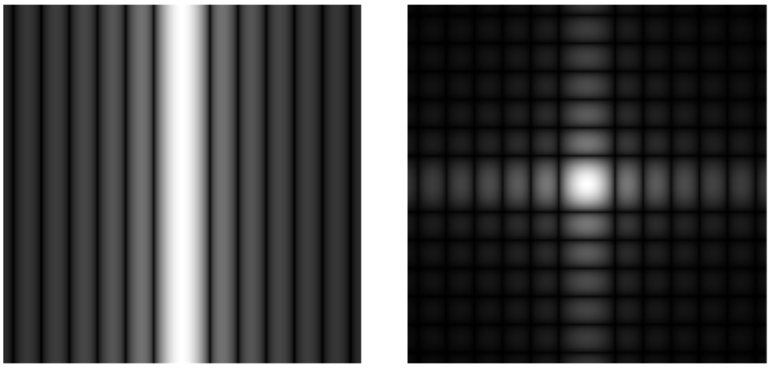

(a) (b)

Figure 2.4. Intensity pattern of a slit (a) and a square aperture (b).

function *sinc*^{2}*(x)* can now be modeled in a 2D spatial domain *(x,y)* by *sinc*^{2}*(x)·sinc*^{2}*(y)*. Figure 2.4 shows both the effect produced by a slit and a rectangular aperture on an image.

However, if we want to consider a circular aperture, *x* and *y* can no longer be treated independently. The Cartesian coordinates must be converted to polar coordinates by means of:

$$r=\sqrt{x^2+y^2} \tag{2.13}$$

where *r* determines the radial distance from the central point of the image *(x,y)=(0,0)*. In this way, the intensity pattern produced by a circular aperture (Figure 2.5) can be approximated by the function *sinc*^{2}(*r*) as depicted in Figure 2.6.

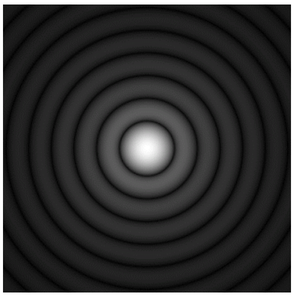

Figure 2.5. Intensity pattern of a circular aperture.

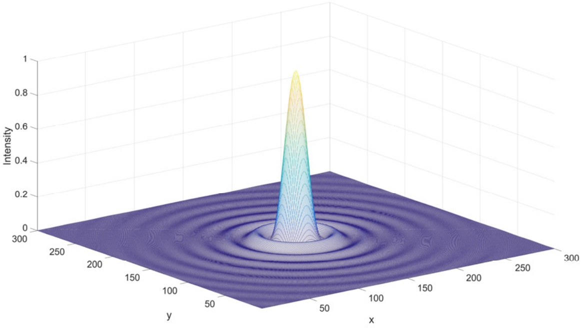

Figure 2.6. Square sinc type approximation of a circular aperture.

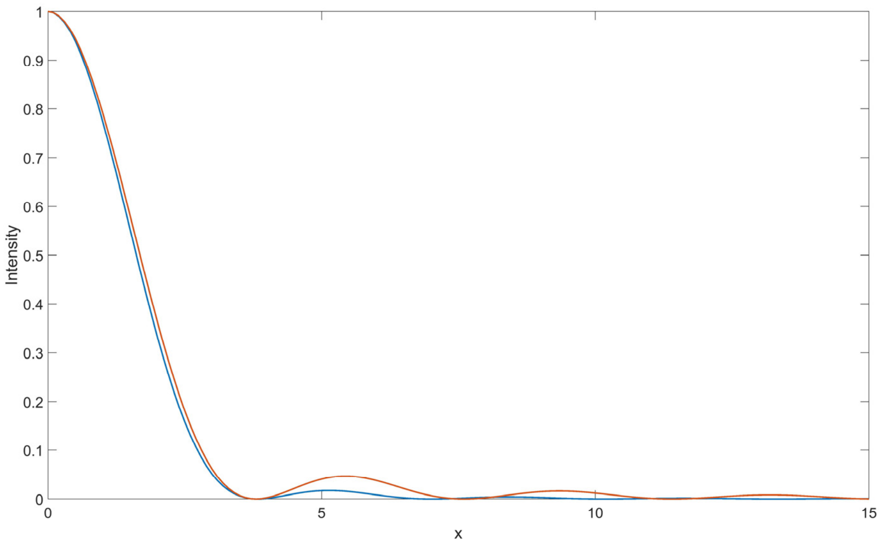

Figure 2.7. Radial cross-section through the Airy Disk (blue) and the approximation *sinc*^{2} function.

Supposing an equal width for the main lobe of both functions (Airy pattern and square *sinc*), the most significant difference between these functions can be appreciated in the side lobes: the Airy pattern presents lower amplitudes than the *sinc*^{2} function and the position of zeroes does not match (see Figure 2.7). Nevertheless, we can consider that side lobes stay in general below the detection threshold when talking about sensitivity and this approximation can be considered acceptable.

It must be said that the election of the square *sinc* function used to model the diffraction introduced by the aperture has been arbitrary. It is worth mentioning that the first approaches of the method were made in 1D and, in this case, a circular aperture can be modeled as a slit. Moreover, the *sinc*^{2} function implies less computational costs and greater simplicity to modify some parameters related to the PSF, such as the main lobe width or amplitudes.

In any case, the choice of one or other PSF is not of great significance since it only depends on the shape of the aperture, which is the Fourier Transform of the distribution in the aperture itself (Fraunhofer approximation). Therefore, it is not a crucial issue in the proposed method.

2.2.3. Image Blurring in the Spatial Domain: Convolution

As stated in the former section 2.2.1, the image blurring can be understood as a discrete spatial convolution of the original image *f*[*x,y*] and the PSF or kernel *h*[*x,y*] which acts as a LPF, resulting in a blurred image *g*[*x,y*].

$$g[x,y] = f[x,y] * h[x,y] = \sum_{i=-\infty}^{\infty} \sum_{j=-\infty}^{\infty} f[i,j] \cdot g[x-i, y-j] \tag{2.14}$$

Even if the equation of the discrete convolution has an infinite range, if we consider an original image *f* of *M*×*N* pixels and a PSF *h* of *P*×*Q* points, the size of the blurred image *g* will be *M*+*P*-1×*N*+*Q*-1 pixels.

There are some aspects that should be taken into account when blurring images in the spatial domain. We can understand the discrete convolution as the PSF *h* (a mask of *P*×*Q* pixels), sweeping the original image *f* by columns and rows and assigning a new value to each pixel, as explained in Figure 2.8. The blurring effect produced by the discrete convolution in a delta-like single pixel can be observed in Figure 2.9.

The blur or distortion introduced in an image can be classified as spatially invariant or variant. In the case of invariant distortion, the PSF is independent regarding the position in the image, which means that an object will be visualized in a similar way no matter its position. In other

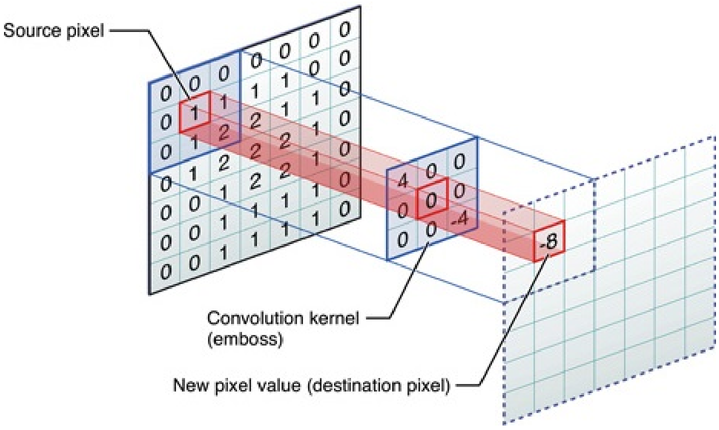

Figure 2.8. Kernel convolution.

Source: modified from Apple Developer.


(a)
(b)

Figure 2.9. (a) Delta-like pixel and (b) the effect produced by the discrete convolution with the PSF.

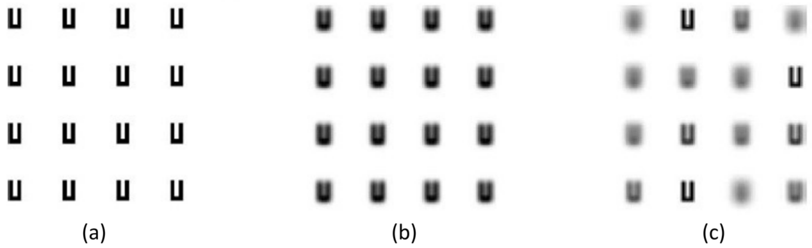
(a) (b) (c)

Figure 2.10. (a) Original image. (b) Spatially invariant distortion. (c) Spatially variant distortion.

words, the same kernel can be used to blur the whole image, producing a homogeneous blurring effect. However, when considering a space-variant distortion, different kernels must be used to calculate the distortion introduced in different locations, obtaining an irregular distortion depending on the position of objects on the image (observe Figure 2.10). The blur produced by diffraction in our method will be considered as a spatially invariant distortion.

Another issue to consider is connected to the boundary conditions of images, which are used to approximate the image scene outside the field of view due to the problems that pixels near the edges of a blurred image can generate, such as ringing [59]. This boundary conditions are usually not included in the PSF but in the original image and there are multiple methods for handling image edges:

- *Periodic:* the image is repeated itself in all directions.
- *Zero:* the pixels outside the borders of the image are zero (zero-padding).
- *Replicating:* the elements outside the image boundaries repeat the border elements.
- *Reflective:* the pixels outside the boundaries are a mirror of the pixels inside the boundaries.

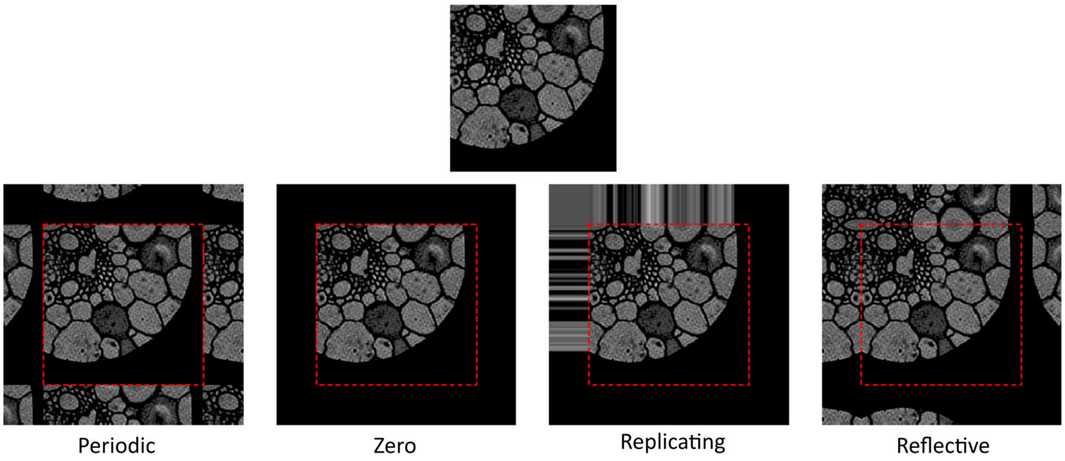

Figure 2.11. Image padding to incorporate boundary conditions [59].

In our case, in order to avoid problems in the pixels close to the edges, zero boundary conditions are used, performed by means of a zero-padding and enlarging the size of the original image up to *M*+*P*-1×*N*+*Q*-1 pixels.

2.2.4. Image Blurring in the Frequency Domain

Considering a discrete image *f*[*x,y*] of *M*×*N* pixels, the corresponding Discrete Fourier Transform (DFT) is expressed by:

$$F[u,v]=\sum_{x=0}^{M-1}\sum_{y=0}^{N-1} f[x,y]e^{-j2\pi(u\frac{x}{M}+v\frac{y}{N})}. \tag{2.15}$$

The inverse DFT is given by:

$$f[x,y]=\frac{1}{MN}\sum_{u=0}^{M-1}\sum_{v=0}^{N-1} F[u,v]e^{j2\pi(x\frac{u}{M}+y\frac{v}{N})}. \tag{2.16}$$

Note that *F*[*u,v*] is a complex matrix with a size of *M*×*N* elements, where the variables *u* and *v* are discrete spatial frequencies.

If we apply the convolution theorem to equation 2.14, which states that under suitable conditions the Fourier Transform of a convolution is the pointwise product of Fourier Transforms, we obtain:

$$g[x,y]=f[x,y]*h[x,y] \underset{DFT^{-1}}{\overset{DFT}{\rightleftarrows}} G[u,v]=F[u,v]\cdot H[u,v] \tag{2.17}$$

where *F*[*u,v*], *H*[*u,v*] and *G*[*u,v*] are defined as the DFT of the original image *f*[*x,y*], the PSF *h*[*x,y*] and the blurred image *g*[*x,y*] respectively.

The fact that the convolution in the frequency domain is an element to element product means that the two complex matrixes *F*[*u,v*] and *H*[*u,v*] must have the same size and, thus, also the original image *f*[*x,y*] and the PSF *h*[*x,y*]. If this is not the case, a zero-padding must be performed prior to calculating the DFT.

This method for calculating convolutions becomes of great importance, resulting in a considerable reduction in the computational power compared to the needed to compute the convolution directly. Besides, the fact that the convolution is defined as a point to point product of Fourier Transforms enables the possibility of recovering the original image—eliminate the introduced blur or distortion—just by means of a simple division:

$$G[u,v]=F[u,v]\cdot H[u,v] \Leftrightarrow F[u,v]=\frac{G[u,v]}{H[u,v]} \tag{2.18}$$

However, it has to be said that things are not really that simple, since—as explained in section 2.2.1—the problem can be ill-posed and this solution becomes unstable when $H[u,v]$ takes values close to zero or the blurred image $G[u,v]$ is slightly perturbed. In any event, it must be emphasized that the blur introduced by diffraction is totally reversible if certain conditions are met.

Figure 2.12 demonstrates the previously described entire process, where 2 different diffraction patterns have been used in parallel to blur an image: a *sinc*^{2} type PSF (left) and an Airy Disk PSF (right). A pointwise multiplication has been performed using the Fourier

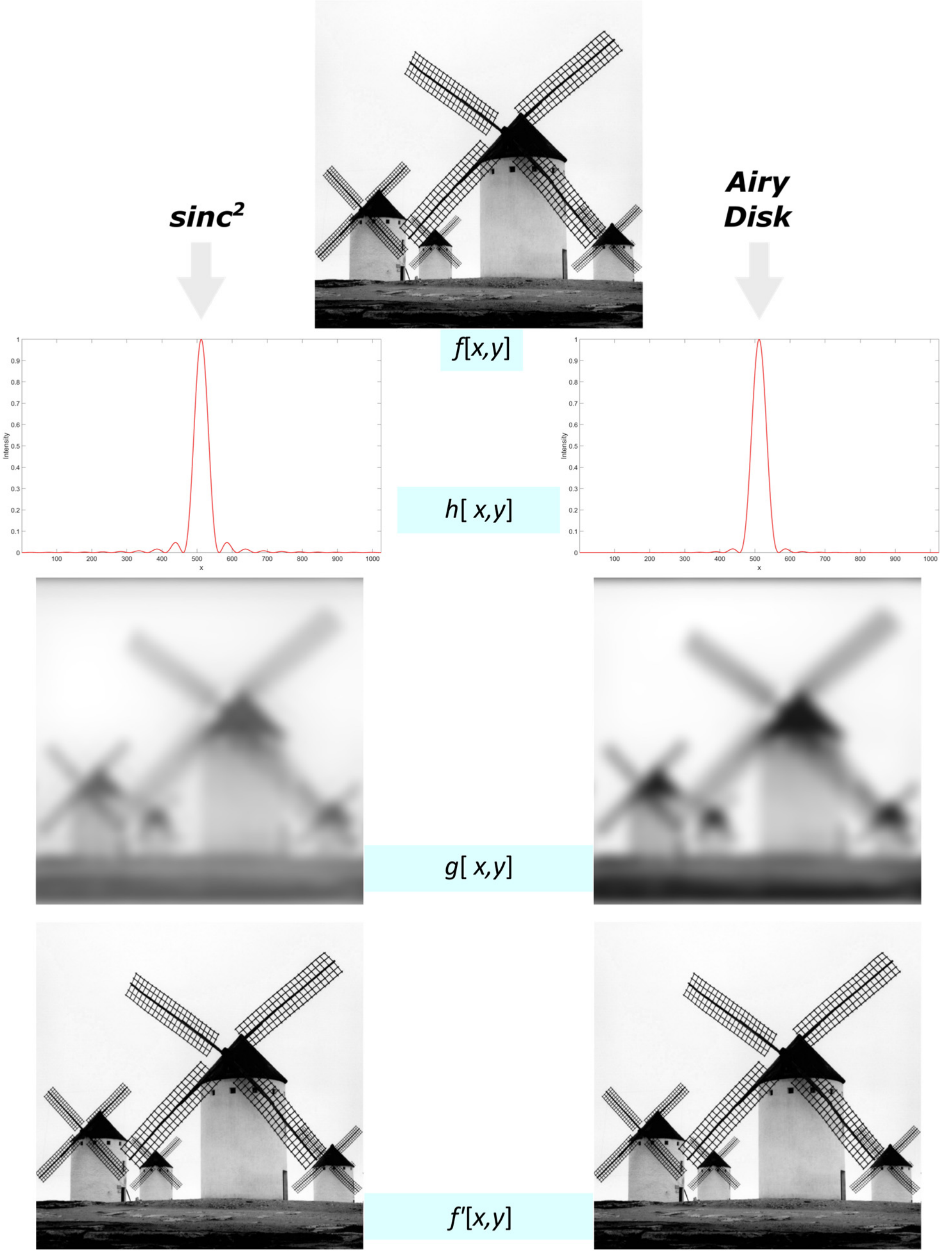

Figure 2.12. Image blurring and de-blurring process by multiplying Fourier Transforms, using *sinc*^{2} type (left) and Airy Disk (right) Point Spread Functions. Original image f (top center) and from top to bottom: cross sections of the PSF h through the central plane, blurred images g and recovered images f'.

Transforms of the original image *f* (at the top center) and the PSF, resulting in a distorted, blurred image. Subsequently, this blurred image has been divided (in the frequency domain) by the Fourier Transform of the PSF, recovering an estimation of the original image. Observe how the estimations *f'* obtained in the two cases—*sinc*^{2} and Airy Disk diffraction patterns—are accurate representations of the original image *f*.

In conclusion, we can say that the introduction of a controlled diffraction effect in an image is a totally reversible process, always subject to specific conditions. Therefore, this makes it possible to take advantage of other benefits produced because of diffraction, such as the spatial diversity or the lower signal sampling requirements. Additionally, it has been demonstrated that the election of a determined PSF over the other seems not to be such an important matter, since the diffraction effect produced on the image is somewhat similar and it can be reversed without any noticeable problem.

2.3. Image Sampling

In the field of Digital Signal Processing (DSP), the sampling procedure can be understood as the transition from continuous signals (also known as analog signals) to discrete signals (digital signals). The image capturing process can be considered as a sampling process: the real scene—a 2D continuous-space signal—observed by the imaging system is projected through the optical system onto the sensor and subsequently converted to a 2D discrete signal, a digital image.

The two-dimensional sampling function (a 2D impulse function) is constructed from Dirac delta functions as follows:

$$s[x,y]=\sum_{m=-\infty}^{\infty}\sum_{n=-\infty}^{\infty}\delta[x-mT_s,y-nT_s]\,. \tag{2.19}$$

By applying the sampling property, the sampled image is given by:

$$g[x,y]\cdot s[x,y]=\sum_{m=-\infty}^{\infty}\sum_{n=-\infty}^{\infty}g[mT_s,nT_s]\delta[x-mT_s,y-nT_s] \tag{2.20}$$

where T_s is the sampling interval and $f_s=\frac{1}{T_s}$ is the sampling frequency or rate.

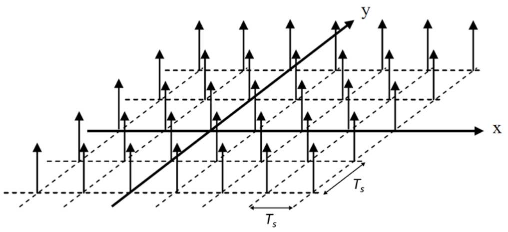

Figure 2.13. The sampling function.

In order to capture all the information in the sampling process, it must be satisfied the Nyquist-Shannon sampling theorem [60], which establishes a minimum sample rate f_s for a given band-limited signal (or image) with a maximum frequency f_{MAX}:

$$f_s > 2 f_{MAX} \tag{2.21}$$

Equivalently, for a particular sample rate f_s, the signal will be perfectly sampled for a maximum frequency $f_{MAX} < f_s / 2$, but not for higher frequencies.

The sampling process of a signal—or an image—generates multiples copies of the spectrum centered at multiples of f_s and combined by addition. Supposing $X[f]$ the spectrum of a band-limited signal ($X[f]=0$ for all $|f| \geq f_{MAX}$), if the sampling rate meets the Nyquist-Shannon theorem established in 2.21, the signal will be perfectly captured or reconstructed. However, if this theorem is not satisfied, the copies of the spectrum will be overlapped, creating an aliasing effect and corrupting the signal (observe Figure 2.14 for a better understanding).

Even if the Nyquist-Shannon sampling theorem can be applied to frequency band-limited (discrete) signals, its application is not so clear when considering continuous signals or images. Notice that the Fourier Transform of a continuous signal is an infinite sum of harmonics with an infinite bandwidth. Therefore, it is not possible to sample it satisfying the Nyquist theorem, since

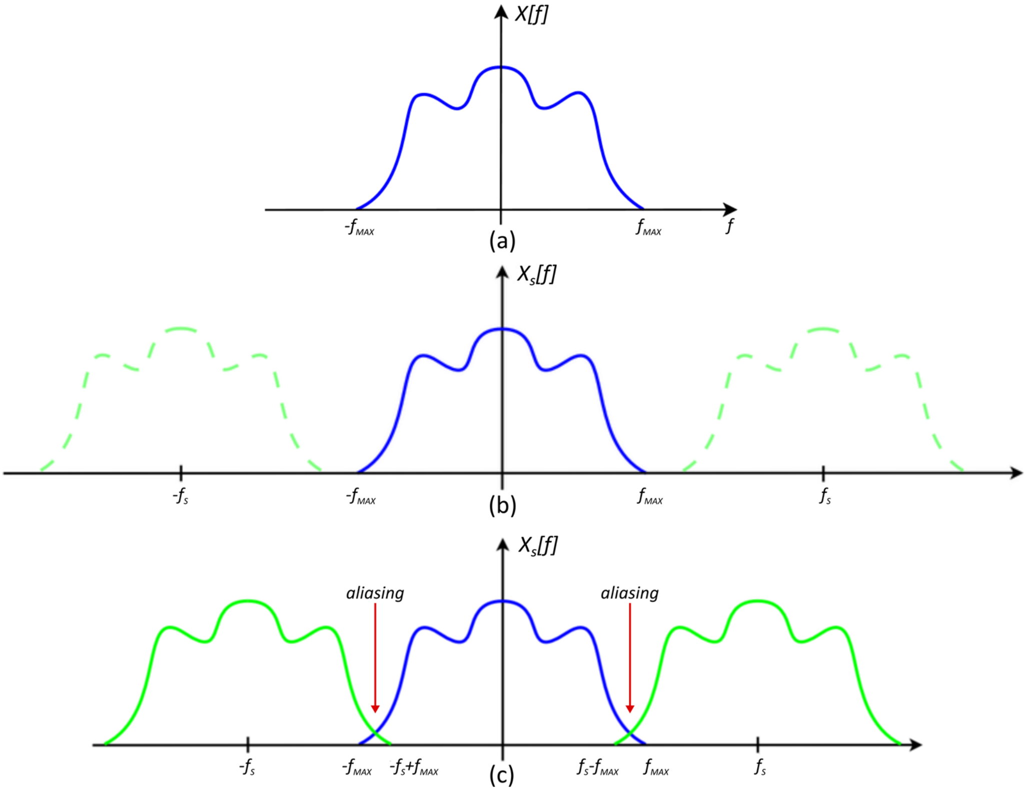

Figure 2.14. (a) Spectrum $X[f]$ of band-limited 1D signal. (b) Spectrum $X_s[f]$ of a correctly sampled signal ($f_s>2f_{MAX}$). (c) Spectrum $X_s[f]$ of an incorrectly sampled signal ($f_s<2f_{MAX}$): aliasing.

it would be required an infinite sampling rate f_s. In order to avoid aliasing, a low-pass filter (anti-aliasing filter) is used prior to the sampling process, which ensures that the signal is band-limited to a frequency f_{MAX}, where $f_{MAX}<f_s/2$.

2.3.1. The Sampling Process in Diffraction-Limited Systems

As mentioned in Chapter 1, in diffraction-limited imaging systems the diffraction pattern (PSF) and the size and separation of the sensors is what determines the maximum achievable resolution, and therefore, the maximum frequency. The separation between sensors is established by the Rayleigh criterion, being equivalent to the sampling interval T_s in terms of DSP.

The Full-Width at Half Maximum (FWHM) points can also be used to determine the minimum distance to resolve the PSF, which is nothing more than the width of the diffraction pattern measured between the points that are half the maximum amplitude. Figure 2.15 shows the FWHM of a Gaussian PSF and the minimum sampling intervals T_s=FWHM required to resolve contiguous points in diffraction-limited systems.

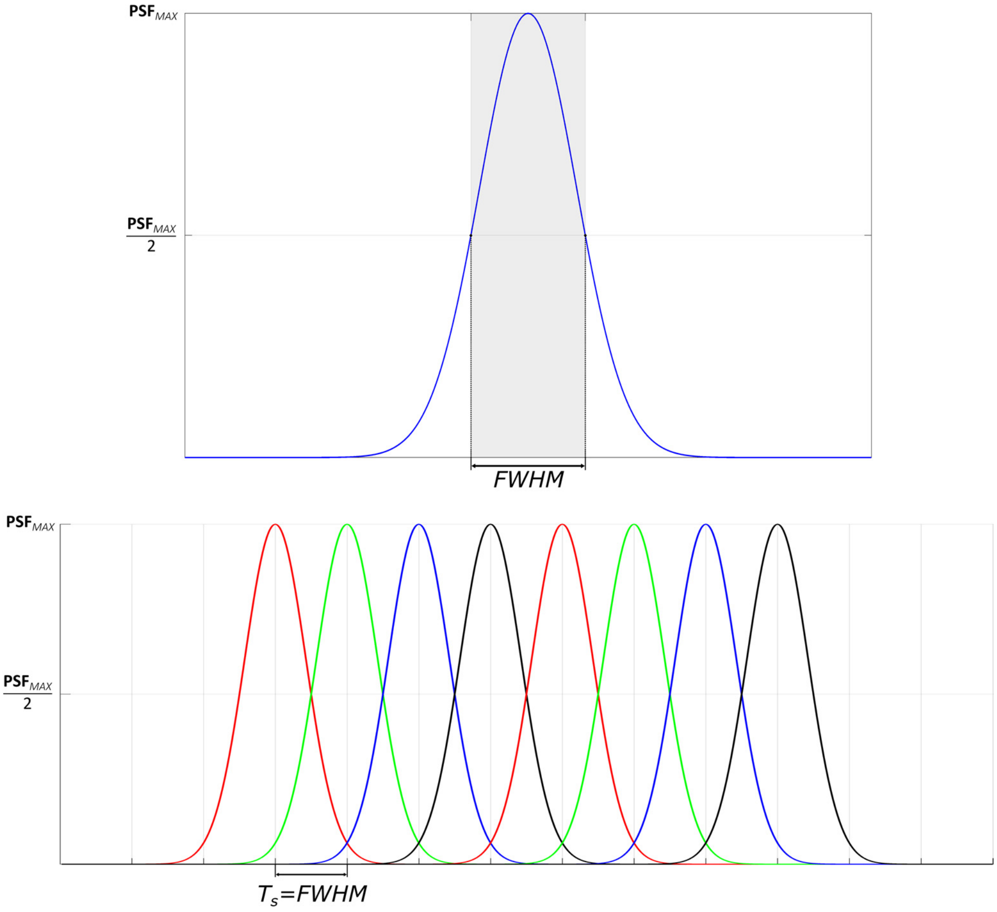

Figure 2.15. FWHM of a Gaussian PSF (top) and minimum sampling intervals T_s=FWHM in a diffraction-limited system.

Let us consider the 1D discrete signal of Figure 2.16 as the signal to be sampled by a diffraction-limited system. Observe how the signal envelope corresponds to a pulse train with a period *T* of 20 samples, where multiple zero values have been introduced randomly to generate high-frequency spectral components. The total signal length is of *N*=200 samples.

When sampling the signal using a diffraction-limited system with a Gaussian PSF of FWHM=5 samples (Figure 2.17 top) the sampling interval T_s must also be of 5 samples, resulting in a signal with a total length of N_s=40 samples (see Figure 2.17 bottom). Observe how the signal envelop (corresponding to the lower frequencies) is captured, but high frequency components are lost, since the maximum frequency is limited by the sampling interval T_s.

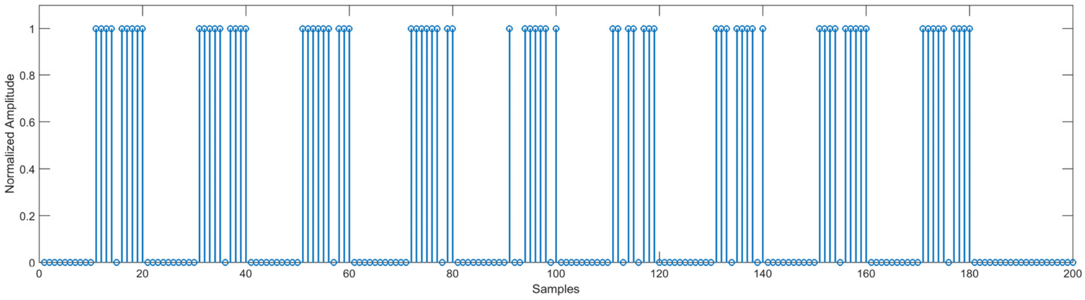

Figure 2.16. 1D discrete signal.

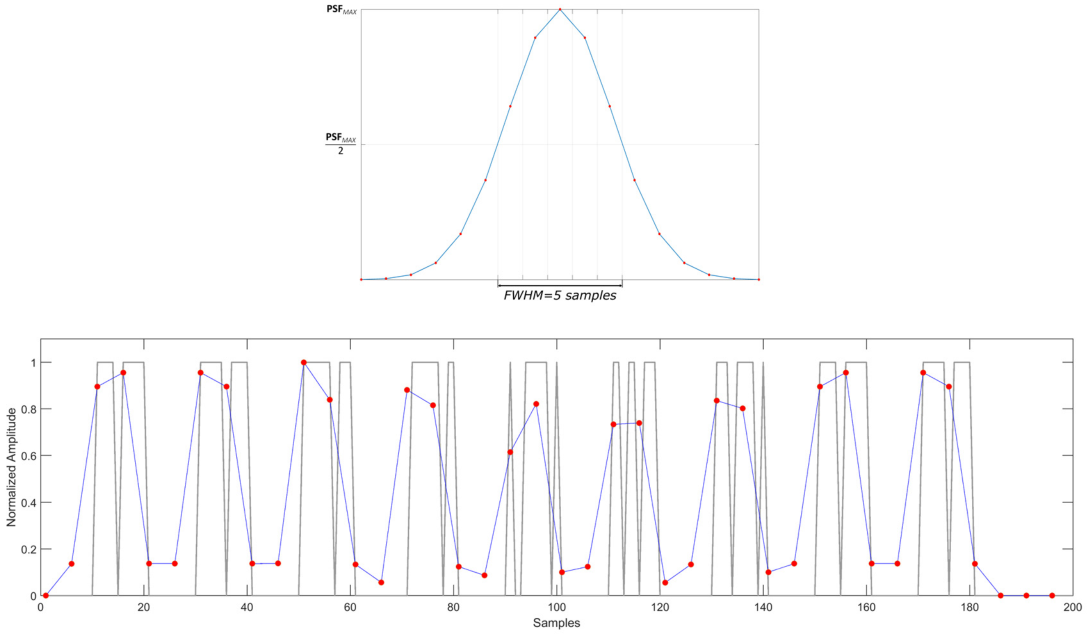

Figure 2.17. Gaussian PSF with FWHM=5 samples (top). Signal sampled by a diffraction-limited system N_S=40 samples (red markers), compared to the original signal (grey).

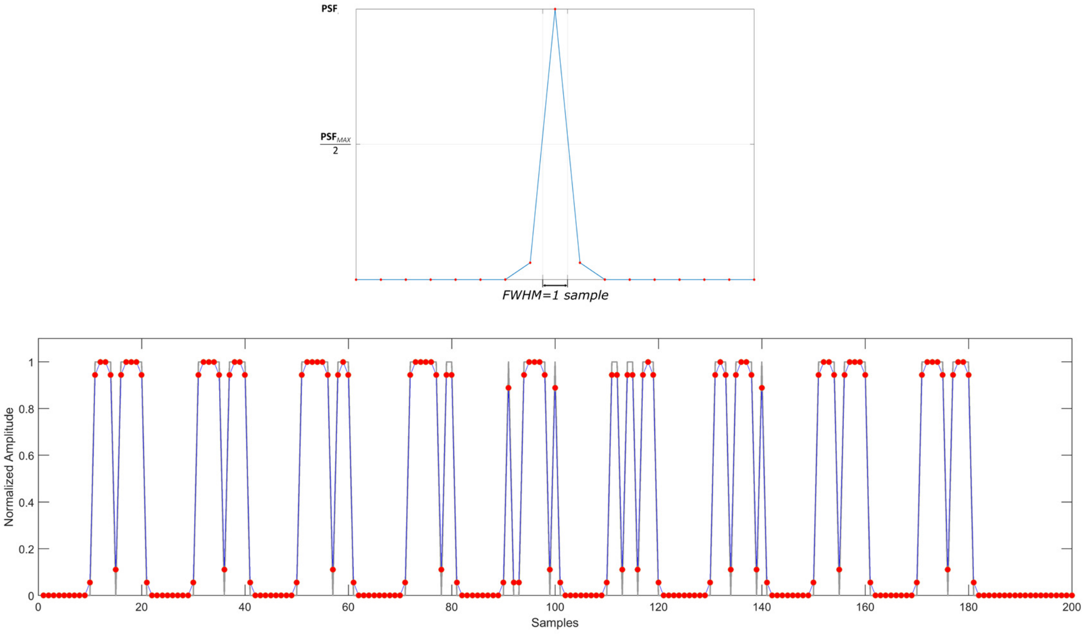

Figure 2.18. Gaussian PSF with FWHM=1 sample (top). Signal sampled by a diffraction-limited system N_S=200 samples (red markers), compared to the original signal (grey).

The only way to capture high-frequency components is to reduce the sampling interval and, thereby, the PSF must be also narrower. Figure 2.18 shows the result of sampling the same signal but using a PSF with a FWHM of 1 sample and equal scanning steps T_s. In this case, the signal is perfectly captured—even if sharp edges are slightly softened—and all the spectral components are correctly sampled.

It can be concluded from this section that in diffraction-limited systems, what determines the maximum frequency of the captured signal is the sampling frequency f_s, given the Nyquist-Shannon theorem, which establishes that $f_{MAX}<f_s/2$. This sampling interval set by the FWHM of the PSF must be fully satisfied if a clear and sharp signal must be captured, because in this way, most of the energy concentrated in the main lobe of the PSF is captured by a single sensor or sample. In the case of sampling at smaller intervals, neighboring samples would be affected creating a blurring effect on the captured signal produced by the diffraction pattern.

2.4. Signal Oversampling

It has become clear that when sampling signals or images, the maximum frequency is established by the sampling interval T_s, the reciprocal of the sampling frequency f_s. This condition based on the Nyquist-Shannon theorem makes it impossible to detect, recover or even reconstruct any spectral component above this frequency. Starting out from this premise, the only possible way to overcome this limit is to increase the sampling frequency, or analogously, to decrease the scanning intervals: oversample the signal. In DSP, oversampling is the process of sampling a signal (or an image) using a sampling rate significantly higher than the sampling frequency established by the Nyquist rate.

In first instance, the signal would be blurred due to the overlapping effect produced by contiguous PSF, but the total number of samples would be higher because of an increase in the sampling rate. Nevertheless, as explained in section 2.2, the introduction of a controlled diffraction in a signal or image is totally reversible if certain conditions are met.

The discrete signal shown in Figure 2.16 has been sampled at intervals of T_s=1 sample and using a Gaussian PSF with FWHM=5 samples by means of a point-to-point product of Fourier Transforms. The result is a signal with a total length of N_s=200 samples (the same length as the original signal), but with smooth and slow transitions, since high-frequency spectral components are considerably attenuated due to the LPF introduced by the PSF (Figure 2.19). This distortion would be appreciated as a blurring effect when applied to 2D images.

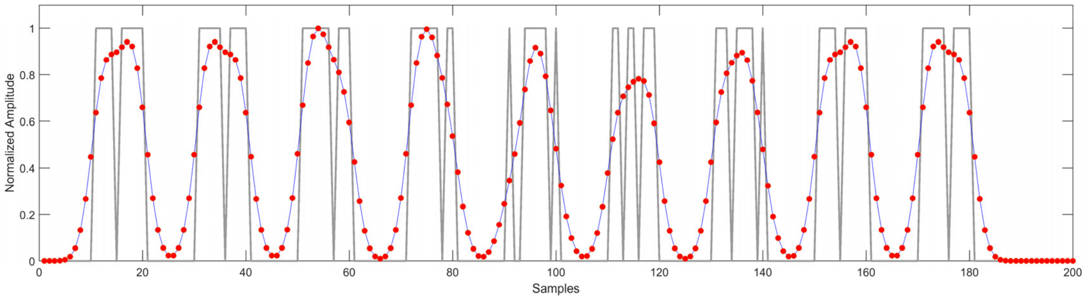

Figure 2.19. 1D discrete signal (grey) sampled at sampling intervals T_s=1 sample using a PSF of FWHM=5 samples (red markers).

2.4.1. Oversampling through Interpolation

In some cases, it is not feasible to reduce the sampling intervals as much as required to obtain a specific number of samples. This particular situation may occur, for example, when a given system (e.g., an imaging device) has a limited number of sensors and it is not possible to configure neither the sampling intervals nor the number of samples acquired by the system. The way to generate new samples between the captured data points is to perform an interpolation process.

On this point, it is of great importance to create the new points with high accuracy because small estimation errors would directly affect the stability of the system if an inverse filter is required. Nevertheless, the introduction of a controlled diffraction at a previous stage makes possible a more precise interpolation, as the signal presents slower variations and smooth transitions when compared with the same signal, but in absence of diffraction. This idea is depicted in figure 2.20 for better visualization: on the upper part of the image, an original test signal (sharp, diffraction-free) has been interpolated (red markers) by means of a cubic

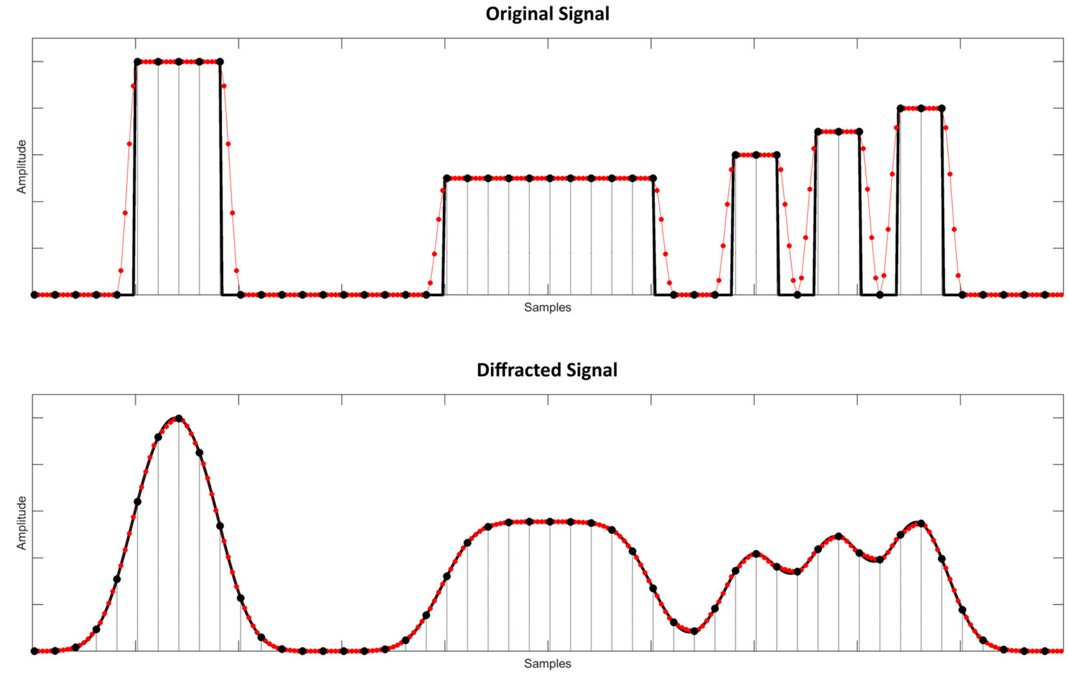

Original Signal

Diffracted Signal

Figure 2.20. Cubic interpolation of a diffraction-free (top) and a diffracted signal (bottom).

interpolation method; at the bottom part, a controlled diffraction has been introduced to the original test signal and then it has been interpolated in an identical manner. Observe how the interpolation is much more accurate in the presence of diffraction, thanks to the slow and smooth variations of the signal.

Taking advantage of this fact, we could sample the signal in Figure 2.16 at sampling intervals of T_s=2 samples (resulting in a signal length of N_s=100 samples) and then interpolate it in order to generate new intermediate data points up to 200 samples. As it is shown in Figure 2.21, the result is very similar to the one achieved by oversampling the signal at intervals of T_s=1 sample and depicted in Figure 2.19.

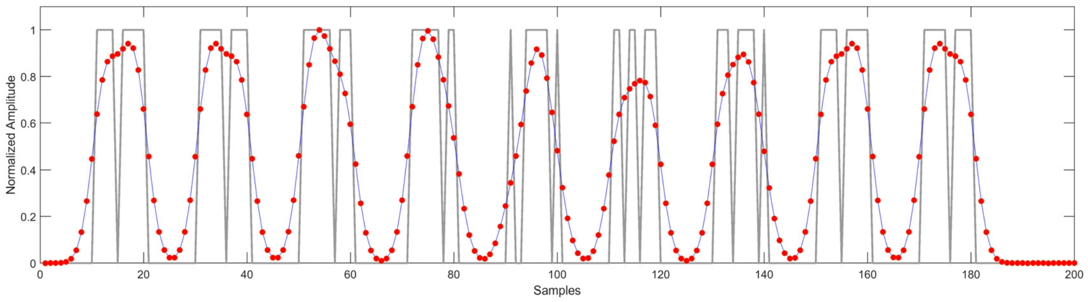

Figure 2.21. 1D discrete signal (grey) sampled at sampling intervals T_s=2 samples using a PSF of FWHM=5 samples and subsequently interpolated (red markers).

In brief, whether by oversampling the signal using small sampling intervals or implementing an interpolation process to generate new data points, the result is a blurred signal with an increased number of samples widely exceeding the sampling rate determined by the Nyquist criterion and, therefore, being possible to recover or reconstruct spectral components at higher frequencies. However, for this purpose it would be necessary to apply some inverse filtering or de-blurring process.

2.5. The Inverse Problem

Inverse problems are usually related to the estimation of certain data starting from indirect measurements—or captures—of information. In short, it involves the use of some deconvolution or inverse filtering method to estimate a signal as accurately as possible. This issue is a matter of great importance in multiple scientific and industry applications, such as:

- Medicine (tomography, ultrasonic, nuclear imaging).
- Communication systems.
- Radar systems.
- Antenna measurement and characterization.
- Seismology.
- Astronomical observation systems.
- Security systems.
- Remote sensing.
- Imaging systems.

Even if some authors [61] define the deconvolution process as the operation of removing the distortion or undesired effects caused by a linear filtering, in our case, the distortion will be introduced deliberately in order to take advantage of it as illustrated in previous sections. In any event, the main purpose of inverse problems is to remove a particular type of distortion to recover or estimate some specific information, usually in the presence of noise.

Let us consider the equation 2.22, where $g[n]$ refers to the measured data, $h[n]$ is the voluntarily or involuntarily introduced distortion (e.g., the PSF) and η represents some form of additive noise. In terms of DSP, the deconvolution process is defined as estimating an approximation of $f[n]$ from the observation $g[n]$ and the knowledge of the degradation introduced by the kernel $h[n]$, so that η is reduced to a minimum. It is assumed that the knowledge of the noise η is limited because of its statistical nature.

$$g[n]=f[n]*h[n]+\eta \tag{2.22}$$

The signal discretization required by digital processing often leads to a troublesome ill-posedness in matrix equation inversions, which means that the operator $h[n]$ does not tolerate the inverse operation or is near singular. This condition makes the system to be highly sensitive to the presence of noise or slight modifications in the observed signal *g*[*n*], producing significant errors in the estimation or even threatening the stability of the whole system. In order to cope with this challenge, several deconvolution and inverse filtering methods exist in literature, which can be classified in two main groups: deterministic and statistical approaches.

The application of deterministic methods requires the knowledge of the observation *g*[*n*] and the kernel *h*[*n*]. The most simple and direct option is to perform the division by the Fourier Transform of the kernel in the frequency domain, but zero values of the kernel can lead to stability problems which must be confronted especially in presence of noise [62]. This group includes also iterative methods, that present problems related to stability and convergence [63] or pseudoinverse solutions and approaches based on singular value decomposition [64], where unstable solutions can be generated due to ill-conditioned formulations. Time or space-domain methods can work well, but these can be approximate solutions, often presenting stability problems and excessive computational cost [65], [66].

On the other hand, statistical methods assume certain knowledge about the kernel *h*[*n*] in advance, but their effective functioning is determined by the used statistical model. In this group are included methods based on the Wiener filter [67]–[70] and also polynomial solutions with certain optimality criteria when deconvolving noisy signal observations [71], [72].

As can be observed, there are multiple approaches to solve the inverse problem connected to 1D signal deconvolution or image restoration techniques in the case of 2D signals. Part of these methods are focused on solving the inverse problem in the time-space domain, but others operate in a transformed domain. Some of the most well-known inverse methods are outlined in detail below for a better understanding of the subsequent chapters.

2.5.1. The Singular Value Decomposition. Regularization Methods

One of the methods to deal with the stability of inverse problems is the Singular Value Decomposition (SVD) [73]. In general, for any matrix $A \in \mathbb{R}^{m\times n}$ the SVD takes the form

$$A = U \sum V^T , \tag{2.23}$$

where the matrices $U = (u_1,...,u_n)$ and $V = (v_1,...,v_n)$ consist of the left and right singular vectors, and both matrices are orthogonal ($U^T U = V^T V = I$).

The central matrix $\sum$ is a diagonal matrix where the diagonal elements σ_i are defined as the singular values of *A*, which are nonnegative and ranked in decreasing order:

$$\sigma_1 \geq \sigma_2 \geq ... \geq \sigma_n \geq 0 . \tag{2.24}$$

The solution to the linear system $Ax = y$ can be expressed by means of SVD:

$$x_{est} = \sum_{j=1}^{n} \frac{u_j^T y}{\sigma_j} v_j \qquad \forall \sigma_j > 0. \tag{2.25}$$

The system is well-posed if it is satisfied the condition:

$$\left\| x_{est} \right\|^2 = \sum_{j=1}^{n} \frac{\left| u_j^T y \right|^2}{\sigma_j^2} < \infty. \tag{2.26}$$

This condition will fail if $\sigma_j \to 0$, since a continuous dependence between the estimation and the observation cannot be guaranteed. In this case, the problem will be ill-posed.

From the above, it can be deduced that a system with the operator *H* will be ill-posed, when the singular values gradually decrease to zero and the ratio between extreme values is large.

$$cond(H) = \frac{\max\left\{\sigma_j\right\}}{\min\left\{\sigma_j\right\}}; \qquad \sigma_j > 0 \tag{2.27}$$

The previous ratio represents the condition number of *H*, and measures how much the output value of the function will be magnified when small changes in the input signal are produced. Therefore, if *cond*(*H*) presents too large values, the system becomes highly unstable and very sensitive to small modifications in the observation *g*[*n*], producing important errors when estimating an approximation of *f*[*n*].

The solution of equation 2.25 when an additive noise *η* is introduced in the system is given by:

$$x_{est} = \sum_{j=1}^{n} \frac{u_j^T y}{\sigma_j} v_j + \sum_{j=1}^{n} \frac{u_j^T \eta}{\sigma_j} v_j \qquad \forall \sigma_j > 0. \tag{2.28}$$

If *H=I*, it becomes a denoising problem and if *η=0*, instead, it will be a deblurring problem.

- ***TSVD Regularization***

Regularization algorithms are oriented to stabilize the computed solution, such that the system becomes less sensitive to different perturbations (e.g., noise). Regularization consists basically of the introduction of some information for the purpose of stabilizing the inverse problem.

The most natural way to regularize an inverse problem is based on the elimination of the most unstable singular values when the noise level is increased. This method is known as Truncated Singular Value Decomposition (TSVD) and consists in the reconstruction of the components with higher singular values (the most stable), while the components corresponding to the smallest singular values (the most unstable) are truncated or removed. This can be done by using a filter where a regularization parameter *α* must be chosen and acts as a threshold level for singular values. Thus, a filter ω_{α} is defined and it only allows the pass of singular values higher than *α*:

$$x_{est} = \sum_{j=1}^{n} \omega_{\alpha}(\sigma_j^2) \frac{u_j^T y}{\sigma_j} v_j \qquad \forall \sigma_j > 0 . \tag{2.29}$$

When the regularization parameter $\alpha \to 0$, the most unstable components are included in the deconvolution process. However, when $\alpha \to 1$ oscillations are represented by slow and smooth functions (sine and cosine functions). In short, the stability of the system depends to a large extent on the appropriate choice of the parameter *α*, but this is not a simple issue since it presents a compromise between the noise suppression and the loss of relevant information.

The TSVD method is possible for small problems, but as the problem size increases, it becomes prohibitive to compute the SVD and alternative regularization methods should be employed.

- ***Tikhonov Regularization***

This regularization algorithm was independently formulated by Phillips [74] and Tikhonov [75], but it is commonly recognized as Tikhonov regularization. The main idea is based on accepting a nonzero residual $Ax - y$ and in exchange obtain a smaller solution norm. The formulation of the problem is:

$$\min \left\{ \|Ax - y\|_2^2 + \lambda^2 \|x\|_2^2 \right\} \tag{2.30}$$

where *λ* is the regularization parameter to control the weight given to minimization of the solution norm $\|x\|_2$ relative to minimization of the residual norm $\|Ax - y\|_2$. When $\lambda \to 0$, the Tikhonov solution x_{λ} approaches the 'naive solution' $Ax = y$ (or the least squares solution, if *A* is rectangular). Instead, if $\lambda \to \infty$, then $x_{\lambda} \to 0$. However, there is a range of intermediate values of *λ* between both extremes, where the algorithm obtains approximations to the desired solution, producing a balance between the residual and solution norms.

Equation 2.30 does not fit numerical calculations and, therefore, normal equations are used to solve the least squares problem:

$$(A^T A + \lambda^2 I)x = A^T y . \tag{2.31}$$

The Tikhonov solution can also be expressed in terms of the SVD of *A* as follows:

$$x_{\lambda} = \sum_{j=1}^{n} \frac{\sigma_j^2}{\sigma_j^2 + \lambda^2} \frac{u_j^T y}{\sigma_j} v_j . \tag{2.32}$$

2.5.2. Convolution-Based Methods. Toeplitz Matrices

In linear algebra, a Toeplitz matrix is constant along diagonals [57]. Thus, an $n \times n$ Toeplitz matrix has the following form:

$$T = \begin{bmatrix} t_0 & t_{-1} & \cdots & t_{2-n} & t_{1-n} \\ t_1 & t_0 & t_{-1} & \ddots & t_{2-n} \\ \vdots & \ddots & \ddots & \ddots & \vdots \\ t_{n-2} & \ddots & t_1 & t_0 & t_{-1} \\ t_{n-1} & t_{n-2} & \cdots & t_1 & t_0 \end{bmatrix} . \tag{2.33}$$

Given a vector $f \in \mathbb{C}^n$, the matrix-vector product *T·f* has the discrete convolution form

$$[Tf]_i = \sum_{j=0}^{n-1} t_{i-j} f_i \,, \qquad i = 0,\ldots,n-1 \,, \tag{2.34}$$

where $t = (t_{1-n},\ldots,t_{-1},t_0,t_1,\ldots,t_{n-1}) \in \mathbb{C}^{2n-1}$. This situation is indicated by *T=toeplitz*(*t*).

An $n_x n_y \times n_x n_y$ matrix *T* is a Block Toeplitz with Toeplitz Blocks (BTTB) matrix, when it takes the block form

$$T = \begin{bmatrix} T_0 & T_{-1} & \cdots & T_{1-n_y} \\ T_1 & T_0 & T_{-1} & \vdots \\ \vdots & \ddots & \ddots & T_{-1} \\ T_{n_y-1} & \cdots & T_1 & T_0 \end{bmatrix} \tag{2.35}$$

where each block T_j is an $n_x \times n_x$ Toeplitz matrix.

This type of matrices transform 1D kernels (PSF) into a convolution matrix starting from a square Toeplitz matrix and symmetrical with respect to the main diagonal, which meets:

$$\forall h_{ij} \in H \,; \qquad h_{ij} = h_{i+1,j+1} \tag{2.36}$$

Considering an array $v \in \mathbb{C}^{n_x \times n_y}$, it can be transformed into a vector $\boldsymbol{v} \in \mathbb{C}^{n_x n_y}$ by stacking the columns of *v* and defining the linear operator ***vec***: $v \in \mathbb{C}^{n_x \times n_y} \rightarrow \boldsymbol{v} \in \mathbb{C}^{n_x n_y}$,

$$\boldsymbol{vec}(v) = [v_{1,1} \ldots v_{n_x,1} v_{1,2} \ldots v_{n_x,2} \ldots v_{1,n_y} \ldots v_{n_x,n_y}]^T \,, \tag{2.37}$$

which corresponds to lexicographical column ordering of the components in the array *v*. the symbol ***array*** is defined as the inverse of the ***vec*** operator,

$$\boldsymbol{array}(\boldsymbol{vec}(v)) = v \,, \qquad \boldsymbol{vec}(\boldsymbol{array}(\boldsymbol{v})) = \boldsymbol{v} \,, \tag{2.38}$$

supposing $v \in \mathbb{C}^{n_x \times n_y}$ and $\boldsymbol{v} \in \mathbb{C}^{n_x n_y}$.

At this point, the block Toeplitz matrix-vector multiplication can be related to discrete 2D convolution expressed as:

$$t * f = \boldsymbol{array}(T\,\boldsymbol{vec}(f)), \tag{2.39}$$

defining *T* as a $n_x n_y \times n_x n_y$ BTTB matrix.

The matrix-vector representation of a discrete and noisy data model is given by:

$$\boldsymbol{g} = T\boldsymbol{f} + \boldsymbol{\eta}, \tag{2.40}$$

where *T*=*bttb*(*t*) is considered the blurring matrix (PSF), **g**=***vec***(*g*) is the measured distorted signal, ***f***=***vec***(*f*) is the original signal and ***η***=***vec***(*η*) is the predominantly Gaussian error term (noise). Given *T* and **g**, the aim is to estimate ***f***.

The direct use of this algorithm to solve a convolution system generates problems associated to stability due to ill-posed nature. Therefore, it requires the use of regularization techniques to produce more stable and adequate results, such as the Tikhonov functional with a quadratic penalty term:

$$T_\alpha(\boldsymbol{f}) = \frac{1}{2}\left\|T\boldsymbol{f} - \boldsymbol{g}\right\|^2 + \frac{\alpha}{2}\boldsymbol{f} * L\boldsymbol{f}, \tag{2.41}$$

considering the symmetric positive definite penalty matrix *L* and the regularization parameter $\alpha > 0$. In order to solve the linear system, T_α must be minimized and the system is transformed into the following formulation:

$$(T * T + \alpha L)\boldsymbol{f} = T * \boldsymbol{g} \tag{2.42}$$

2.5.3. Fourier-Based Methods

In general, a blurring system is considered to be linear and spatially invariant, which is basically a Linear Time-Invariant (LTI) system. In this context, Fast Fourier Transform (FFT) based schemes become greatly efficient methods for computational image restoration. Nevertheless, real images have properties that cannot always be handled by linear methods, e.g., images consist of positive light intensities captured by sensors, and thus nonnegativity constraints should be imposed when implementing DSP methods. The incorporation of these constraints and other information have been suggested in multiple applications leading to substantial improvements in inverse problem approaches. However, these constraints can be excluded from multiple implementations since they can lead to non-linear problems with demanding computational cost requirements [76].

The model for a discrete implementation is defined by the convolution:

$$g[x,y]=f[x,y]*h[x,y]+n[x,y] \tag{2.43}$$

where $f[x,y]$ is the original image, $h[x,y]$ the PSF, $n[x,y]$ additive noise and $g[x,y]$ is considered the measured data. The equivalent model can be represented in the frequency domain applying the DFT to each term from equation 2.43 as follows:

$$G[u,v]=F[u,v]\cdot H[u,v]+N[u,v] \tag{2.44}$$

An inverse filter is a linear filter $h_{inv}[x,y]$ which can be defined as the convolutional inverse of the blurring function or PSF $h[x,y]$ and meets

$$h_{inv}[x,y]*h[x,y]=\delta[x,y], \tag{2.45}$$

where

$$\delta[x,y]=\begin{cases}1, & \text{if } x=y=0\\ 0 & \text{elsewhere}\end{cases} \tag{2.46}$$

The inverse filter can also be expressed in the discrete frequency domain by:

$$H[u,v]\cdot H_{inv}[u,v]=1. \tag{2.47}$$

This filters are practically impossible to design when considering the space-variant distortion [77]. Hence, from now on only the space-invariant case will be taken into consideration.

If the blurred image—the captured data $g[x,y]$—is filtered with the above described inverse filter, the output will be an estimation of the original signal $f[x,y]$ and the DFT is determined by:

$$\begin{aligned}F'[u,v]&=H_{inv}[u,v]\;G[u,v]\\ &=H_{inv}[u,v]\;\left[H[u,v]\;F[u,v]+N[u,v]\right]\\ &=F[u,v]+H_{inv}[u,v]\;N[u,v].\end{aligned} \tag{2.48}$$

It can therefore be deduced that the recovered estimation $f'[x,y]$ is thus equal to the original image to which the inverse filtered noise is added.

Unfortunately, the inverse filtering in the frequency domain is not as straightforward as it might appear. First of all, the inverse filter may not exist if $H[u,v]$ comes from an ideal LPF or if it takes null values at selected frequencies. Additionally, problems associated to an excessive noise amplification may occur, since most of the power spectrum in the blurred image is usually concentrated at low frequencies and decreases for high ones. Oppositely, the spectrum of the additive noise $N[u,v]$ typically contains considerably more high frequency spectral components. Thus, at high frequencies, the estimation $F'[u,v]$ is dominated by the inverse filtered—amplified—noise, which yields unsatisfactory solutions and results. In some cases, the blurring function or PSF is not known with the required precision adversely affecting the realization of the inverse filter $H_{inv}[u,v]$ and resulting in an intolerable uncertainty. As a final note, it can be mentioned that the inverse filter suffers because it makes no use of the properties of the measured data $g[x,y]$.

2.5.4. Least-Squares Methods. The Wiener Filter

There exist a set of restoration filters called least-squares filters and specially created to overcome the stability or noise amplification problems connected to the inverse problem. One of the most widely used is the Wiener filter [64], a linear space-invariant filter which takes advantage of the power spectrum of both the image and the noise to avoid and control the excessive noise amplification [77].

The frequency response of the Wiener filter H_w[u,v], is determined to minimize as much as possible the Mean Squared Error (MSE) in the restoration process given by:

$$\begin{aligned} E_2 &= E(|F[u,v]-F'[u,v]|^2) \\ &= E(|F[u,v]-G[u,v]\,H_w[u,v]|^2), \end{aligned} \tag{2.49}$$

considering $E(\cdot)$ as the expectation over a group of images.

The solution to this minimization problem can be described by:

$$H_w[u,v]=\frac{H^*[u,v]}{|H[u,v]|^2+\dfrac{S_{nn}[u,v]}{S_{ff}[u,v]}} \tag{2.50}$$

where $S_{ff}[u,v]$ represents the power spectrum of the original image, $S_{nn}[u,v]$ is the power spectrum of the noise and $H^*[u,v]$ corresponds to the complex conjugate of $H[u,v]$. In absence of noise, the Wiener filter behaves as the following pseudo-inverse filter:

$$H_{ps}[u,v]=\begin{cases} \dfrac{1}{H[u,v]} & \text{for } H[u,v]\neq 0 \\ 0 & \text{for } H[u,v]=0 \end{cases} \tag{2.51}$$

2.5.5. Iterative Methods

Image restoration algorithms based on iterative methods can be greatly efficient both for spatially variant and invariant distortions, including a wide variety of regularization techniques and multiple boundary conditions. Due to the fact that there is no optimal standard procedure for all image deconvolution problems, the study of iterative methods has long been an active and important research topic [59], [77], [78].

One of the main motivations for the use of iterative procedures is the existence of mechanisms oriented to limit the set of possible solutions for the inverse problem by requiring a closed convex space where these solutions must be found. The computational load of an iterative method depends on the amount of operations performed in each iteration, such as the necessary number of iterations to ensure the quality of the image restoration. While different techniques exist to speeding up the convergence of the method, e.g., pre-conditioning strategies, they must be used meticulously, since they may lead to an erroneous convergence behavior. A critical issue for iterative methods is the development of solid stopping criteria to produce consistent results.

Generally, iterative methods are structured as follows:

```
$\mathbf{x}_0$ = initial estimation of $\mathbf{x}$
for k = 0,1,2…
        ▪ $\mathbf{x}_{k+1}$ = computations involving $\mathbf{x}_k$, H, a preconditioner matrix P and other intermediate parameters.
        ▪ Check the if the stopping criteria is satisfied.
end
```

The computational operations implemented to update x_{j+1} at each iteration depend directly on the specific iterative scheme used, but the most intensive computations usually involve matrix-vector products and the solution of linear systems with the kernel H, the transpose matrix H^T and the preconditioner matrix P.

Preconditioning is used to accelerate the rate of convergence of iterative methods. Although there is an additional computational cost, the number of iterations needed to compute a good approximation of the solution can be reduced drastically, resulting in a considerable decrease in the overall cost of the iterative scheme. The speed of convergence of one iterative method is normally determined by certain spectral properties of the kernel H. Therefore, preconditioning consists on modifying these spectral properties to accelerate convergence and is often presented in the context of solving the linear systems such as the one defined by $Ax = y$. The standard approach is to construct a preconditioning matrix P that meets the following properties:

- The construction of P should be computationally affordable.
- The solution of the linear system $Pz = w$ should be relatively inexpensive.
- The preconditioned system needs to satisfy $P^{-1}A \approx I$ in the sense that the singular values of $P^{-1}A$ are clustered around 1.

The first two properties are connected to the additional computational load produced by preconditioning and the last requirement determines the speed of convergence: the more singular values clustered around 1, the faster the convergence.

The construction of effective preconditioners is a well-known field [79], [80]. However, when the problem is ill-posed, preconditioning can generate an erratic convergence behavior which results in fast convergence to an inappropriate solution. In this respect, some research work has been carried out to overcome these difficulties [81], [82]. As in earlier instances, for ill-posed problems, regularization can be incorporated and therefore the previous formulation may require some modifications. If Tikhonov regularization is applied, the standard approach outlined above is defined by the linear system $\hat{A}x = \hat{y}$, where

$$\hat{A} = \begin{bmatrix} A \\ \lambda L \end{bmatrix}, \quad \hat{y} = \begin{bmatrix} y \\ 0 \end{bmatrix} . \tag{2.52}$$

Nevertheless, when regularization is implemented by truncating iterations, the process can be a bit more delicate. The first iterations tend to reconstruct mostly the good part of the solution, while noise components are filtered out. These iterations are the ones that must be accelerated. At a particular point, the system starts to reconstruct noise components and the following iterations are corrupted, being this part of the iteration which should not be accelerated.

- ***Van Cittert Deconvolution***

The Van Cittert iterative deconvolution algorithm [83] is one of the most simple methods and, although it was originally formulated for the space-invariant case, it can also be applied to the spatially-variant case.

If the contribution of noise is ignored and using the compact matrix-vector notation, it can be defined the following identity, which must be met for all values of the parameter β:

$$f = f + \beta(g - Hf) . \tag{2.53}$$

If the method of successive substitutions is applied:

$$\begin{aligned} \hat{f}_0 &= \beta g \\ \hat{f}_{k+1} &= \hat{f}_k + \beta(g - H\hat{f}_k) \\ &= \beta g + (I - \beta H)\hat{f}_k \\ &= \beta g + R\hat{f}_k \end{aligned} \tag{2.54}$$

where *I* is defined as the identity operator.

An aspect of great importance in any iterative algorithm is the convergence and, if it is produced, to what limiting solution. By direct enumeration it can be seen that

$$\hat{f}_k = \beta \sum_{r=0}^{k} R'g\,, \tag{2.55}$$

which can also be written as

$$\hat{f}_k = \beta(I-R)^{-1}(I-R^{k+1})g\,, \tag{2.56}$$

on the assumption that the matrix $(I-R)$ is revertible, that is to say, the kernel H is invertible. Finally, if the condition of convergence

$$\lim_{k\to\infty} R^{k+1} g = 0 \tag{2.57}$$

is met, then the limiting solution is given by

$$\hat{f}_\infty = \lim_{k\to\infty} \hat{f}_k = \beta(I-R)^{-1} g = H^{-1} g\,, \tag{2.58}$$

and this is the inverse filter solution. Therefore, implementing iterations indefinitely will generate a solution with multiple inadequate properties. However, the iterative application of the inverse filter has some advantages over the direct implementation: first, it can be finished prior to convergence, obtaining in a partially deblurred or restored image, but in absence of noise amplification. Moreover, it is not necessary to implement the inverse operator, since each iteration requires only the blurring operator itself.

- ***Richardson-Lucy Algorithm***

The Richardson-Lucy deconvolution algorithm was developed from Bayes' theorem [84], [85] and it became popular in the fields of astronomy and medical imaging due to its implementation of maximum likelihood and the ability to reconstruct images of high quality in presence of high noise levels [86].

This algorithm takes into account statistical fluctuations in the signal and this is why it has the ability to reconstruct noisy images. The inverse relation of the iterative algorithm in terms of convolution is given by:

$$f_{j+1}(x) = \left\{ \left[\frac{g(x)}{f_j(x) * h(x)} \right] * g(-x) \right\} f_j(x) \tag{2.59}$$

where (*) is the convolution operation. As the PSF $h(x)$ is known, the object $f(x)$ has to be found by iterating equation 2.59 until it converges. First of all, an initial estimation is required for the object $f_0(x)$ to start the algorithm. Then, the form of the algorithm produces the rapid loss of large deviations in the guess from the true object in initial iterations, whereas small details are solved more slowly in subsequent iterations. The Richardson-Lucy method presents multiple advantages, as the nonnegativity constraint if the initial guess $f_0(x)\geq 0$ or the conservation of energy as iterations proceed.

2.6. General Overview of the Visual Hyperacuity Simulation Method

Once the main characteristics and particularities of each step of the visual hyperacuity simulation method have been analyzed, it may be worth taking an overview of the whole system, linking the different stages of the process. As already explained, the human eye uses a low number of sensors to capture images and, moreover, the retinal image seems to be blurred because of diffraction. The developed method intends to improve the final image resolution when the number of available sensors is limited, using a controlled diffraction effect introduced at the beginning of the process, as the human eye does based on our hypothesis. In short, it can be understood as an explanation and simulation of the visual hyperacuity, a diffraction-enhanced system, far from conventional imaging devices, widely known to be diffraction-limited. The block diagram of the whole system can be observed in Figure 2.22.

For a better comprehension and interpretation, the method will be described step by step with the aid of images and observing how they are transformed at each stage.

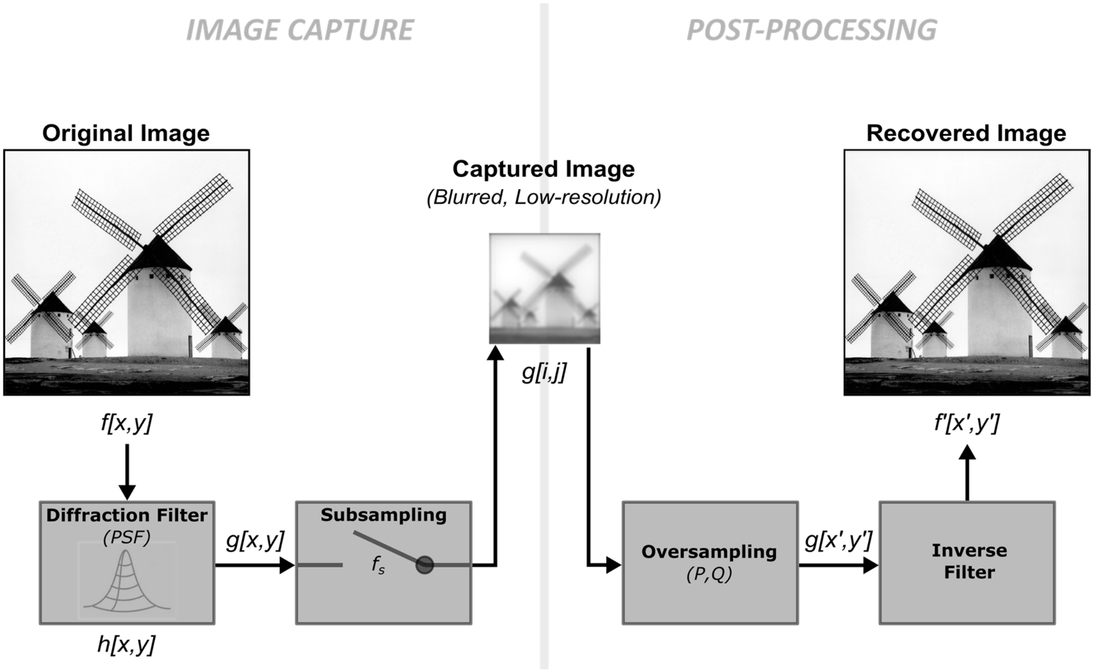

Figure 2.22. Block diagram of the visual hyperacuity simulation method: original image (observed real scene), captured image (input image) and recovered image (estimation).

Figure 2.23. Original test image used for simulation, reproducing the high-resolution real scene.

The original test image (Figure 2.23) is used as a model of the real scene observed by the imaging system and, as such, it is conceived as a high-resolution image at the entrance of the optical system. Ideally, it should be a continuous image with an infinite resolution (and bandwidth), but it is not possible if we start from a digital (discrete) image. In view of this fact, it must be clear that it is unthinkable to go beyond this initial resolution, whatever image restoration method is used.

The first step of the approach consists in introducing a known diffraction (PSF) at the entrance of the system. Its main effect is producing a blurring effect in the incoming image (observe Figure 2.24 a), the one projected over the sensors. Subsequently, the diffracted image is spatially subsampled (Figure 2.24 b), which aims to simulate the reduced number of sensors used for image capturing. The result of the subsampling process would be the input image, the one captured by the imaging device: a blurred and low-resolution image (Figure 24 c).

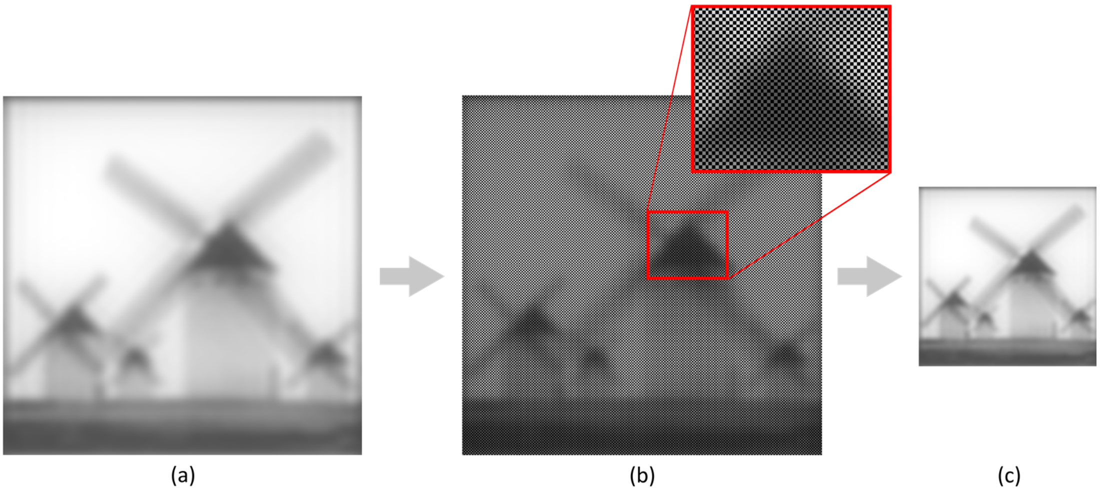

Figure 2.24. (a) Blurred image projected over the sensors. (b) Subsampling process. (c) Input image: blurred and low-resolution.

On the next stage the image goes through an interpolation process, increasing the total data points, thus, creating new samples between the existing ones. The interpolated image is still blurred (see Figure 2.25), but the image size is increased. The LPF (diffraction) introduced in advance makes possible a more accurate interpolation, because the blurred image presents low-variation and smooth transitions and a more precise estimation of new image data points is performed.

Figure 2.25. Interpolated image.

The last stage of the visual hyperacuity simulation method is the application of an inverse filter or deconvolution to remove the blur introduced by the diffraction to recover a sharp and focused image with an enhanced resolution in comparison to the one captured by the sensor (Figure 2.26). It is worth mentioning that the inverse problem is ill-posed and thus the inverse filtering becomes highly unstable, presenting noise amplification problems and high sensitivity against errors produced by interpolation. In this case, the effects of noise have not been considered and small errors in the recovered image are produced due to inaccuracies produced in the interpolation process.

Figure 2.26. Recovered image.

2.7. Conclusions

It has been shown how the introduction of a controlled diffraction at a first stage reduces considerably the sampling requirements for signal capturing, allowing the use of less sensors, due to the fact that it acts as an anti-aliasing filter. Nevertheless, it must be clear that, based on the Nyquist theorem, when capturing both signals or images the maximum frequency is established by the sampling interval or equivalently the sampling frequency, and it is not possible to detect or even recover any spectral component above this cutoff frequency.

In the case of diffraction-limited systems, the sampling interval is set by the PSF and a minimum sampling distance must be met in order to prevent from affecting neighboring samples and producing a blurring effect, if a clear and sharp image has to be captured. The only way to improve the image resolution or capture higher frequencies involves the generation of a narrower PSF and increasing the sampling rate.

The proposed method takes advantage of diffraction to improve the final image or signal resolution, far from being a diffraction-limited system. On the one hand, we can oversample the signal with sampling intervals smaller than those established by the Rayleigh criteria, creating an overlapping effect. On the other hand, when the number of sensors is limited and it is not possible to configure neither the sampling intervals nor the number of captured samples, the introduction of a controlled diffraction prior to sampling makes possible an accurate interpolation to generate new samples. In both cases, the captured signal is blurred due to the diffraction produced by the PSF. However, the increased number of samples widely exceeds the sampling rate determined by the Nyquist criterion and, therefore, it is possible to recover or reconstruct spectral components at higher frequencies even if some inverse filtering or deconvolution needs to be applied.

On the negative side, it must be noted that the inverse problem is often ill-posed and the system becomes highly sensitive to the presence of noise or slight modifications in the blurred signal, producing significant errors or even threatening the stability of the whole system. Several deconvolution and inverse filtering methods exist in literature to deal with this challenge and the election of the most robust one for each case is an issue of great importance.

To conclude, the proposed method aims to be an explanation and simulation of the visual hyperacuity, a system which makes use of diffraction to enhance the final image resolution, not like conventional imaging devices, where it can be considered a limiting factor. The application of this method can generate new opportunities and novel approaches in more than one technological field as will be described in the following chapters.

Chapter 3

Visual Hyperacuity for Imaging Systems and Applications

3.1. Introduction

The resolution is an issue of great importance for most of the imaging purposes, no matter the application area. In this case, we will refer to spatial resolution as the capability to observe or define objects as small as possible or, put another way, the level of detail of an image.

The most common imaging technologies used in conventional digital cameras, such as CCD or CMOS sensors, tend to enhance the spatial resolution by means of the reduction of the pixel size—usually arranged in 2D arrays—and increasing the number of pixels per unit area. Other solutions are focused on increasing the focal length or the size of the sensor chip. Even if current digital cameras drive resolutions up to 50 megapixels or even more, these resolution improvement procedures have technological limitations as well. Taking into account the challenges imposed by hardware techniques, signal processing approaches become of great interest as a trade-off between computational load and hardware cost.

One of the most innovative techniques in this field is the super-resolution imaging. The operating principle of this method is based on the reconstruction of high-resolution images from multiple low-resolution captures. In this way, high-frequency components are reconstructed and image details are improved overcoming the limitations imposed by low-resolution imaging devices.

Despite the fact that it cannot be considered a resolution improvement method, it is worth mentioning at this point a technique used in imaging and photography to reproduce a greater dynamic range of luminosity: High Dynamic Range Imaging. The image resolution is not affected, but this method greatly improves visual perception by combining images with different exposure parameters.

In connection with leading edge technology THz imaging cannot be forgotten, considering that it has great prospects in the field of nondestructive and contact-free testing for many applications (medicine, industry, security, material evaluation, agriculture, etc.). Nevertheless, due to technological constraints, the implementation of devices with many detectors at these frequencies is highly complicated and the resolution of the whole system is compromised. In consequence, while CCD or CMOS technologies can reach resolutions of multiple megapixels, THz imaging cameras are limited to no more than a few thousands of sensors, normally requiring the use of progressive scanning techniques. The visual hyperacuity simulation method proposed in previous chapters could prove to be of great help to overcome this technology barrier by means of software-based signal processing techniques, given that this initial limitation matches with the reduced number of sensors employed by the human eye.

This chapter provides the implementation of the visual hyperacuity simulation method for imaging systems from two different approaches: a kernel-based local implementation and another one based on the Fourier Transform, operating in the whole image or at a global level. The proposed scheme and its performance have been tested by simulations with the software MATLAB. The parameters used for analyzing the obtained results are as varied as the visual inspection, image quality metrics or the spectral analysis, compared with the results that would be obtained in absence of diffraction. The tests have been implemented using multiple images for better evaluation and assessment of its performance.

3.2. Super-Resolution Imaging

The generation of high-resolution images is a relevant issue for most digital imaging applications. The image resolution defines the level of detail contained in an image, but this concept can be understood in multiple different ways, such as spectral resolution, temporal resolution, pixel resolution, spatial resolution or radiometric resolution. In this instance, we will focus on the spatial resolution, which can be understood as the pixel density in an image, measured in pixels per unit area [27]. But in short, image spatial resolution refers to the capability of the sensor to measure or observe objects as small as possible and depends mostly upon the pixel size [28]. A standard resolution test chart used to determine the spatial resolution of an imaging systems is shown in Figure 3.1.

Overall, the spatial resolution of an image is limited by the sensor of the acquisition device. Current image sensors are based on CCD and CMOS technologies, commonly arranged in a two-dimensional array of pixels to capture 2D image signals. As the spatial resolution is governed by the optical lens and the sensor array, the most straightforward way for a spatial resolution enhancement is to reduce the size of each pixel, increasing the number of pixels per unit area. However, this solution reduces considerably the amount of available light and produces shot noise that degrades the image quality, since the SNR of the system is lowered [87]. Current image sensor technology has almost reached this existing limitation to reduce the pixel size. Other approaches for spatial resolution improvements are oriented towards increasing the focal length or the size of the sensor chip. In return, a longer focal length will result in greater size

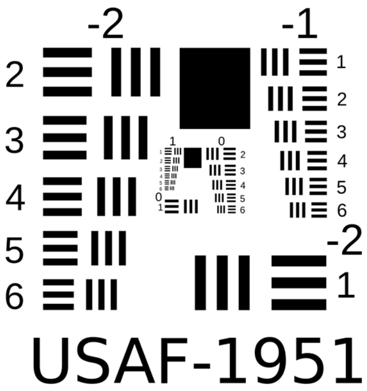

Figure 3.1. The 1951 USAF resolution test chart, set by US Air Force in 1951.

imaging devices, while a larger chip size will produce an increase in capacitance. This latter option slows down the charge transfer rate, which makes this approach deficient. On top of that, the optical system of any imaging device also limits the image details (high frequency spectral components) due to blur and aberration effects produced by the lens, aperture diffraction or optical blurring because of motion.

In brief, the construction of imaging sensors and optical components to capture high-resolution images involves a high economic cost and it is not practical in multiple real applications. Considering the difficulties of resolution enhancement via hardware techniques, signal processing methods become of great importance when high-resolution images are required, to trade-off computational load with the hardware cost. These methods are known as image super-resolution (SR) techniques and reconstruct high-resolution (HR) images from a number of low-resolution (LR) images, improving image details (high frequency components) and overcoming the limitations or degradations introduced by low-resolution imaging devices. The underlying concept is to combine, in an intelligent manner, the non-redundant information of multiple LR frames to generate a HR image (multi-frame SR). However, there are cases where it is not possible to capture multiple LR images, and thus the reconstruction of the HR image must be implemented using the limited LR information of a single image (single-frame SR).

The acquisition of different LR images can be realized by means of sub-pixel displacements, which produce various "observations" of the real scene. These sub-pixel shifts can be generated both due to ungoverned motions between the imaging system and the observed scene or due to controlled and programed movements. Each LR frame is a decimated observation of the real scene, very similar, but containing non-redundant information (see Figure 3.2). At first glance, this SR technique seems to be closely related with the image interpolation approach, that can also be applied to increase the total image size. Nevertheless, when implementing an

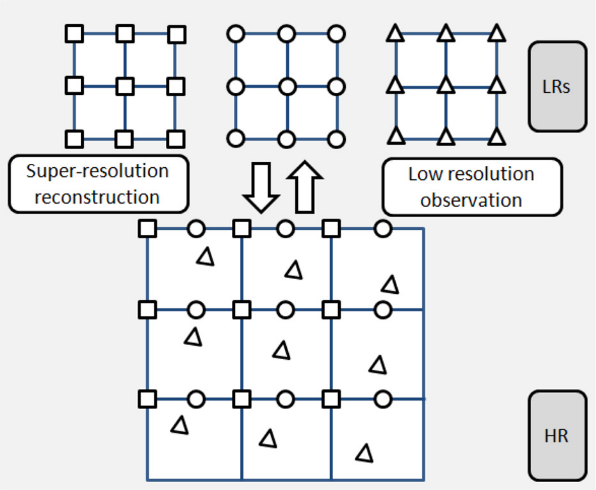

Figure 3.2. The concept of multi-frame SR: reconstruction of HR image from multiple LR observations by means of sub-pixel shifts [27].

interpolation process, no new or additional information is generated and the quality of the reconstructed image is significantly limited, as the frequency components lost in the image capturing (sampling) process cannot be recovered.

SR methods are widely used in a variety of areas and applications:

- Video standard conversion and information enhancement [88].
- Surveillance video applications: traffic surveillance, security monitoring [89].
- Earth-observation and remote sensing [90].
- Astronomical observation [91].
- Radar systems [92], [93].
- Medical imaging and diagnosis [94].
- Biometric information identification [95], [96].

3.2.1. The Observation Model

The digital system used for image acquisition presents hardware limitations which produce different degradations. Just to mention some of them, the entrance aperture causes optical blur or diffraction modeled by the PSF, the exposure time generates motion blur, the finite sensor size leads to sensor blur, the sampling produces aliasing effects which limits the spatial resolution of the captured image, the presence of noise, etc. These degradations are intended to be incorporated or modeled in different SR techniques. In general, it is usually supposed that degradations affecting the image acquisition process are warping, blurring, down-sampling and noise [27], [28], [87].

The observation model defines the relation of the HR image with LR frames (see Figure 3.3). The input of the system is the real scene, a continuous signal, which is sampled beyond the Nyquist rate to avoid aliasing[1], generating the desired HR digital image. The motion between the camera and the captured scene is modeled as a warping (translation, rotation), generating

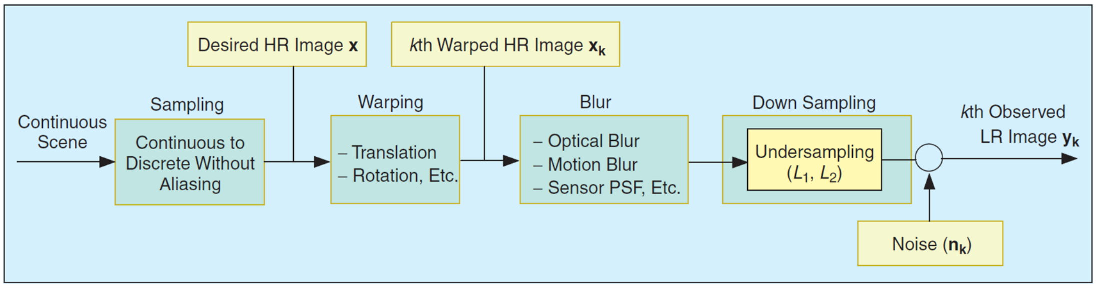

Figure 3.3. Diagram of the observation model relating HR image with LR frames [87].

---

[1] In fact, the continuous real scene has an infinite bandwidth and, therefore, it is not possible to avoid aliasing when sampling it.

multiple LR frames of the scene. The imaging device introduces different blurring effects (optical, motion, PSF) prior to down-sampling at the image sensor (pixels). Additionally, the down-sampled images are affected by the sensor noise and color filtering noise. The result is a determined number of LR frames: blurred, decimated and noisy versions of the real scene.

The observation model is mathematically expresed by:

$$\boldsymbol{y_k} = D_k H_k M_k \boldsymbol{x} + n_k, \qquad k = 1,2,\ldots,K \tag{3.1}$$

where x is the reconstructed HR image (i.e., the digital image sampled from the continuous scene) and y_k is the k-th LR observation from the camera. D_k represents the down-sampling matrix, H_k is the blurring operator, M_k is defined as the warp matrix simulating the motion information (rotation, translation) and n_k indicates additive noise. The whole observation model represented by means of images is shown in Figure 3.4.

The observation model for single-frame SR is obtained when K=1. If D_k and M_k are omitted, it becomes in a model for image restoration, just dealing with problems related to noise, blurring or the absence of information, as shown in the following equation:

$$\boldsymbol{y_k} = H_k \boldsymbol{x} + n_k\,. \tag{3.2}$$

The model described in this section does not cover all the possible situations, since other complex factors could be included to better approximate real cases, such as different types of noise, dimensional complexity or domain transformation, for example.

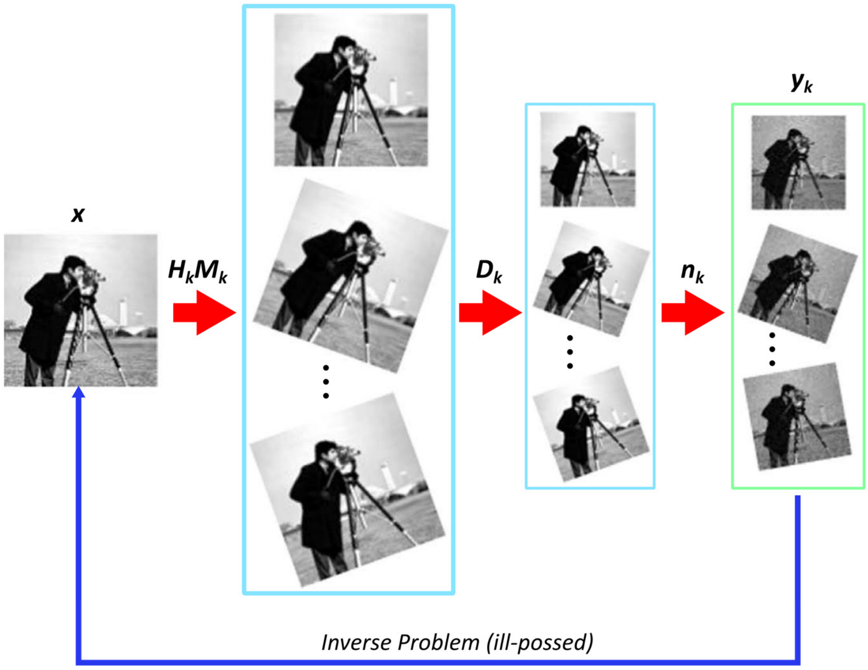

Figure 3.4. The SR imaging model.

3.2.2. SR Image Reconstruction Methods

Based on the observation model described in the previous section, the main objective is to reconstruct the HR image from a set of warped, blurred, noisy and down-sampled captured LR frames. Nevertheless, the SR image reconstruction becomes an ill-posed problem because of an insufficient number of LR frames and ill-conditioned blur operators. Therefore, the model in equation 3.1 is ill-conditioned, and the SR approach can be considered an ill-posed inverse problem. In this section, just a few conventional SR reconstruction methods will be described, even though numerous approaches exist in literature.

- ***Nonuniform Interpolation Method***

The nonuniform interpolation approach is one of the most intuitive SR techniques and it consists of three main stages:

1. Estimation of the relative motion (registration).
2. Nonuniform interpolation.
3. Deblurring and noise removal (inverse problem).

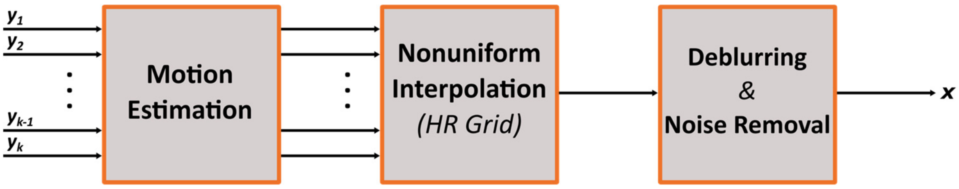

Figure 3.5. The main stages of the SR nonuniform interpolation method.

Figure 3.6 shows the process graphically: using the estimation of the relative motion information between LR images, the HR image is formed, but on nonuniformly spaced sampling points. The next step consists of producing uniformly spaced sampling points by means of a direct or iterative reconstruction process. Finally, a restoration problem is addressed to remove both blurring and noise. The inverse problem can be faced by applying any deconvolution method existing in literature, provided that noise is considered.

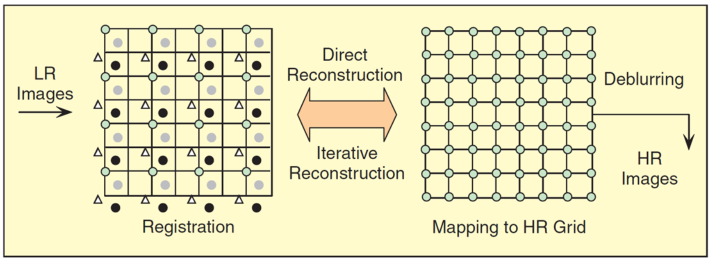

Figure 3.6. Graphical representation of the SR nonuniform interpolation method [87].

One of the great assets of this method is that it takes relatively low computational cost, making it suitable for real time applications. Nevertheless, it also presents drawbacks: the method can only be applied when the blur and the noise characteristics are constant for all LR frames. Additionally, the reconstruction algorithm is not assured, since errors produced in the interpolation stage are ignored.

- ***SR in the Frequency Domain***

The frequency domain method takes advantage of the aliasing existing in each LR frames to reconstruct the HR image [87]. The HR image is related with the LR images by a frequency domain formulation based on the shift an aliasing properties of the continuous and discrete Fourier Transforms [27], following these properties:

1. The shifting property of the Fourier Transform.
2. The aliasing relationship between the continuous FT (CFT) of the original HR image and the discrete FT (DFT) of observed LR images.
3. It is assumed that the original HR image is bandlimited.

These principles allow the formulation of the system equation relating the aliased DFT coefficients of the observed LR images to a sample of the CFT of an unknown image. Figure 3.7 shows the example of two 1D LR signals sampled below the Nyquist sampling rate (aliased) decomposed into a HR signal in absence of aliasing.

This approach is computationally efficient and theoretically simple, since the relationship between LR frames and the HR image is clear in the frequency domain. However, the method is limited in the abilities to handle complicated image degradation models and the application of the spatial domain a priori knowledge for regularization is difficult.

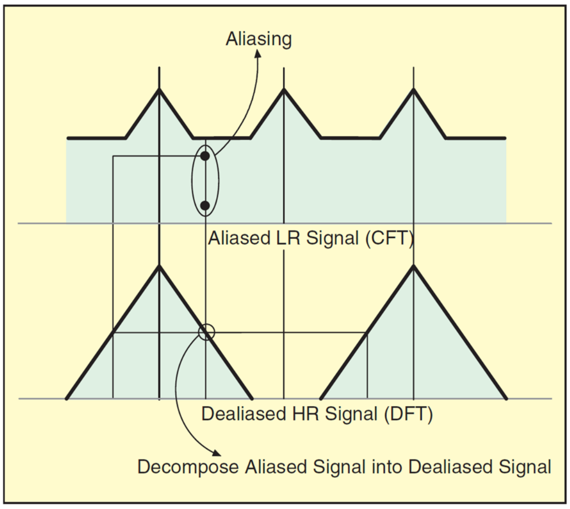

Figure 3.7. Aliasing relationship betwen LR images and HR image [87].

- ***Regularized SR Reconstruction Method***

Regularization methods are aimed at stabilizing the inversion or deconvolution of ill-posed problems. The deterministic regularized SR approach makes use of prior information of the solution to solve the observation model shown in equation 3.2, turning it into a well-posed problem. This method can be implemented by the constrained least squares method [87], formulated by choosing an *x* to minimize the Lagrangian defined by:

$$\left[\sum_{k=1}^{K}\left\|y_k - W_k x\right\|^2 + \alpha\left\|Cx\right\|^2\right] \tag{3.3}$$

where the operator C represents a high-pass filter and $\|\cdot\|$ is a l_2 -norm. The prior knowledge is represented by a smoothness constraint, accepting that most images have limited high frequency information and, therefore, minimizing the high-pass energy in the reconstructed SR image. The regularization parameter α is a Lagrange multiplier which controls the tradeoff between fidelity of data and the smoothness of the reconstruction.

When few LR images are available (the problem is undetermined) or the observed data is not accurate due to registration errors and noise, α tends to adopt large values, generating smooth solutions. Nevertheless, when the amount of noise is reduced or many LR images are available, small values of α will obtain good solutions. It seems clear that the application of a method to find the optimum value of the regularization parameter α plays a key role in the deterministic approach.

3.2.3. Challenges for Image SR

Even if SR reconstruction methods obtain high quality results in many cases, there are some challenges that must be addressed in relation with complex motion conditions, the number of used LR images or the required computational load.

In complex movement conditions, a precise motion estimation is a challenging task and an inaccurate motion registration affects considerably the performance of the SR algorithm. There exist multiple solutions to face this problem, such as the incorporation of advanced registration strategies, robust fidelity models, joint parameter estimation or methods without explicit motion estimation.

The main objective of SR is to reconstruct HR details combining the information obtained from multiple LR images. Nevertheless, in some real cases, the acquisition of a sufficient number of LR frames is difficult, being complicated to recover fine details. The performance of the reconstruction-based algorithms is deteriorated quickly when the magnification factor is large. At this point, the study of single-frame SR methods is gaining relevance in the scientific field. However, SR methods using a single image must not be confused with image interpolation and reconstruction techniques, which use little extra information and they do not reconstruct high frequency information.

Lastly, the use of SR approaches on large datasets, such as big data, generates considerable computational load. Therefore, it is crucial to develop effective and efficient methods to accelerate strategies for big data processing and satisfy the demands of the latest industrial applications. Although multiple optimizations have been already proposed in this direction, their efficiency is still far away from satisfying the exigencies of real-time applications.

The visual hyperacuity simulation method proposed in the previous chapter could deal with most of these challenges: multiple LR images are not required (a single LR frame would be enough), the blur introduced by motion or other effects is used as a benefit for super-resolution—far from being a limiting factor—and the simplicity and robustness of the whole system would suppose a considerable reduction in the computational load.

3.3. High Dynamic Range Imaging

A current method in imaging technologies and applications is the High Dynamic Range Imaging (HDRI), which aims to offer a new approach of representing colors in digital images and video. The visible range of colors of the HVS is much larger than the one obtained by conventional digital cameras and displays. HDRI technologies face this problem capturing and manipulating all colors and luminance levels visible to the human eye [97]. Some authors [98], define the HDRI as the capture, storage, manipulation, transmission and display of images that more accurately represent the wide range of real-world lighting levels. This method greatly improves the overall quality of visual content in digital images, obtaining much more realistic and attractive results.

Even if HDR images can be acquired using special image sensors (e.g., oversampled binary image sensors), the simplest way of capturing HDR images is based on merging multiple low dynamic range (LDR) images. This method involves taking multiple images, but using different exposure parameters: a different luminance range is captured in each image and, later on, these images are combined into a single HDR image by weighted averaging of pixel values across the exposures. The resulting HDR image merged from these LDR images spans the full range of luminance in the scene (see Figure 3.8).

In theory, multi exposure methods permit the capture of scenes with arbitrary dynamic ranges, provided that an adequate number of exposures per frame are merged. HDRI cannot be considered as a super-resolution method because no resolution enhancement is generated as such. However, it can be said that this technique exploits the full resolution and capture possibilities of a digital camera, producing a marked improvement in the image quality perceived by a human observer and being possible to distinguish small details that cannot be discriminated in absence of HDRI methods (see Figure 3.9). This technique is available in many consumer products (mobile phones, digital cameras), but it is also being used for scientific purposes, such as scientific imaging applications [16], electrochemical sensors [17] or even astronomical applications [99].

Althoug HDRI cannot be considered an image resolution enhancenment technique, the use of this method in combination with both SR techniques or the proposed visual hyperacuity simulation method could provide positive and interesting results, considering that the color perception is clearly improved.

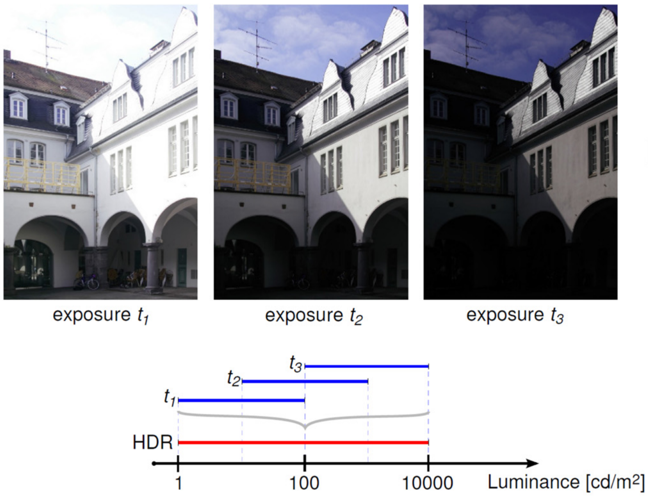

Figure 3.8. Consecutive exposures captured at subsequent time steps (t_1, t_2 and t_3) and the resultant HDR image [97].

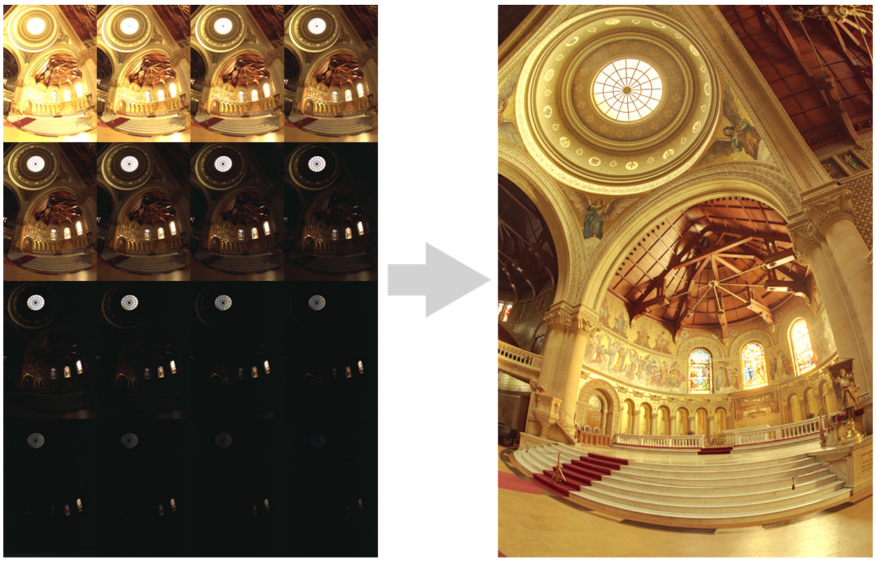

Figure 3.9. LDR image exposure sequence (left) and HDR image (right), showing small details.

Source: Open Source Computer Vision.

3.4. Terahertz Imaging

In physics, the term terahertz radiation—also known as submillimeter radiation—is applied to electromagnetic radiation with frequencies between the lower edge of the microwave band (300 GHz or 0.3 THz) and the high frequency upper edge of near-infrared light (3 THz). When talking in terms of wavelength, this frequency band ranges from 0.1 mm (infrared) to 1 mm (microwave).

It is likewise well known that there has been a lack of technology—mostly sources and detectors of THz electromagnetic radiation—between 0.3 and 30 THz, called the terahertz gap, produced due to different technological difficulties. On one side, transistor based electronic technologies are limited to about 300 GHz, even if they result extremely inefficient above the practical limit of 50 GHz. On the other hand, optical frequency semiconductor lasers can hardly generate wavelengths down to 10 µm (about 30 THz) [100]. The existence of this gap lies on the fact that no current semiconductor technology can efficiently convert electrical power into electromagnetic radiation in the THz range and inversely.

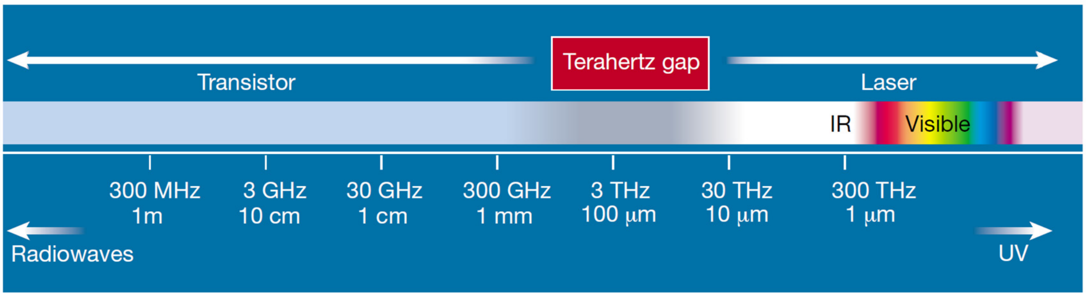

Figure 3.10. The therahertz gap lying between 300 GHz and 30 THz [100].

3.4.1. Applications of Terahertz Systems

The scientific research work over the latest years and the advances in the development of THz systems combined with the appearance of the first related commercial products (efficient emitters and detectors), has been conductive to the emergence of multiple industries and applications. THz spectroscopy, and more concretely THz imaging, holds large potential in the field of nondestructive, contact-free testing [101], [102].

- ***Pharmaceutical Industry***

THz imaging and spectroscopy technology is used to control the quality and production process of pharmaceutical products: determine the heterogeneity and integrity of pharmaceutical cores and coatings, tablet coating thickness in-line control or the analysis of the crystalline structure of drugs are just a few examples.

- ***Medical Diagnosis***

Terahertz photons are not energetic enough to break chemical bonds and ionize molecules or atoms, so they are harmless for living organisms (not as UV or X-rays). THz imaging has created multiple opportunities for medicine, thanks to the penetrating capability of THz waves, making possible to visualize internal information about physical objects. The strong water absorptions in the THz region of the electromagnetic spectrum allows the investigation of soft tissues. This technology presents many medical applications:

- Non invasive techniques for early detection of pathological conditions (cancers).
- Ex-vivo and in-vivo examination of tissues.
- Dental care.
- Preventive healthcare and blood testing.
- Diagnostics of osteoarthritis and arthritis.

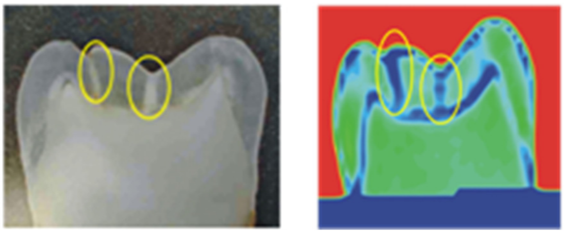

Figure 3.11. Terahertz image of a human tooth where caries are detected.

Source: TeraView Ltd.

- ***Homeland Security and Hidden Objects Identification***

THz radiation seems to be safe for screening humans and penetrates different type of clothing and other concealment and confusion materials. Therefore, this technology can be used in border and port security generating images safely, non-invasively and quickly. The application areas can be related to personnel, luggage and mail screening or detection of explosives and noxious gases among others.

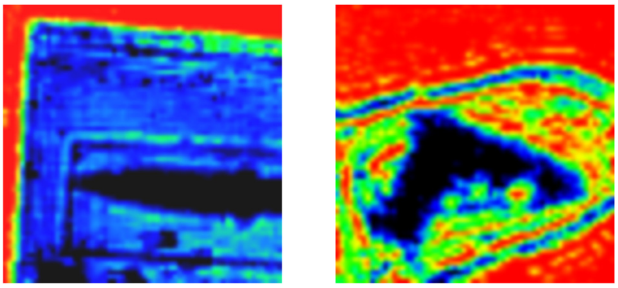

Figure 3.12. Sample sub-THz transmission images of a knife hidden in a book (left) and a gun replica hidden in a textile cover (right).

Source: TeraSense Terahertz Group.

- ***Nondestructive Evaluation of Materials***

The use of terahertz nondestructive evaluation allows the inspection of layers in multiple materials that are challenging for other technologies or characterization methods. There are many industrial applications for a wide range of materials (paper, ceramics, clothes, plastics, woods, fiber composites, etc.) that are transparent for THz waves:

  - Paints and coatings defect identification in automobile structures.
  - Non-contact stereoscopic imaging for physical art analysis.
  - Structure analysis of ceramics and composites.

- ***Material Characterization***

THz systems play a major role as instruments for contact-free inspection of plastic components, improvement of the performance and quality of solid-state properties of metamaterials and the characterization of electron carriers, understanding physical processes such as carrier transport and dynamics of semiconductors in order to further develop applications of high-speed devices.

- ***Beam Profiling Systems***

Terahertz cameras enable obtaining real time 2D cross-section intensity maps of antenna beams, being a useful technology for characterizing THz radiation sources (measure the beam intensity profile and the far-field radiation pattern) and aligning quasi-optical THz systems.

- ***Terahertz Inspection of Agricultural Products***

Terahertz imaging technology for nondestructive testing and noninvasive inspection appear to take the lead in popularity in the agricultural sector and the industry of product processing. With the aid of THz imaging devices, it is possible to detect under the shell the presence of harmful fungus and infections affecting peanuts, corn, nuts, other grain-crops and oil-plants (observe Figure 3.13). In a similar way, THz cameras can also be used to detect the seed

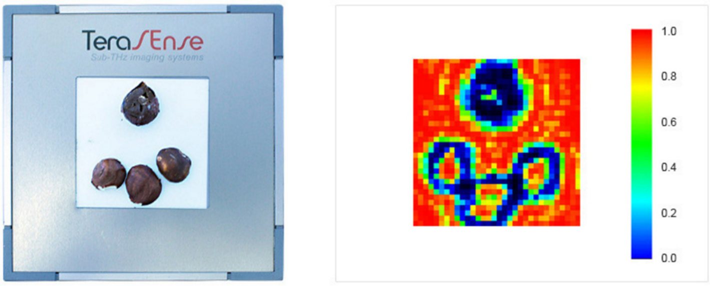

Figure 3.13. Picture of four hazelnuts (right) and THz image of the same hazelnuts at 100 GHz (right). The upper nut is infected with fungus.

Source: TeraSense Terahertz Group.

availability and determine the seed structure inside a plant or for acidity estimation of sunflower seeds. Another problem linked to agricultural processing is the separation of stones, sticks, mud clots and other contaminants from the crops, where visual inspection equipment fails due to the inherently low color contrast. The different absorption that contaminants have in the THz frequency range makes them clearly discernible when capturing THz images.

Another possible application of THz imaging for agriculture relates to monitoring the presence of water in plants and leaves. A constant control of water status in plants or any type of crops is a matter of great importance to improve aspects related to irrigation scheduling, alleviate extreme climate effects and, consequently, enhance as much as possible the quality of final products [103], [104].

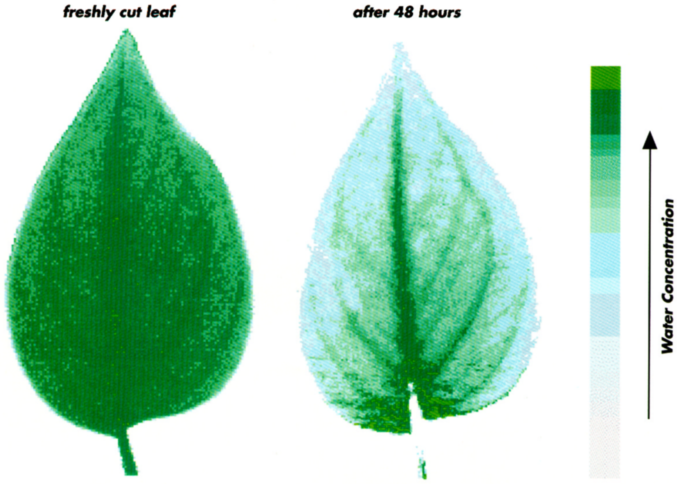

Figure 3.14. THz image of a fresh leaf (left) and the same leaf after 48 h (right), where it can be observed that water has clearly evaporated, except from the stems of the leaf [101].

3.4.2. THz Imaging Technological Difficulties

Even if THz imaging provides cutting-edge in multiple applications, this technology also presents some difficulties that must be faced. There exists a technical challenge in connection with signal generation, since THz frequencies are so high that conventional oscillators cannot work effectively and too low for the optical photon emitters to work in. In order to close this gap, THz waves are usually generated by either one of these methods and frequency multipliers or dividers [105].

One of central issues in the THz science and technology research is the resolution of imaging systems. Due to the long wavelength ($\lambda_{1\ THz}$=300 µm) used in THz applications, the spatial resolution is constrained by the limited spot size and the resolution is generally in the scale of millimeter when working as a diffraction-limited system [106], [107].

Additionally, there exists difficulties to fabricate and implement devices with many detectors at terahertz frequencies and this technological constraint limits the resolution possibilities of the whole system. As previously explained, neither optical nor microwave technology provide effective tools for developing practical solutions at the low THz frequency band. Common devices working in these frequencies require the use of complex detectors equipped with heterodyne receivers to perform conversions to work in an intermediate frequency that current technology can handle [108]. Such drawbacks considerably limit the number of detectors that can be implemented in an array. Therefore, while optical imaging devices based on CCD or CMOS technologies use sensor arrays of multiple megapixels, THz imaging cameras are limited to some hundreds or a few thousand detectors (see Figure 3.15).

The manner in which THz technology has overcome these challenges is through progressive scanning techniques, such as scanning mirror systems [109] or progressive mechanical scanning techniques where both the analyzed objects or the imaging devices can be moved [110], as can be observed in Figure 3.16.

Figure 3.15. Terahertz imaging camera of 4096 pixels (64×64 array) and linear camera of 1024 pixels (256×4 array).

Source: TeraSense Terahertz Group.

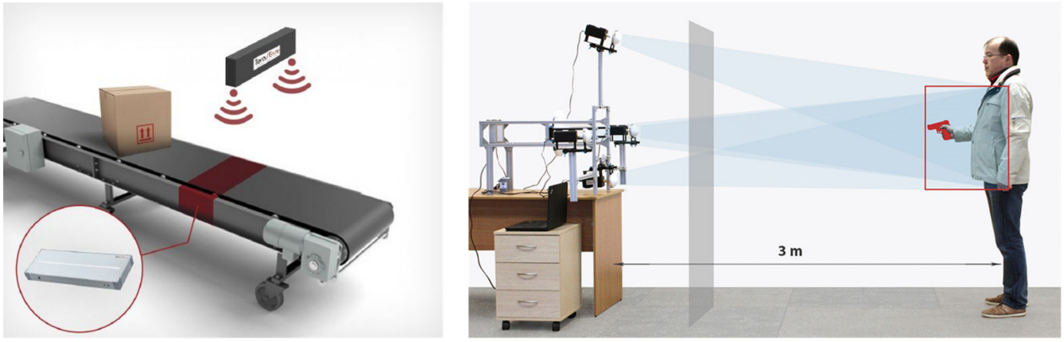

Figure 3.16. Layout for linear THz imaging system installation on a conveyor (left) and THz security body scanner (right).

Source: TeraSense Terahertz Group.

3.4.3. Visual Hyperacuity for Terahertz Imaging

As already stated, one of the main constraints in THz imaging systems is the low number of available detectors to capture images. This initial limitation coincides with the reduced number of sensors that the human eye employs for central sharp vision. Therefore, the visual hyperacuity simulation method presented in Chapter 2 could be very useful in overcoming this hardware resolution constraint by means of software-based signal processing techniques. The low-resolution images generated by current THz imaging devices usually allows to detect the presence of foreign objects but, in many cases, it is difficult to determine what they really are. The resolution improvement achieved with the proposed method could better define the shape of visualized objects, being an important advance for many THz applications.

Moreover, the spatial diversity generated by means of the introduction of a controlled diffraction improves the SNR of the imaging device, obtaining a higher sensitivity. This feature offers multiple advantages: first of all, the working distance can be increased significantly. Besides, it would be possible to reduce the radiation power or even dispense with the use of THz sources. The radiations produced by THz body scanners systems are supposed to be non-invasive and non-ionizing, but this subject matter is always controversial.

Finally, replacing the mechanical scanning systems (conveyor belts, mirrors, etc.) with software-based resolution enhancement techniques, such as the proposed visual hyperacuity simulation method, would lead to a significant reduction in the time required for analyzing each object or person. This technological advance would avoid placing objects in conveyor belts or could allow people to get through security checkpoints in airports and borders without the need to stop while the security body scanner performs the scanning process.

3.5. Kernel-Based Hyperacuity Simulation Method. A Local Approach

As mentioned earlier, human eye could be profiting from the spatial diversity obtained thanks to different sources of distortion, mainly diffraction. Therefore, the introduction of a known diffraction blur at the entrance of the system (understanding it as a low pass filtering) has a key role in the proposed method. This first step relaxes signal sampling frequency constraints, enabling the use of a reduced number of sensors for a subsequent image data capture. Afterwards, the low-resolution blurry image is interpolated increasing the total number of data points. The softening process performed in advance makes possible a more accurate interpolation, due to slow signal variations. Eventually, an inverse filtering or deconvolution process is applied to remove the blur introduced in the first stage, and thus recovering a sharp image with considerably increased resolution in relation to the captured one at the entrance of the system. Due to the ill-posedness of the inverse problem, stability of the system at this final step comes to be critical. The whole system is shown in Figure 3.17.

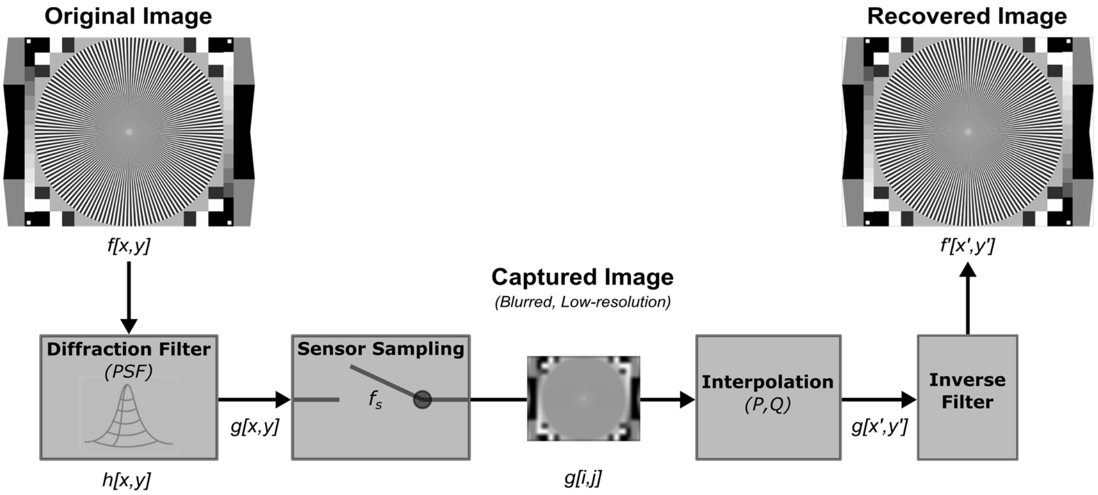

Figure 3.17. Block diagram of the hyperacuity simulation system.

3.5.1. Pre-Processing: Diffraction and Image Sensing

The distortion introduced by the optical system can be simulated in 1D by a discrete FIR filter:

$$g_n = b_0 f_n + b_1 f_{n-1} + \ldots + b_N f_{n-N} = \sum_{k=0}^{N} b_k f_{n-k} \,, \tag{3.4}$$

where f_n is the input signal, g_n the output (distorted) signal, N the filter order and b_k are the coefficients of the direct form FIR filter. Thus, equation 3.5 shows the Z-transform of the transfer function and the corresponding diagram is displayed in Figure 3.18.

$$H(z) = \frac{G(z)}{F(z)} = \frac{b_0 + b_1 z^{-1} + \ldots + b_N z^{-N}}{1} \tag{3.5}$$

It is possible to perform 2D processing, just following the elements in two dimensions (rows and columns) and the general expression for the discrete 2D FIR filter is defined by

$$g_{m,n} = \sum_{j=0}^{M} \sum_{k=0}^{N} b_{j,k} f_{m-j,n-k} \,. \tag{3.6}$$

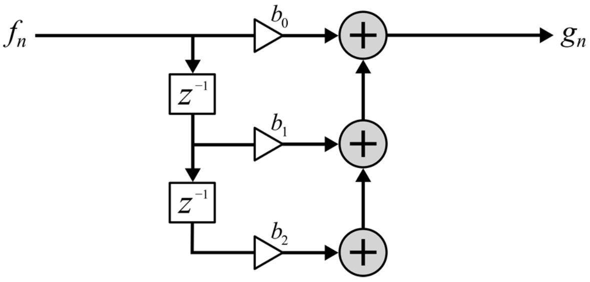

Figure 3.18. Direct form 1D discrete FIR filter diagram.

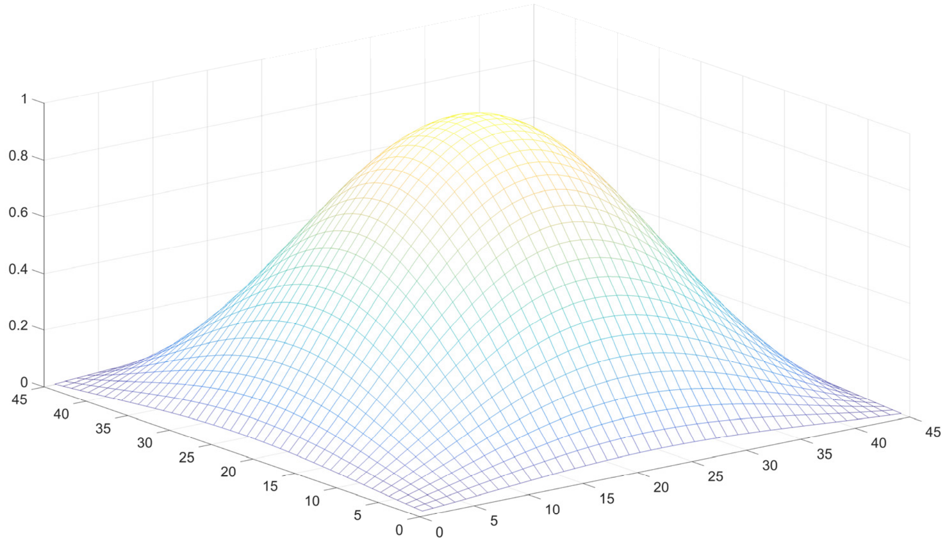

Figure 3.19. System input 2D Point Spread Function (45×45 pixels).

When observing equation 3.6, it is possible to notice that the 2D FIR filter approximates a 2D discrete convolution of the incoming image and the kernel which simulates the diffraction introduced by the optical system:

$$g[x,y] = f[x,y] * h[x,y] \tag{3.7}$$

where h represents the PSF, f the original image and g the filtered output image. The PSF is essentially a *sinc*^{2} type radial function of 45×45 pixels (observe Figure 3.19), to which some modifications have been applied. Firstly, side lobes have been removed remaining only the central one, to avoid null coefficients. Furthermore, the maximum has been slightly shifted (less than one sample) breaking the symmetry of the PSF. These settings are quite relevant to the stability of the system.

To simulate the real scene observed by the imaging system—ideally an infinite resolution continuous image—, it has been used a high-resolution test image of 567×755 pixels (see Figure 3.20). It is worth pointing out that it is not possible to go beyond this initial resolution, whichever image restoration method is used. This original test image has been filtered using the PSF shown in Figure 3.19 by means of a 2D discrete convolution as the one described in equation 3.7.

Once the diffraction introduced by the optical system is simulated with the low-pass filtering process, the outcoming image is subsampled by means of a decimation process (a factor of 2 in each dimension), reducing the image size to 284×378 pixels. This subsampling intends to reproduce the reduced number of sensors used to capture a real image, supposed to be continuous or a high-resolution image (as the one used initially). At this point finishes pre-processing, obtaining an image considered to be the system input: a low-resolution image with slow variations, due to the controlled distortion introduced by the PSF (see Figure 3.21).

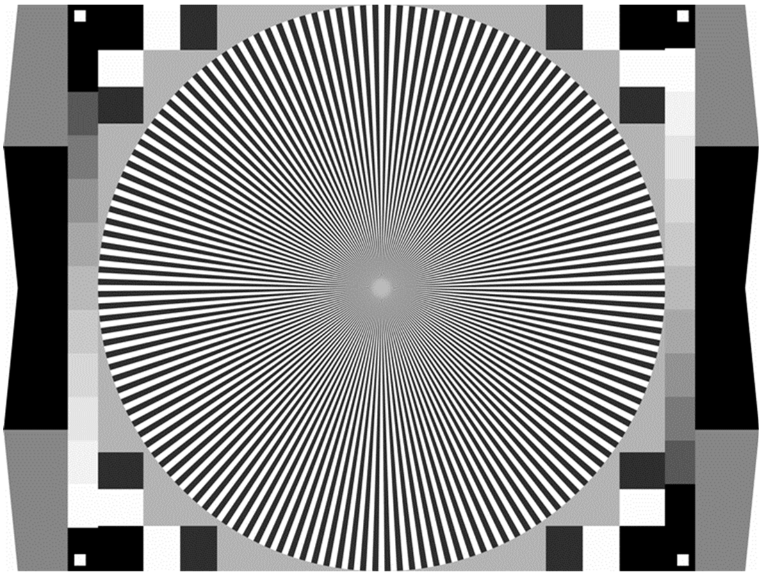

Figure 3.20. High-resolution original test image (567×755 pixels).

Figure 3.21. Low-resolution blurred captured image (284×378 pixels).

3.5.2. Post-Processing: Interpolation and Inverse Filtering

The previously blurred and sensed image is interpolated by a factor of 2 in each dimension (vertical and horizontal), by means of a 2D cubic spline interpolation method. The output image is still blurred, but the image size has been increased to 567×755 pixels. It is worth to mention that the LPF introduced in advance makes possible a more precise interpolation, since low variation transitions reduce sampling frequency constraints and enable more accurate estimation of new data points.

The last step consists in implementing an inverse filtering process, to obtain a resolution-enhanced and sharp image, recovering high frequency spectral components. The inverse problem comes to be ill-posed and thus the system becomes highly unstable and sensitive to small errors generated on account of interpolation. The above-mentioned modifications made to the PSF are focused to minimize the effects produced by this instability, obtaining better results when the inverse filtering is performed.

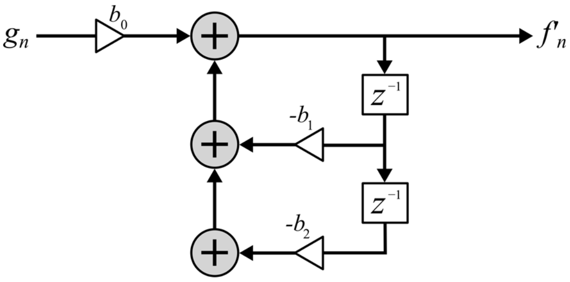

Figure 3.22. Inverse form 1D discrete IIR filter diagram.

The inverse process would mean that *H(z)* should be inverted, i.e. denominator and numerator swapped: a_k and b_k coefficients of the direct FIR filter must be exchanged. We may as well see how this inversion makes the former expression (equation 3.8) become an all poles IIR filter, which corresponding diagram can be seen in Figure 3.22. Note that now the entrance g_n would refer to the blurred and interpolated image and f'_n to the recovered estimation.

$$H_{inv}(z)=\frac{F(z)}{G(z)}=\frac{1}{b_0+b_1z^{-1}+\ldots+b_Nz^{-N}}=\frac{\frac{1}{b_0}}{1+\frac{b_1}{b_0}z^{-1}+\ldots+\frac{b_N}{b_0}z^{-N}} \tag{3.8}$$

Now, the 1D inverse IIR filter difference equations can be written as follows:

$$f'_n=\frac{1}{b_0}\left(g_n-\sum_{k=1}^{N}b_kf'_{n-k}\right). \tag{3.9}$$

2D processing can be performed by following the elements in two dimensions by rows and columns and the discrete 2D IIR filter's difference equations are expressed by:

$$f'_{m,n}=\frac{1}{b_{0,0}}\left(g_{m,n}-\sum_{j=1}^{M}\sum_{k=1}^{N}b_{j,k}f'_{mm-j,n-k}\right). \tag{3.10}$$

Since the 2D IIR filter comes to be recursive, each system output $f'_{m,n}$ depends on the previous output samples defined by an M×N mask formed by filter $b_{j,k}$ coefficients (see Figure 3.23). An important observation would be that with this technique just the filter coefficients and an equal M×N number of data elements are needed to compute each output sample $f'_{m,n}$ keeping the problem localized (in this case, a 45×45 coefficient matrix), rather than using a large amount of elements. This is why this method can be defined as a local approach.

The outcome of applying the inverse filter to the blurred and interpolated image is displayed in Figure 3.24. Edges appear now significantly sharper, being possible to define and distinguish shapes that could not be appreciated beforehand. In addition, high frequency information has been recovered mainly at the central part of the output image: abrupt transitions could not be noticed in the incoming image (Figure 3.21). Finally, the image has now a resolution of 567×755

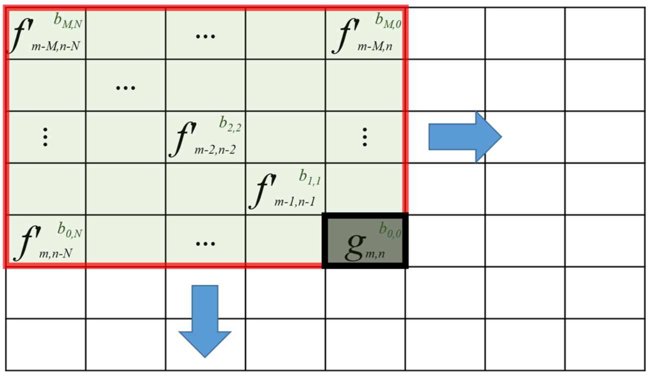

Figure 3.23. 2D IIR filter performing by rows and columns, positioned to calculate the output sample $f'_{m,n}$.

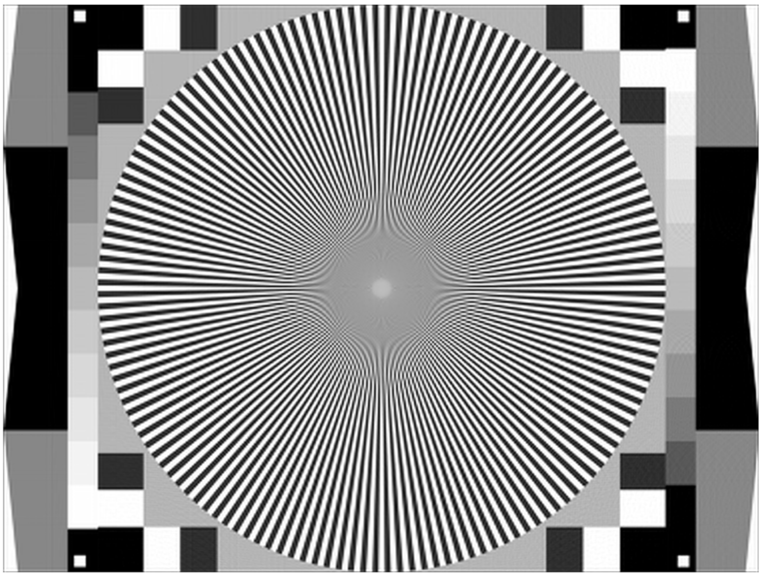

Figure 3.24. High-resolution recovered output image (567×755 pixels).

pixels, which means that it has been increased by a factor of 4 when compared to the initial image or equivalent sensor size (284×378 pixels).

3.5.3. Analysis of the Results

The outcomes obtained by means of this method are worth analyzing carefully if the resolution improvement is to be observed. One way to evaluate this enhancement is to compare the recovered image with an image that would supposedly be a distortion-free image or the one captured by a diffraction-limited system with the same sensor size of 284×378 pixels (see Figure 3.25). At first glance, it is difficult to appreciate a real improvement, just some high frequencies at the central part of the image seem to be better displayed. Figure 3.26 shows a digital zoom for better comparison: considering the high-resolution original test image (a) as a reference, it can be appreciated how the image recovered using the method (b) reconstructs shapes and edges accurately, while the diffraction-free image (c) hardly defines edges due to a pixelating effect. Note that initially both images had the same size of 284×378 pixels before applying post-processing techniques of the visual hyperacuity simulation method.

The whole method has been applied to different images, generating more results to provide better observation and analysis (Figure 3.27). Observe how in the case of the cameraman facial features and small details of the camera are accurately reconstructed. However, in the image captured simulating a diffraction-limited system they are hardly recognizable. Similarly, when

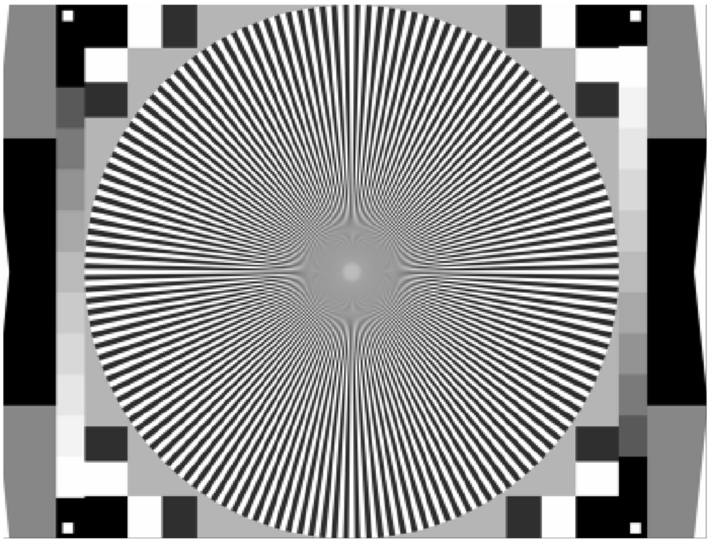

Figure 3.25. Distortion-free image (284×378 pixels), captured by a diffraction-limited system.

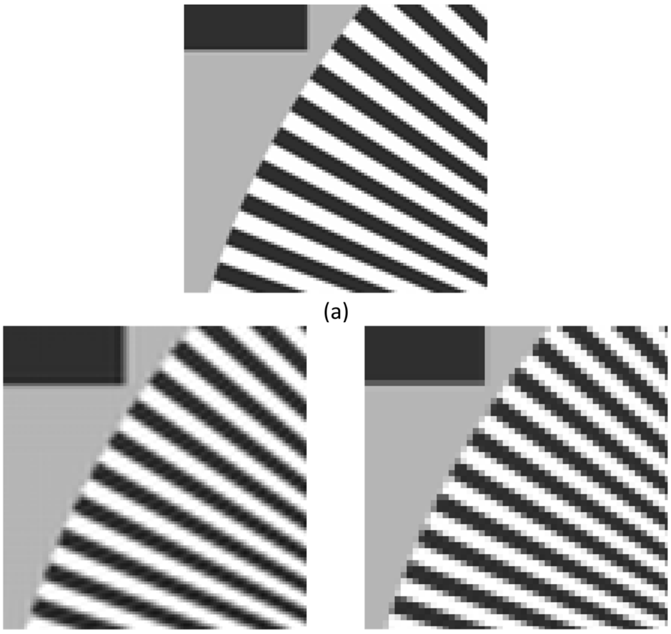

(a)

(b)

(c)

Figure 3.26. Image detail of: (a) original test image of 567×755 pixels; (b) high-resolution recovered image of 567×755 pixels; (c) distortion-free image of 284×378 pixels.

analyzing the image of the airplane, numbers, letters and the shape of the star are barely recognized when the hyperacuity simulation method is not implemented.

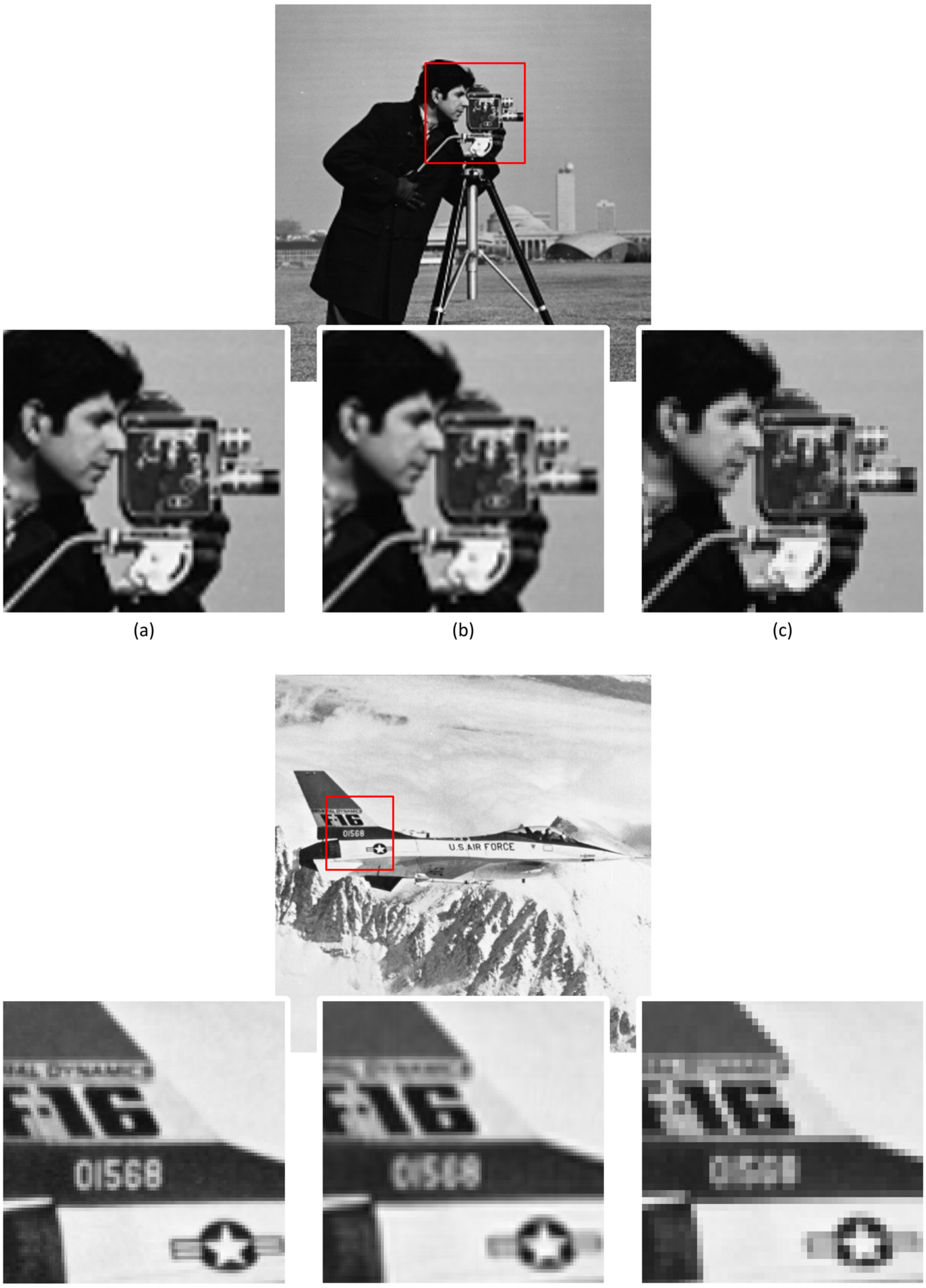

Figure 3.27. Original test images and details of: (a) original test image of 511×511 pixels; (b) high-resolution recovered image of 511×511 pixels; (c) distortion-free image of 256×256 pixels.

Image or resolution enhancement in digital images can be subjective and it is interesting to establish empirical measures to determine the effect of the visual hyperacuity simulation method on image quality. Therefore, with the aim of obtaining a more objective, accurate and quantifiable quality metric working at pixel level, it has been computed Peak Signal-to-Noise Ratio (PSNR). This parameter calculates the ratio between the maximum possible value (power) of a signal (or image) and the power of distorting noise that affects the quality of its representation. In other words, it compares the “true” pixel values of the original test image to the pixels of the degraded image.

The PSNR is commonly expressed in terms of the logarithmic decibel scale by the following mathematical equation:

$$PSNR = 20\log_{10}\left(\frac{MAX_f}{\sqrt{MSE}}\right), \tag{3.11}$$

where the Mean Squared Error (MSE) for an image size of $M\times N$ is given by:

$$MSE = \frac{1}{MN}\sum_{m=1}^{M}\sum_{n=1}^{N}\left\|f[x,y]-g[x,y]\right\|^2 . \tag{3.12}$$

Taking the original test images (pattern, cameraman and airplane) as reference, it has been computed the PSNR for the images recovered using the proposed method and the diffraction-free ones, in which case a nearest-neighbor interpolation has been made to match the image size (the dimensions of reference and degraded images must be identical). Results are shown in Table 3.1, obtaining improvements around 4.5 dB when applying the visual hyperacuity simulation method.

Image	**Hyperacuity Simulation Method PSNR (dB)**	**Diffraction-Limited Simulation Method PSNR (dB)**	**Improvement (dB)**
Pattern	16.85	12.32	**4.53**
Cameraman	29.17	24.43	**4.74**
Airplane	26.91	22.59	**4.32**

Table 3.1. PSNR of images with the hyperacuity simulation method, diffraction-limited simulation method and the obtained improvement.

3.5.4. Comments on the Method

In view of the results, it has been demonstrated how diffraction can be helpful to improve the final image resolution, far from being a limiting factor like in most imaging devices. In this regard, the method can be understood as an explanation and simulation of visual hyperacuity.

Mention that the inverse problem is a critical process that could be solved through the use of diverse methods and here just one has been implemented. There are different factors that should be taken into account when choosing the most appropriate method to solve the inverse filtering as the nature of the diffraction effect, the presence of noise in the system, the resolution enhancement required, the type of images or the specific application. Nevertheless, keeping the problem localized as in this case reduces the stability problems since less elements are involved in the calculation of each output value. In return, the recursive approach generates a cumulative error that could be avoided using other methods.

Additionally, it can be said that the proposed system breaks the established relationship between the number of pixel sensors needed to capture an image and its final resolution, leading us to consider the opportunities and possibilities this method provides.

3.6. Fourier-Based Hyperacuity Simulation Method. A Global Approach

The main stages of the Fourier-based hyperacuity simulation method are virtually identical to the ones of the above described method. The first step of the approach consists in introducing a known diffraction blur using a PSF (low-pass filter) at the entrance of the system. The resulting blurry image is then captured with a low number of sensors, i.e., spatially subsampled: this would be the input image, the one projected over the sensors and captured by the imaging device. On the next stage the image goes through an interpolation process, increasing the total data points, thus, creating new samples. At the final stage, an inverse filter is applied to remove the blur introduced by the diffraction, which recovers a sharp and focused image, with an enhanced resolution in comparison to the one captured by the sensor.

The main difference lies in the method used both for introducing a controlled diffraction and for solving the inverse problem: in this case, the scheme is based on Fourier Transforms. The fact that the convolution in the frequency domain is an element to element product means that the original test image and the PSF must have the same size (in pixels). Therefore, the output depends on all the elements involved in the process, so it may be regarded as a global—non-localized—approach. When the size of the original image and the PSF does not match, it must be performed a zero-padding prior to calculating the DFT.

Another important variation is that the method has been applied to color images. The system does not undergo significant changes, unless the original test image is splitted into RGB components and each channel must be processed independently, before combining them at the end of the method. For better understanding, the block diagram of the complete system is depicted in Figure 3.28.

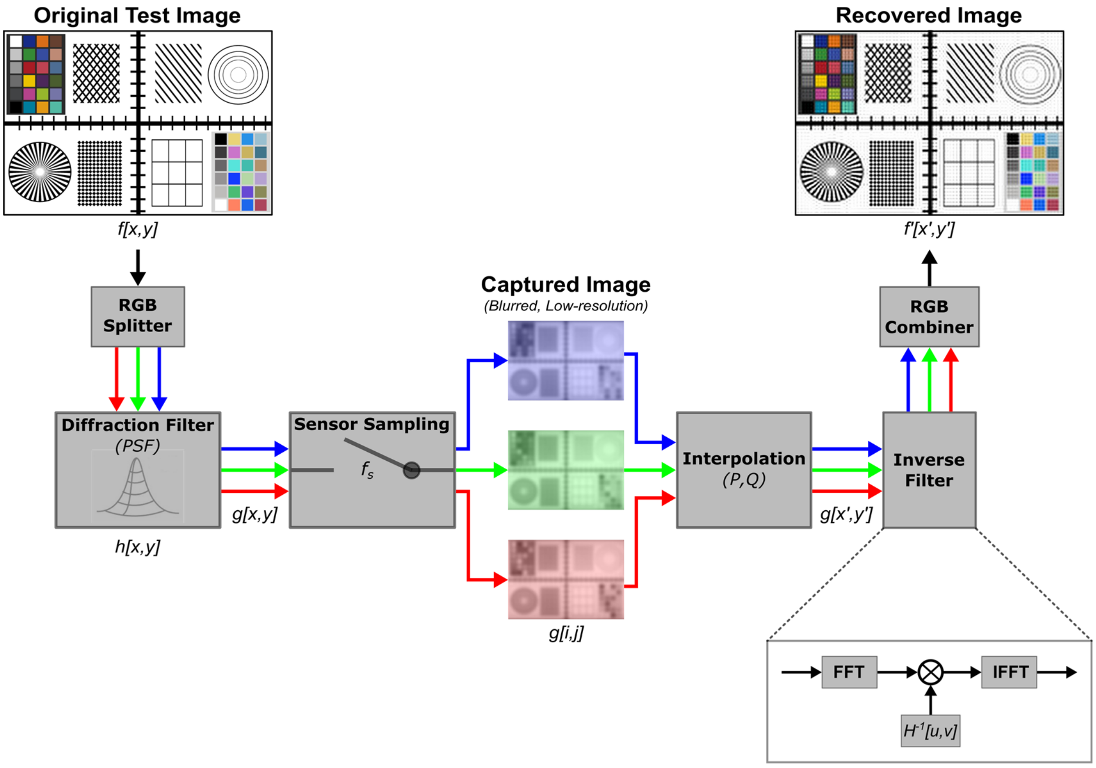

Figure 3.28. Block diagram of the visual hyperacuity simulation method for RGB images: original test image (observed real scene), captured RGB images (input images, blurred and low-resolution) and recovered image (enhanced resolution).

3.6.1. Image Capture: Diffraction and Sensing

The selected original test image is 1600×1100 pixels in size (see Figure 3.29). This image is used as a model of the real scene observed by the imaging system, and as such, it is conceived as a high-resolution image at the entrance of the optical system.

The image projected over a sensor can be modeled by a simple convolution of the real scene and the diffraction pattern or PSF produced by the optical system,

$$g[x,y] = f[x,y] * h[x,y] \tag{3.13}$$

where *f* represents the original test image, *h* is the PSF and *g* is considered as the blurry image captured by the sensor. Applying the Fourier Transform, the image acquisition process can be expressed as a simple matrix multiplication as follows:

$$G[u,v] = F[u,v] \cdot G[u,v] \, . \tag{3.14}$$

The diffraction pattern (PSF) created by a uniformly-illuminated circular aperture is an Airy Disk, which can be approximated by a $sinc^2$ type radial function of 1600×1600 pixels such as the one displayed in Figure 3.30, and its main effect is the introduction of blur in the incoming image transforming point sources into blobs. Since the size of *f* and the PSF does not match, the original

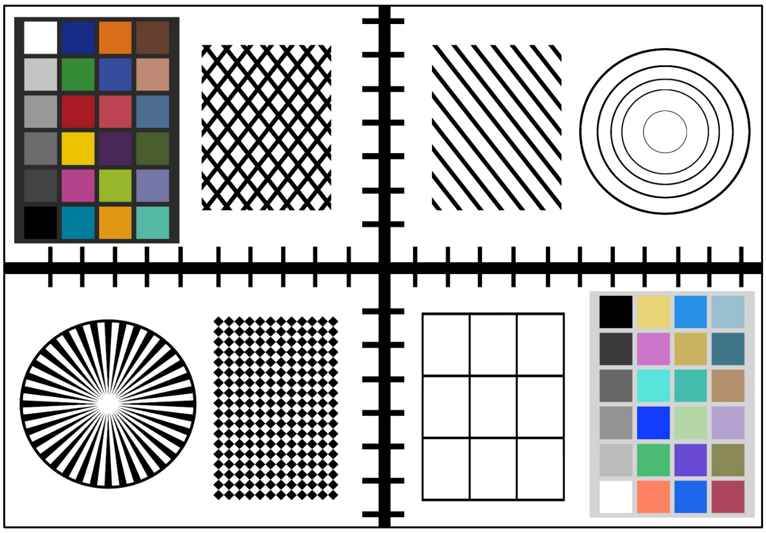

Figure 3.29. Original test image used for simulation, reproducing the high-resolution observed real scene (1600×1100 pixels).

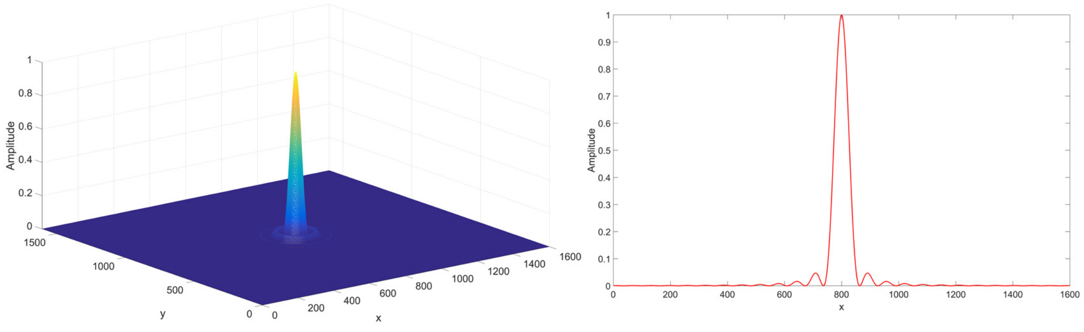

(a)

(b)

Figure 3.30. (a) MATLAB 3D plot of the *sinc*^{2} type PSF of 1600×1600 pixels. (b) Cross section of the PSF through the central plane.

test image has been zero-padded reaching a size of 1600×1600 pixels (the black edge will be removed when showing the images). This diffraction introduced by the optical system acts as a low-pass filter (LPF) when analyzing in the frequency domain.

To simulate the image capturing using a reduced number of sensors, the previously diffracted image is spatially subsampled, performing a decimation by a factor of 10 in each dimension (vertical and horizontal) and reducing data points to 160×110 pixels. It is important to note, that the LPF introduced by the PSF enables to lower the sampling frequency (i.e., use less sensors), since the signal is now limited in a narrower frequency-band. In this sense, we can understand the introduction of diffraction as an anti-aliasing filter prior to the sampling process, which attenuates considerably the high frequencies of the image. In addition, the subsampling produces spectral truncation, permanently removing some high-frequency spectral components. At this point, we obtain the image considered to be the system input, the one captured by the sensors: a low-resolution image (simulating a low number of sensors) and blurred due to the diffraction introduced by the optical system (see Figure 3.31), which renders difficult to appreciate sharp edges and shapes because of the loss of information at high frequencies.

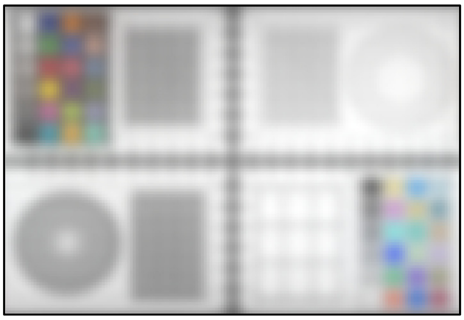

Figure 3.31. Image captured by the sensor: blurred and low-resolution (160×110 pixels).

3.6.2. Post-Processing: Interpolation and Inverse Filter

To achieve a resolution enhancement, the first step is to increase the image size, and by doing so, new data points are created between the existing samples. For this purpose, it has been implemented a 2D interpolation by a factor of 10 using the FFT method. The interpolated image is still blurred (there is no acuity or detail improvement), but the image size is increased from 160×110 to 1600×1100 pixels (observe Figure 3.32). The LPF (diffraction) introduced in advance makes possible a more accurate interpolation, since the blurred image presents low-variation and smooth transitions, and enables a more precise estimation of new image data points. As may be seen, the use of this interpolation factor returns the image to its original size. Even if the choice may appear arbitrary, the reason is that this is the maximum resolution that can be

Figure 3.32. Interpolated image: blurred and increased data points (1600×1100 pixels).

recovered due to the size and resolution of the original test image. Additionally, it provides the chance of taking it as a reference to evaluate the achieved resolution improvement.

The last stage of the visual hyperacuity simulation method is the application of an inverse filter to remove the blur introduced by the diffraction, obtaining a resolution-enhanced and sharp image. It is worth mentioning that the inverse-problem is ill-posed and thus the inverse filtering process becomes highly unstable, presenting high sensitivity against errors produced by interpolation and noise-amplification problems. However, the LPF effect of the PSF and the subsampling performed in advance, considerably attenuate or even remove some high-frequency components (the most critical in relation to stability and noise-amplification problems), making possible the use of an inverse filter in a straightforward manner. The inverse filtering is also carried out in the frequency domain, by applying the inverse filter $H^{-1}[u,v]$, to the diffracted, subsampled and subsequently interpolated image:

$$F'[u,v] = G[u,v] \cdot H^{-1}[u,v] = G[u,v] \cdot \frac{1}{H[u,v]} \,. \tag{3.15}$$

The output image obtained from implementing the inverse filter is shown in Figure 3.33. As can be appreciated, even if some high frequency information has been lost, edges appear considerably sharper being possible to recognize and resolve shapes, details, lines and abrupt color transitions that were not detectable in presence of diffraction. This resolution improvement is produced thanks to the new data points created by interpolation between sensed samples and the reconstruction of the spectral components attenuated in advance by diffraction, but it is not possible to recover the components previously truncated due to the subsampling process. Nevertheless, the most important spectral information of the image is kept in low-frequencies and this loss may not be critical when reconstructing the original image.

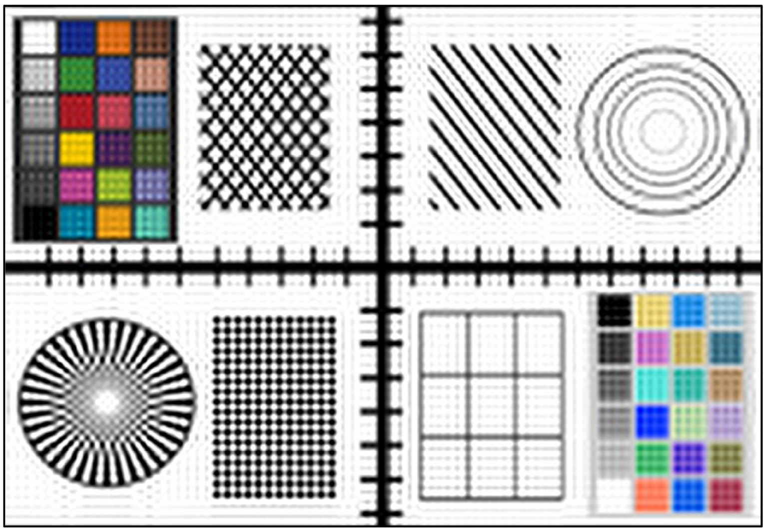

Figure 3.33. High-resolution recovered image (1600×1100 pixels), using the Fourier-based visual hyperacuity simulation method.

In addition, the image has now a size of 1600×1100 pixels, meaning that the resolution is increased by a factor of 10 in each dimension (vertical and horizontal) in comparison to the initial low-resolution image of 160×110 pixels captured by sensors, due to the creation of new data points between samples. However, it should be noticed that a slight grid effect is created in the image background because of the FFT interpolation process.

3.6.3. Analysis of the Results

Once again, the results must be analyzed rigorously to discern the resolution improvement. On this occasion as well, the resolution enhancement of the outcome is evaluated comparing the Fourier-based visual hyperacuity simulation method with an identical but diffraction-limited system, without introducing neither diffraction and therefore nor inverse filter: the image is captured with the same sensor size of 160×110 pixels and an FFT interpolation method is implemented, increasing the data points by a factor of 10 in each dimension. For a better understanding the block diagram of this scheme is depicted in Figure 3.34. The result of reproducing the method without diffraction and inverse filtering can be observed in Figure 3.35.

Figure 3.36 shows side by side the original test image (a) and the images obtained using the proposed method with diffraction (b) and without diffraction (c), for a better visual comparison. A simple visual inspection reveals that thanks to diffraction many fine details can be recovered (grid lines, reconstruction of patterns and continuous circumference lines, sharp definition of objects keeping their size) and information can as well be detected which is not feasible when diffraction is not introduced in the system. In short, the image shown in Figure 3.36 (b) captured in presence of diffraction represents in a more accurate way the original test image represented in Figure 3.36 (a) and almost no data is lost. The spreading of light over the sensor produced by diffraction creates spatial diversity and the information of a single point source is also expanded

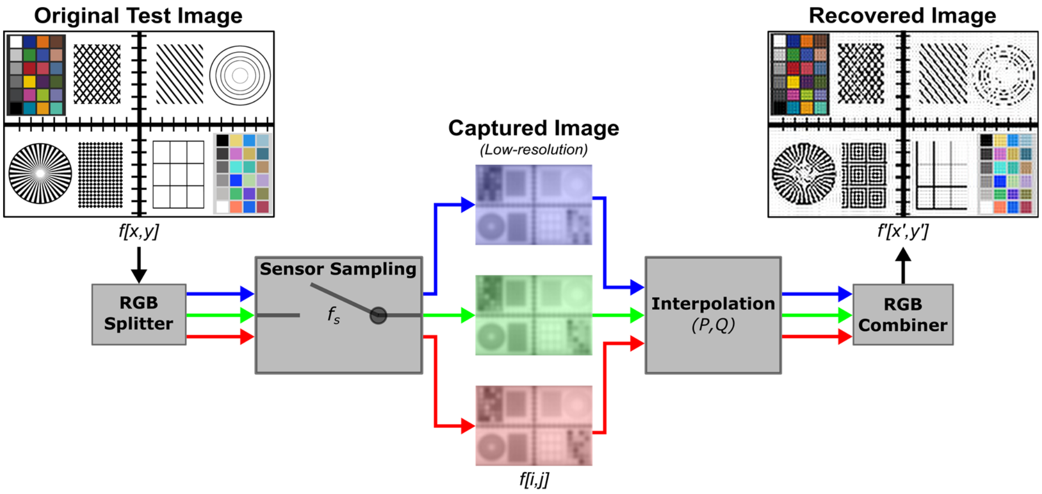

Figure 3.34. Block diagram of a diffraction-limited system simulation method: original test image (observed real scene), captured image (input image, low-resolution but diffraction-free) and recovered image (interpolated).

over a wider area, being possible to sense information using a reduced number of sensors, which would be lost in absence of diffraction. Therefore, we can recover information spatially located between sensors and represent it creating new samples: increasing the image resolution.

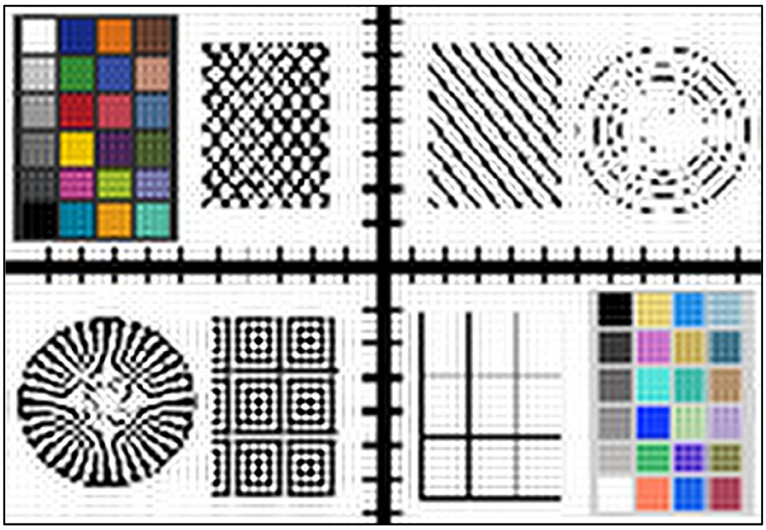

Figure 3.35. Recovered image (1600×1100 pixels) simulating a diffraction-limited system and interpolation.

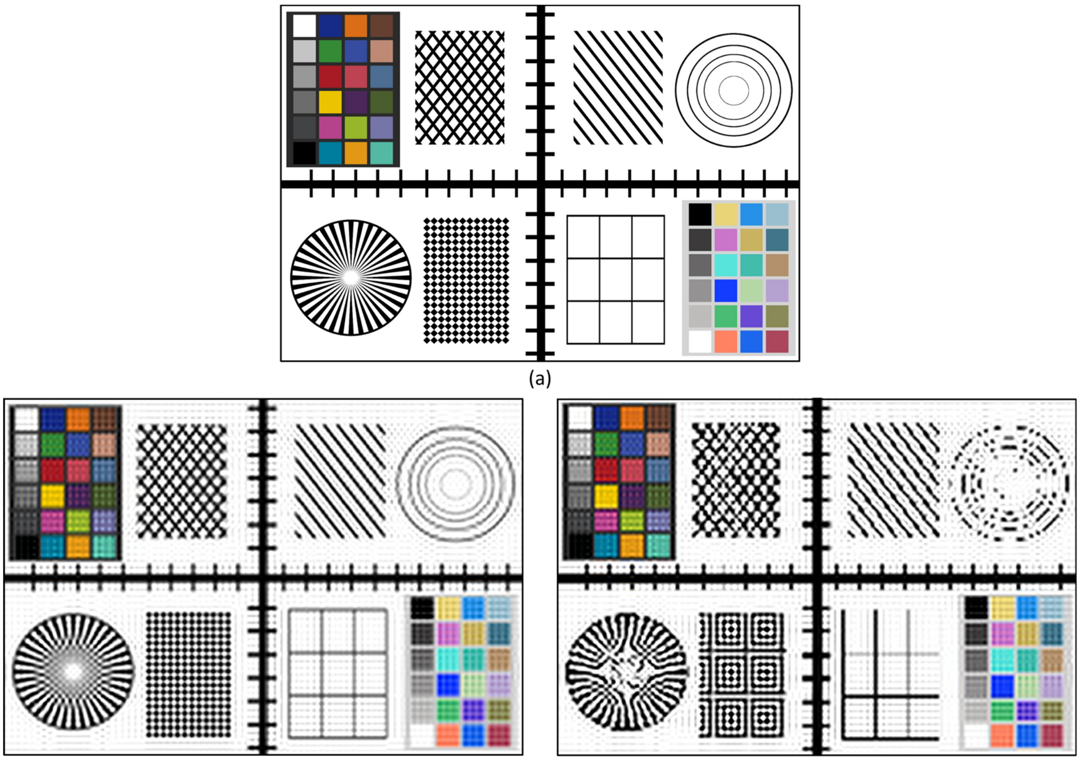

(a)

(b)

(c)

Figure 3.36. Visual comparison of (a) original test image, (b) visual hyperacuity simulation method (diffraction) and (c) diffraction-limited method.

The Fourier-based scheme has been implemented for multiple images of real scenes, in order to obtain extra results and better monitor the performance of the method (Figures 3.37, 3.38, 3.39 and 3.40). In all cases, original test images (a) are compared to the results obtained by means of the visual hyperacuity simulation method (b) and the simulation of a diffraction limited system with the same initial sensor size (c). The results speak for themselves: the proposed method capture high-resolution fine details that are not noticed in absence of diffraction, that is, a significant resolution improvement is achieved.

Table 3.2 shows the PSNR for the images obtained with both methods (taking original test images as a reference) and the improvement obtained thanks to diffraction. Notice how in this case the improvement seems to be smaller. This is because in this case FFT interpolation has been applied in the case of diffraction-limited simulation method, instead of nearest-neighbor interpolation as above, and it obtains better results.

Image	Hyperacuity Simulation Method PSNR (dB)	Diffraction-Limited Simulation Method PSNR (dB)	Improvement (dB)
Pattern	14.62	13.46	**1.16**
London Eye	16.76	14.81	**1.95**
City	20.17	17.89	**2.28**
Bike	20.20	18.17	**2.03**
Bridge	23.74	22.24	**1.5**

Table 3.2. PSNR of images with the hyperacuity simulation method, diffraction-limited simulation method and the improvement obtained using the proposed system.

3.6.4. Comments on the Method

Once again, it has been demonstrated how the introduction of a controlled diffraction pattern could play a key role on surpassing the resolution defined by the number and size of sensors of a given system, breaking the paradigm of the number of pixel sensors needed to capture an image and its final resolution.

From the standpoint of sensors, diffraction creates spatial diversity due to the spreading of light over the surface where sensors are located, improving the system sensitivity and increasing the SNR, for the reason that multiple sensors receive information from the same point source. In addition, it makes possible to capture or sense fine details that would be spatially located between detectors and could not be detected in absence of diffraction, when using a reduced number of sensors. Moreover, diffraction can be understood as an anti-aliasing filter which relaxes significantly signal sampling requirements, allowing the use of a reduced number of sensors for capturing the image. Spectral components truncated because of the subsampling cannot be recovered, but they seem not to be critical, due to the fact that the most important components are kept in low frequencies and most of the fine details in the image are resolved.

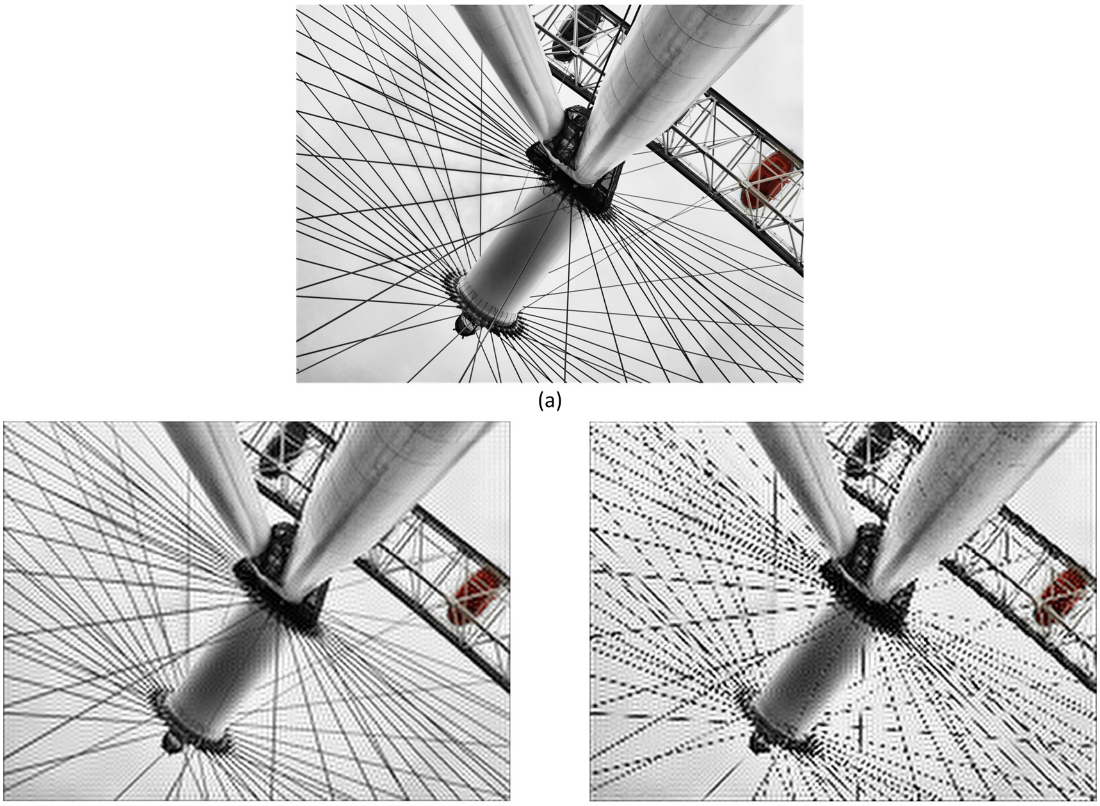

(a)

(b)

(c)

Figure 3.37. (a) Original test image. (b) Visual hyperacuity. (c) Diffraction-limited.

(a)

(b)

(c)

Figure 3.38. (a) Original test image. (b) Visual hyperacuity. (c) Diffraction-limited.

(a)

(b) (c)

Figure 3.39. (a) Original test image. (b) Visual hyperacuity. (c) Diffraction-limited.

(a)

(b) (c)

Figure 3.40. (a) Original test image. (b) Visual hyperacuity. (c) Diffraction-limited.

Yet, it is worth to mention that the inverse problem comes to be ill-posed and the system could show stability problems and be quite sensitive to small errors generated on account to interpolation. This instability can also be a serious issue in presence of noise, and it could involve the use of inverse functions or methods to minimize problems associated to noise amplification. Nevertheless, the attenuation and truncation of some high-frequency spectral components produced thanks to the diffraction and subsampling, reduces considerably problems related to stability and noise-amplification, allowing the use of a direct inverse filter. An important aspect to consider when facing the inverse problem as a global approach is that all the pixel values contained in the image as well as the same number of filter coefficients are involved all at once, what means that any displacement or mismatch may generate significant errors that make it difficult to obtain satisfactory results.

An additional important remark is that, since it is possible to obtain improved resolution images starting from a low number of sensors, the size of each pixel sensor might be increased (without the need to increase the image sensor size), resulting in higher dynamic range and improving the total SNR of the system. This would mean that our method could be taken into consideration when vision under poor lighting conditions is required, due to real improvement of the sensor’s sensitivity and unlike digital ISO works in digital cameras, amplifying both signal and noise.

3.7. Spectral Benefits of Diffraction for Imaging

This section analyzes the advantages and benefits produced by diffraction, once again through the comparison of the proposed method and the equivalent diffraction-free system, but based on spectral analysis.

The original test image in this case is a checkerboard with a black edge of 540×540 pixels such as the one displayed in Figure 3.41, where each square of the pattern has 11 pixels per side. This image has been intentionally chosen because it presents very specific spectral components, which come to be appropriate for the purpose of this section. It has been subsampled with a decimation factor of 5, both when introducing a controlled diffraction and without it, resulting in images of 108×108 pixels, aiming to simulate the use of few sensors for image capturing (see Figure 3.42).

Eventually, the image sizes have been increased up to 540×540 pixels via FFT interpolation and the one with diffraction inversely filtered. When observing the outcomes depicted in Figure 3.43, it is possible to appreciate how when applying the hyperacuity simulation method (with diffraction) the checkerboard pattern is perfectly reproduced. However, this does not occur in absence of diffraction, where a periodic pattern is obtained but it does not correspond to the original test image.

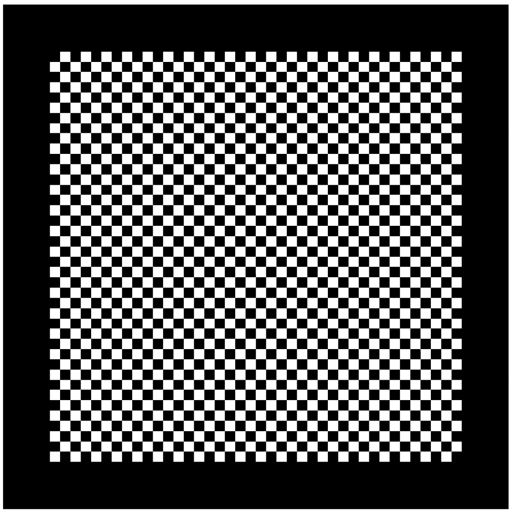

Figure 3.41. Original test image: checkerboard with a black edge (540×540 pixels).

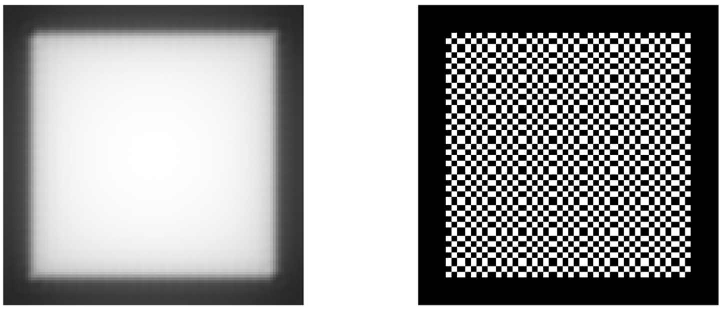

(a) (b)

Figure 3.42. Images captured by sensors (108×108 pixels): diffracted (a) and diffraction-free (b).

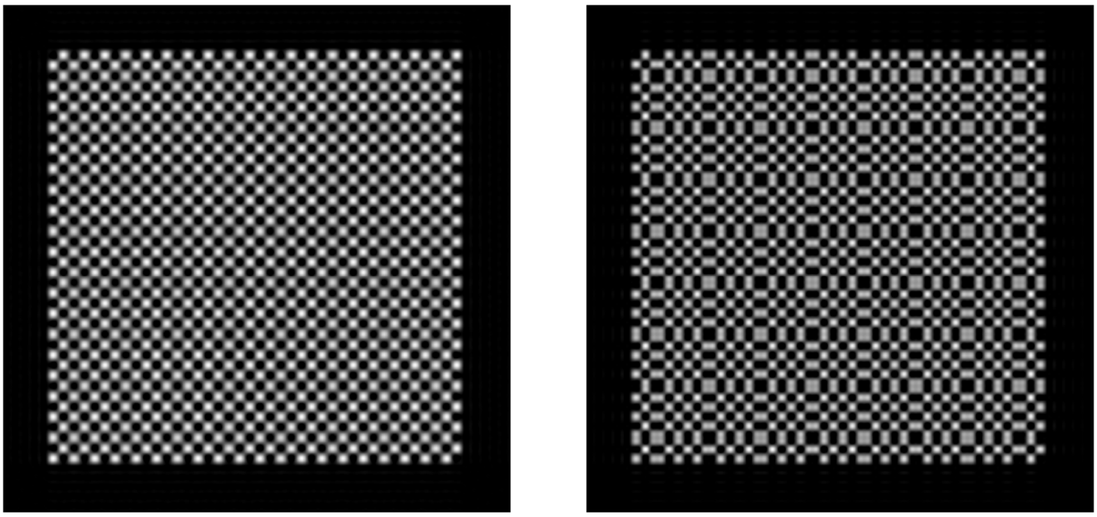

(a) (b)

Figure 3.43. Recovered images (540×540 pixels): with diffraction (a) and diffraction-free (b).

Figure 3.44 shows the original test image (a), the image recovered with diffraction and the one obtained in absence of diffraction (c) together with their corresponding periodograms, in order to represent the spectral density of each image. As can be seen, the process of subsampling has truncated the high-frequency spectral components of both images and they are not recovered even after applying interpolation or inverse filtering. Nevertheless, when focusing on the lower frequencies—where the most critical information is kept—the hyperacuity simulation method manages to reconstruct spectral components accurately when compared with the spectrum of the original test signal, but this is not the case in absence of diffraction. The introduction of diffraction can be understood as an anti-aliasing filter and allows images to be captured with a reduced number of sensors. Spectral components attenuated are subsequently recovered when the inverse filter is applied. However, when diffraction is not introduced in the system, the subsampling process generates aliasing corrupting frequency information and generating other spectral components which does not represent the ones in the original image and degrading the final outcome.

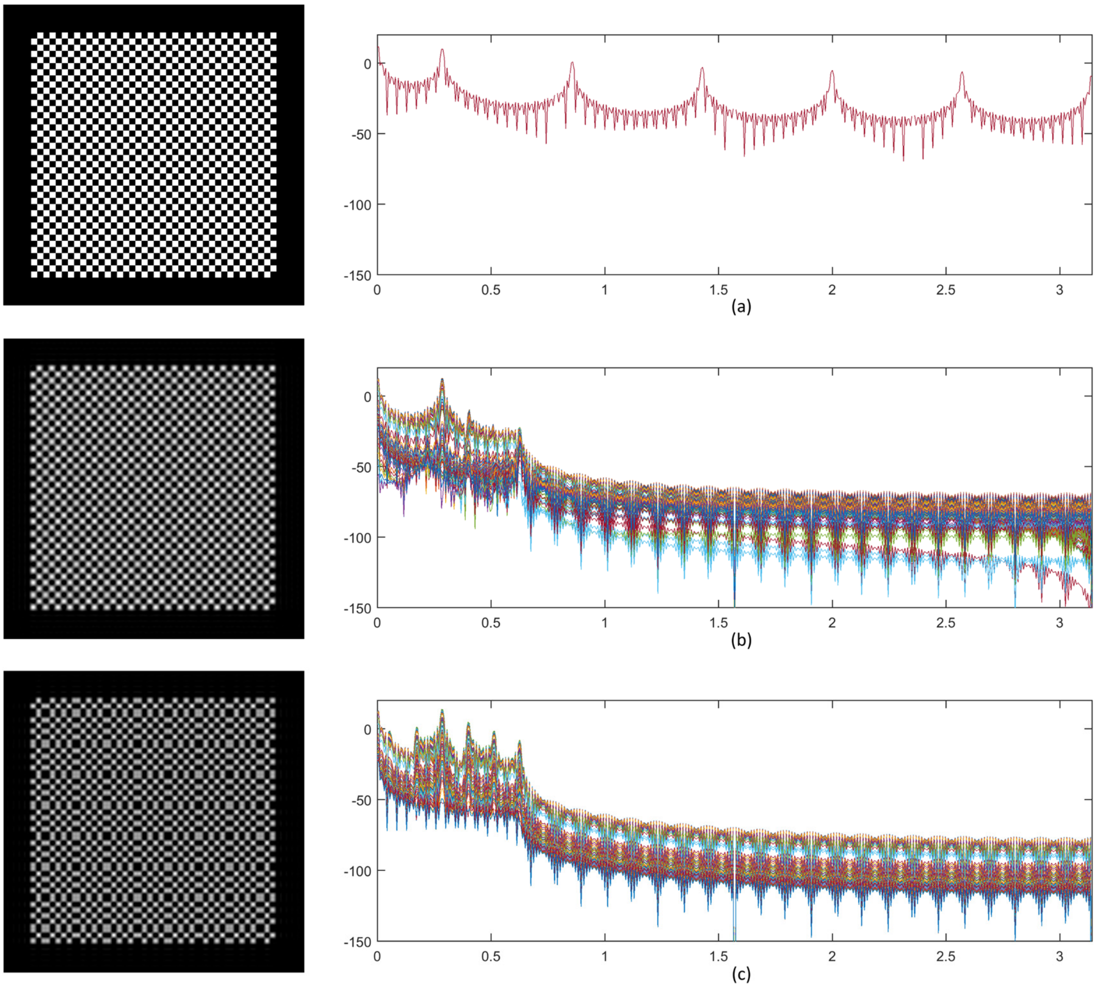

Figure 3.44. Checkerboard paterns and corresponding periodograms of: original test image (a), image recovered with diffraction (b) and image recovered difraction-free.

3.8. Conclusions

The design and implementation of imaging sensors and optical components to generate high-resolution images involves, in many cases, high economic and technological cost and it may not be practical depending on the nature of the application. These hardware-related complications could be faced using signal processing methods in order to obtain high-resolution images compensating this hardware charge with computational load.

SR imaging can be an interesting approach in many applications, but it also presents some difficulties that may not be solved in many cases. The visual hyperacuity simulation method could deal with some of these challenges, as long as multiple LR images are not required, the blur introduced by motion or other effects is used as a benefit for super-resolution and the simplicity of the system would suppose a considerable reduction in the computational cost.

In relation to THz imaging, the hyperacuity scheme could be of great help to exceed the resolution limits imposed by the low number of detectors available in imaging devices operating in this frequency band and it would suppose an important step forward for many applications. Additionally, the spatial diversity obtained thanks to diffraction would improve the sensitivity of the system offering advantages such as the increase of the working distance or the reduction of the radiation power, which is always a contentious and polarizing topic. Finally, the replacement of mechanical scanning systems with software-based resolution enhancement techniques would lead to a significant reduction in the in the time required for analyzing objects.

In view of the results obtained from simulations, it has been demonstrated how the introduction of a controlled diffraction pattern could play a key role on surpassing the resolution defined by the sensors of a given system, breaking the paradigm of the number of pixel sensors needed to capture an image and its final resolution. In this context, the method can be conceived as an explanation and simulation of visual hyperacuity.

The spatial diversity created by diffraction makes possible to capture fine details that would be lost in absence of diffraction when using a reduced number of sensors, because multiple sensors receive information from a single point source. In addition, diffraction acts as an anti-aliasing filter which relaxes signal sampling requirements, allowing the use of a reduced number of sensors for capturing the image.

On the negative side, inverse problems are ill-posed and the stability of the system may be compromised along due to the high sensitivity to small errors generated by interpolation and the presence of noise. It is therefore necessary the use of inverse functions or methods to minimize and control these aspects. Nevertheless, the attenuation and elimination of high-frequency spectral components produced by diffraction and subsampling reduces considerably stability and noise-amplification problems allowing, in some cases, the use of a direct inverse filter.

As a final remark, the opportunity to obtain high-resolution images from a low number of sensors could enable to increase the area of each pixel sensor, resulting in higher dynamic range and improving the SNR of the system, a matter of great importance for vision under poor lighting conditions, for example.

upna

Universidad Pública de Navarra
Nafarroako Unibertsitate Publikoa

Chapter 4

Applications of Visual Hyperacuity in Antenna Systems

4.1. Introduction

This chapter is mainly focused on the application of the basic concepts of visual hyperacuity to antenna systems, that could benefit from the proposed method in many ways, such as improving the angular resolution of the system, decreasing the overall size of a given antenna, increasing the scanning intervals or reducing the necessary number of data points for high-resolution signal reconstruction. Indeed, any antenna system, regardless of the operation frequency band (visible, infrared, terahertz, millimeter waves, etc.), can achieve angular resolutions significantly higher by taking advantage of the introduction of a known distortion which may later be removed. When it comes to antenna systems, the radiation pattern can be considered as the element which introduces the distortion or the PSF, due to the beam divergence.

The proposed method has been implemented by using MATLAB software simulations to show and prove the previously explained ideas. For this purpose, multiple tests have been carried out comparing antennas with different angular resolutions or beamwidths, varying the noise power (SNR) in the data acquisition process or modifying the sampling rates used to simulate the signal capturing. On this occasion, instead of using 2D images, the tests have been performed with 1D signals with a view to facilitating the development and analysis of the results. Once again, the outcomes have been analyzed from multiple perspectives, including visual observation, numerical quality metrics (e.g., Mean Squared Error) and the evaluation of spectral properties in some instances too.

The aim of this chapter is to generate a discussion and bring out a novel point of view on the angular resolution achieved by antenna systems, the related aperture size and the required sampling rate, among other factors.

4.2. Angular Resolution of Antenna Systems

When it comes to antenna systems, angular resolution is usually a parameter of critical importance in many applications. This spatial resolution is mainly determined by the Rayleigh resolution limit [111], which depends on the effective wavelength and the physic size of the antenna aperture, leading to large aperture antenna solutions when high resolutions are required.

The angular resolution of an antenna can be defined as the minimum angular separation where two equal point sources or targets must be located when at the same range (i.e. the minimum distance between objects to be resolved). This resolution is normally confined by the antenna beamwidth and more precisely by the full width half-maximum points (FWHM) or, equivalently, the 3 dB beamwidth (BW_{-3dB}). This parameter is defined in each of the principal planes as the angle between the points in the main lobe that are down from the maximum gain

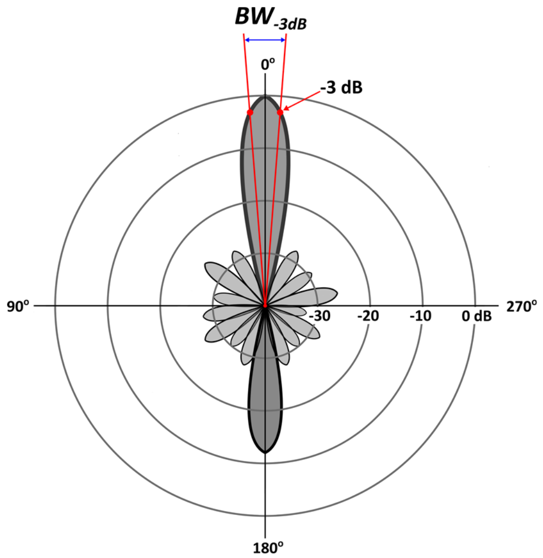

Figure 4.1. 3 dB beamwidth of an antenna radiation pattern in polar-coordinates.

by 3 dB (see Figure 4.1). Therefore, many efforts are oriented to create narrow high directivity beams by means of complex technological solutions and designs, often leading to large size devices. Another aspect to consider is that the acquisition of high-resolution signals requires sampling multiple data points at small scanning intervals and it usually takes too long time at antenna sweeps.

The close link between the antenna beamwidth and the angular resolution is fixed due to the fact that the received signal can be defined as the convolution of the antenna beam and the reflectivity of the observed scene and, thus, the wider the antenna beam is the lower angular resolution will be achieved [112]. The 1D signal $g[n]$ captured by the antenna can be modeled by a convolution:

$$g[n] = h[n] * f[n] \tag{4.1}$$

where $h[n]$ corresponds to the antenna beam and $f[n]$ represents the real scene where the targets are located. As a consequence of the convolution, the captured signal is blurred because of the low-pas filtering effect of the antenna beam. The way to avoid the blurring effect produced by overlapped beams is to perform the antenna sweep matching the scanning steps with the BW_{-3dB}. Therefore, under this approach, the only alternative to improve the angular resolution involves using antennas with narrower beamwidths (more directive) and decreasing scanning steps.

Let us analyze the mathematical relationship between the directivity, the beamwidth and the aperture (or effective area) of any antenna. The connection existing between the directivity and the antenna beamwidth can be obtained from the following equation:

$$D = \frac{4\pi}{\Omega_A} \cong \frac{4\pi}{\theta_{-3dB}\phi_{-3dB}} \tag{4.2}$$

where Ω_A represents the beam solid angle (approximated by the horizontal and vertical 3 dB beamwidth plane angles θ and ϕ). It follows therefore that directivity is inversely proportional to the antenna beamwidth, making necessary the use of high-directivity systems when high angular resolution is demanded and this condition impacts on the antenna effective area (equation 4.3), demanding large size antennas.

$$A_{eff} = \frac{\lambda^2}{4\pi} D \tag{4.3}$$

4.2.1. High Directivity Antennas

Given that high angular resolution antenna systems must generate high directivity beams, current antenna technologies are orientated towards two possible solutions or approaches: high-performance antenna arrays composed by multiple radiating elements and parabolic antennas with large size reflectors.

Many antenna array technologies can be cited where multiple individual radiating elements are devoted to creating a single spot beam, such as airborne and spaceborne Synthetic Aperture Radar (SAR) imaging systems [113], [114] or phased array antennas used by many communication satellites to create coverage spot maps over the earth surface [115]. Astronomical observation systems could also be included in this category, since a high directivity beam is created to obtain an image of the sky. This is the case of ESA's Planck mission, devised to provide a map of the Cosmic Microwave Background by means of LFI (Low Frequency Instrument) and HFI (High Frequency Instrument) which are equipped with receiver and detector arrays [115]. All these systems are equipped with high gain antenna arrays. The generation of a high-directivity beams is accomplished by means of the cooperation of multiple

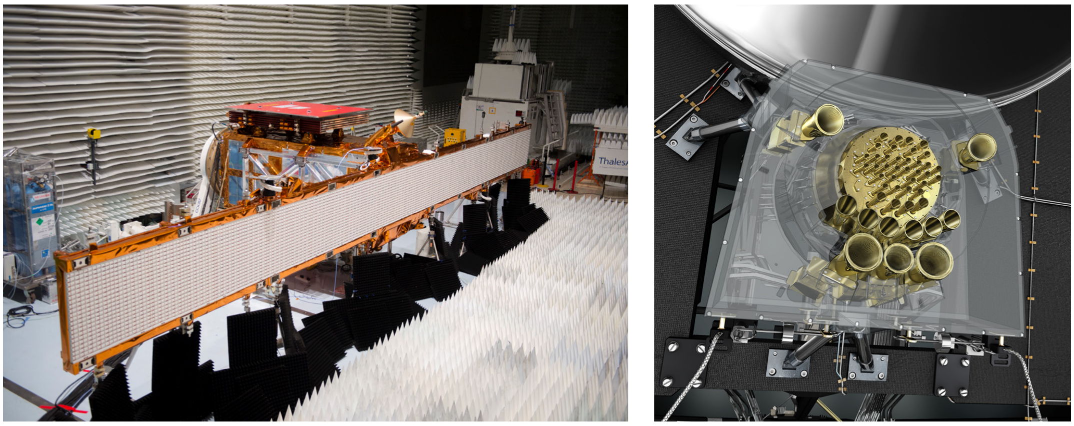

Figure 4.2. C-band SAR of Sentinel-1 satellite (left) and LFI/HFI instruments of the Planck spacecraft (right).

Credits: ESA.

individual antennas: the more radiating elements operating together, the more directive antennas. In consequence, these solutions are usually comprised of large aperture antenna systems.

On the other hand, we find technological approaches where sophisticated large size reflector systems are used to generate high directivity beams. The radio telescopes used for astronomical observation are a good example of that: the Arecibo Observatory in Puerto Rico outfitted with a spherical reflector of 305 m in diameter [116], Haystack Radio Telescope (ø37 m) in Massachusetts [117] or the Sardinia Radio Telescope [118], a fully steerable radio telescope with a diameter of 64 m, just to mention a few (see Figure 4.3). In other cases, higher angular resolutions are obtained by means of astronomical interferometers, consisting of radio telescope arrays working in conjunction to increase the resolution by means of interferometry techniques, e.g., the Atacama Large Millimeter Array (ALMA) in Chile [119] or the Very Large Array (VLA) in New Mexico [120], as can be observed in Figure 4.4.

In any event, the use of so large aperture antenna systems entails several challenges that need to be addressed at the design, implementation and construction stages, even during their operation lifetime. These demanding tasks can be related to diverse factors, such as the equipment's weight, physical dimensions, power supply, mechanical scanning difficulties or the specific constraints imposed by applications in each case, among others.

Figure 4.3. Arecibo Observatory (left), Haystack Observatory (center) and Sardinia Radio Telescope (right).

Sources: NAIC, MIT Haystack Observatory, INAF.

Figure 4.4. ALMA astronomical interferometer (left) and VLA observatory (right).

Sources: ALMA, NRAO.

4.3. Hyperacuity in Antenna Systems

As discussed earlier, the signal received by an antenna can be modeled as the convolution of the antenna beam and the reflectivity of the observed real scene, where the wider the antenna beam is, the more blurred the received signal will be. In other words, it acts as a low-pass filtering process where the highest frequencies are attenuated capturing a distorted signal. Hence, it is possible to apply the visual hyperacuity simulation method described in previous chapters to improve the angular resolution by using deconvolution methods, considering the ill-posed nature of the inverse process and its associated noise-amplification and stability problems.

Multiple approaches have been carried out to confront this topic, mainly in connection with the area of radar super-resolution—where the angular resolution becomes a matter of great importance—by proposing different deconvolution methods or algorithms [93], [121], [122]. All these methods are dedicated to improving the angular resolution of a given sophisticated antenna system, trying to achieve super-resolution with post-processing techniques.

Looked at from another perspective, the opportunity to increase the angular resolution using deconvolution methods enables the use of lower angular resolution antennas that achieve comparable results to those obtained with high performance devices. This approach is interesting given the fact that it would allow the use of much simpler antenna systems which may also lead to smaller effective area requirements and, consequently, smaller antenna sizes. Initially, this strategy would reduce considerably the angular resolution of the system, since a beam-overlapping effect is produced in the data acquisition process—Rayleigh criterion is not met—and high frequencies are attenuated. Therefore, it may require the use of some inverse filtering method, which could suppose problems linked to stability in presence of noise.

Additionally, taking advantage of the spectral band-limited nature of the captured data [123] and thanks to the blur introduced by the antenna beam, it is possible to perform a subsampling process increasing the sampling intervals (i.e., decrease the sampling frequency), reducing the total number of data points used for reconstructing the captured signal. This approach would considerably shorten the time used for sweeping the field of view (FOV) or making measurements of any type. What is more, in some cases the subsampling can virtually eliminate the high frequencies—the most critical spectral components related to noise-amplification and the stability of inverse problems—being substantially easier to implement an inverse filtering process.

4.4. 4x Reduction in Antenna Size. Angular Resolution & SNR Variations

Suppose a circular scanning radar antenna rotating 360° in azimuth, with a constant angular velocity. The signal captured by the antenna $g[n]$ can be modeled by the convolution:

$$g[n] = h[n] * f[n] + \eta \tag{4.4}$$

where *h*[n] is the antenna beam, *f*[n] the original test signal simulating a real scene and η additive white Gaussian noise. Assuming uniform angular steps Δθ of 0.5° for scanning the FOV, both *f*[n] and *g*[n] would have the same length of *N*=720 samples.

The Fourier transform of the data acquisition process is shown by:

$$G(\omega) = H(\omega) \cdot F(\omega) + \eta \,. \tag{4.5}$$

Due to the fact that $H(\omega)$ acts as a low-pass filter, the captured data *g*[*n*] has lost high frequency information and an inverse filtering or deconvolution process is required in order to recover an estimation of the original scene *f*[n]. The ill-posedness of the problem converts the system very sensitive to noise and this is why the restoration problem cannot be solved by simply applying an inverse filter $H^{-1}(\omega)$. Therefore, it is necessary to rely on an inverse function that minimizes the noise amplification. Marmolin *et al.* [69] proposed a simple restoring filter based on the Wiener filter which operates well when the scene and noise properties are unknown and it is approximated by the following equation:

$$R(\omega) = \frac{H^*(\omega)}{\left|H(\omega)\right|^2 + T} \,. \tag{4.6}$$

Note that the noise-to-signal power density ratio is approximated by a constant *T,* reflecting just some information about the relative magnitude of signal and noise. It should be observed how as $T \to 0$, the restoring filter is exactly an inverse filter. In general, high values of *T* implies a noise-free but a low performance filter, while low values of *T* allows better results but also an excessive noise magnification. The optimization of the restoring filter shown in equation 4.6 is achieved by means of the value of *T* that obtains an optimal balance between noise and resolution improvement.

4.4.1. Simulation Method

The two antenna patterns used in the simulation process can be seen in Figure 4.5. Both are Gaussian beam functions, but with different angular resolutions defined by the 3 dB beamwidth of 1° and 4°. Antenna beams are sampled each 0.5 degrees that matches with scanning angular steps Δθ. If we compare antenna directivities based on equation 4.2, it can be deduced that the low angular resolution antenna beam is four times less directive than the high-resolution one. Therefore, from equation 4.3 we can conclude that the antenna effective area—and therefore the antenna size—is also reduced at the same rate.

The original test signal simulating a real scene over the FOV of 360° considered for simulation is shown in Figure 4.6, where different size targets have been placed at multiple ranges and angular distances. The scanning of the FOV using the previously characterized antenna beams is performed by signal spectrum multiplication as explained in equation 5.4, adding white Gaussian

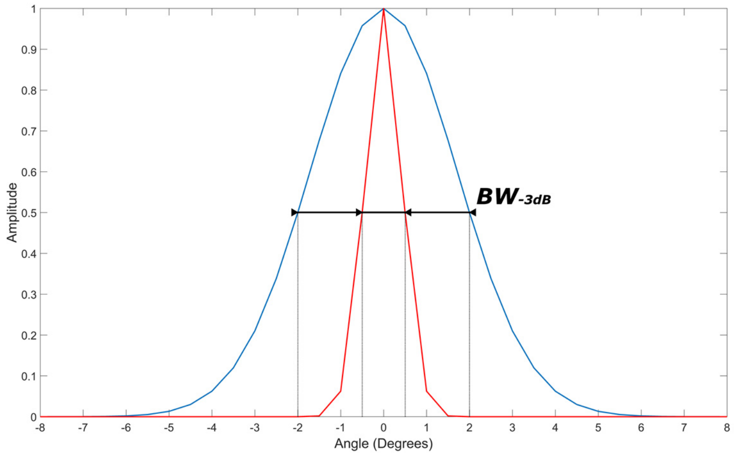

Figure 4.5. Gaussian antenna patterns used for simulation.
BW_{-3dB}=1° (red) and BW_{-3dB}=4° (blue).

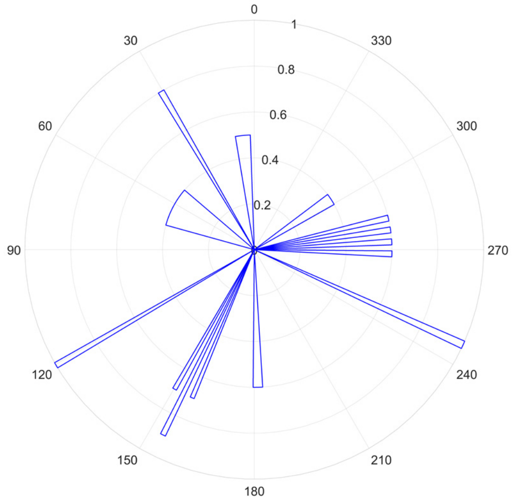

Figure 4.6. Original test signal: target distribution over the scanned FOV of 360˚ in polar coordinates.

noise in order to reproduce realistic conditions, as a noisy environment (see Figure 4.7). By looking at Figure 4.7 (a) it is hard to appreciate a loss of resolution, due to the angular resolution of the beam (BW_{-3dB}=1°). When observing Figure 4.7 (b) instead, as a result of the less directive beam (BW_{-3dB}=4°) and small angular steps $\Delta\theta$=0.5° used for scanning, each section of the FOV is illuminated by multiple beams, creating a significant overlapping effect. As a consequence, angular resolution is lost, being difficult to distinguish adjacent targets and also range information has been corrupted. It is clear that a loss of high-frequency information has occurred during the data acquisition process.

Using the inverse function described in equation 4.6, it is possible to reverse this effect, obtaining similar results to those obtained by means of the BW_{-3db}=1° antenna, always taking into account the limits imposed by the ill-posedness of the system and the consequent noise

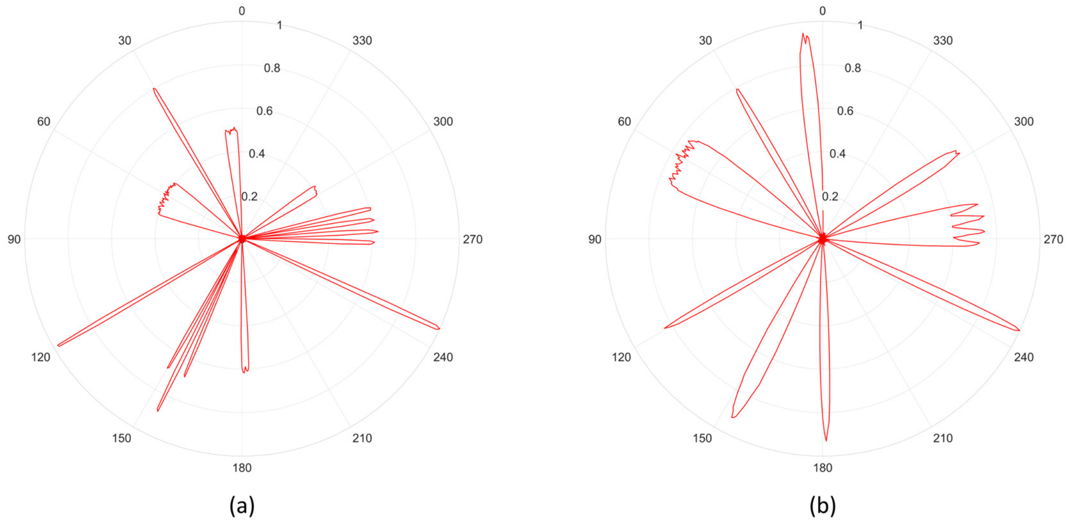

Figure 4.7. Simulation of data acquisition by scanning the FOV with antennas of BW_{-3dB}=1˚ (a) and BW_{-3dB}=4˚ (b), SNR=35 dB.

amplification. The objective is to calculate an estimation $F'(\omega)$ of the real scene from the signal captured by the antenna $G(\omega)$ using the inverse function $R(\omega)$. Operating in frequency domain it works as follows:

$$F'(\omega) = G(\omega)\cdot R(\omega) = G(\omega)\cdot \frac{H^{*}(\omega)}{\left|H(\omega)\right|^{2}+T} . \tag{4.7}$$

This process requires determining the value of the constant T, needing to find a compromise between resolution improvement and noise amplification. In this case, the optimum value of T has been obtained according to the calculation of the Mean Squared Error (MSE) as in equation 4.8, between the real scene $f[n]$ and the estimation of the real scene $f'[n]$ for a signal length of N=720 samples, trying to minimize it as much as possible. Due to the randomness of the additive white Gaussian noise, the outcome varies smoothly and also the corresponding MSE. Therefore, the calculation has been made 1000 times, obtaining the average value afterwards.

$$MSE = \frac{1}{N}\sum_{n=1}^{N}\left(f'[n]-f[n]\right)^{2} \tag{4.8}$$

4.4.2. Results

The whole process described above has been carried out for different signal-to-noise ratio (SNR) values, adjusting the constant T to minimize the MSE in each case. Table 4.1 contains the MSE results obtained from the simulation of data acquisition by scanning the FOV with antenna beamwidths of BW_{-3dB}=1° (first column) and BW_{-3dB}=4° (second column) for different SNR values. Notice how the results are significantly worse in the second case, due to the low angular resolution of the antenna beam. The third column represents the MSE for the estimation of the real scene $f'[n]$ after performing the inverse filtering process to the data captured with the antenna of BW_{-3dB}=4°. Even if the MSE values are not as good as the ones obtained with the antenna of BW_{-3dB}=1°, it is possible to appreciate a sharp improvement, being rather close to the values achieved with the antenna of high angular resolution.

For a better visualization, Figure 4.8 shows simulation results of data acquisition by scanning the FOV with the antenna of BW_{-3dB}=1° compared to the estimation of the real scene when capturing with BW_{-3dB}=4° and performing the inverse filtering, for different SNR values. Observe how results are highly satisfactory with respect to angular resolution. Nevertheless, the amplitude or range of the estimated signal is slightly affected by the noise amplification due to stability and noise-amplification problems of the system, mostly for low SNR values.

These results show how might be possible to obtain high angular resolution for an antenna system using a less directive beam, and therefore, a smaller effective area. In this case antennas with 3 dB beamwidths of 1 and 4 degrees have been compared, achieving quite successful and similar results when it comes to angular resolution, by applying post-processing techniques.

The proposed approach could have a direct impact on the antenna design process, since it is possible to reduce considerably the effective area or aperture, and consequently the antenna size used in many applications. This idea could relax significantly the limitations related to the antenna size and, therefore, the problems associated with the equipment weight, physical dimensions, mechanical scanning difficulties or remote power supply, just to mention a few.

SNR (dB)	$\overline{MSE}_{1000}$ *(BW_{-3dB}=1°)*	$\overline{MSE}_{1000}$ *(BW_{-3dB}=4°)*	$\overline{MSE}_{1000}$ *(BW_{-3dB}=4° & Inverse Filter)*	***T***
15	0.0044	0.0433	0.0121	*0.600*
20	0.0032	0.0405	0.0101	*0.200*
25	0.0029	0.0396	0.0086	*0.070*
30	0.0027	0.0393	0.0074	*0.030*
35	0.0027	0.0392	0.0064	*0.008*
40	0.0027	0.0392	0.0055	*0.004*

Table 4.1. Average Mean Squared Error for different SNR and *T* values (1000 iterations).

4.5. Antenna Beamwidth vs. Angular Resolution from a Spectral Perspective

On this occasion, as in the previous section, the data acquisition process of a circular scanning radar antenna rotating 360° in azimuth with a constant angular velocity is modeled by means of a convolution, as suggested in equation 4.4.

Considering that the antenna beams act as a low-pass filter, it becomes interesting the use of some deconvolution or inverse filtering process to recover an estimation of the original scene $f[n]$ with an improved angular resolution. Due to the fact that the problem is ill-posed, this

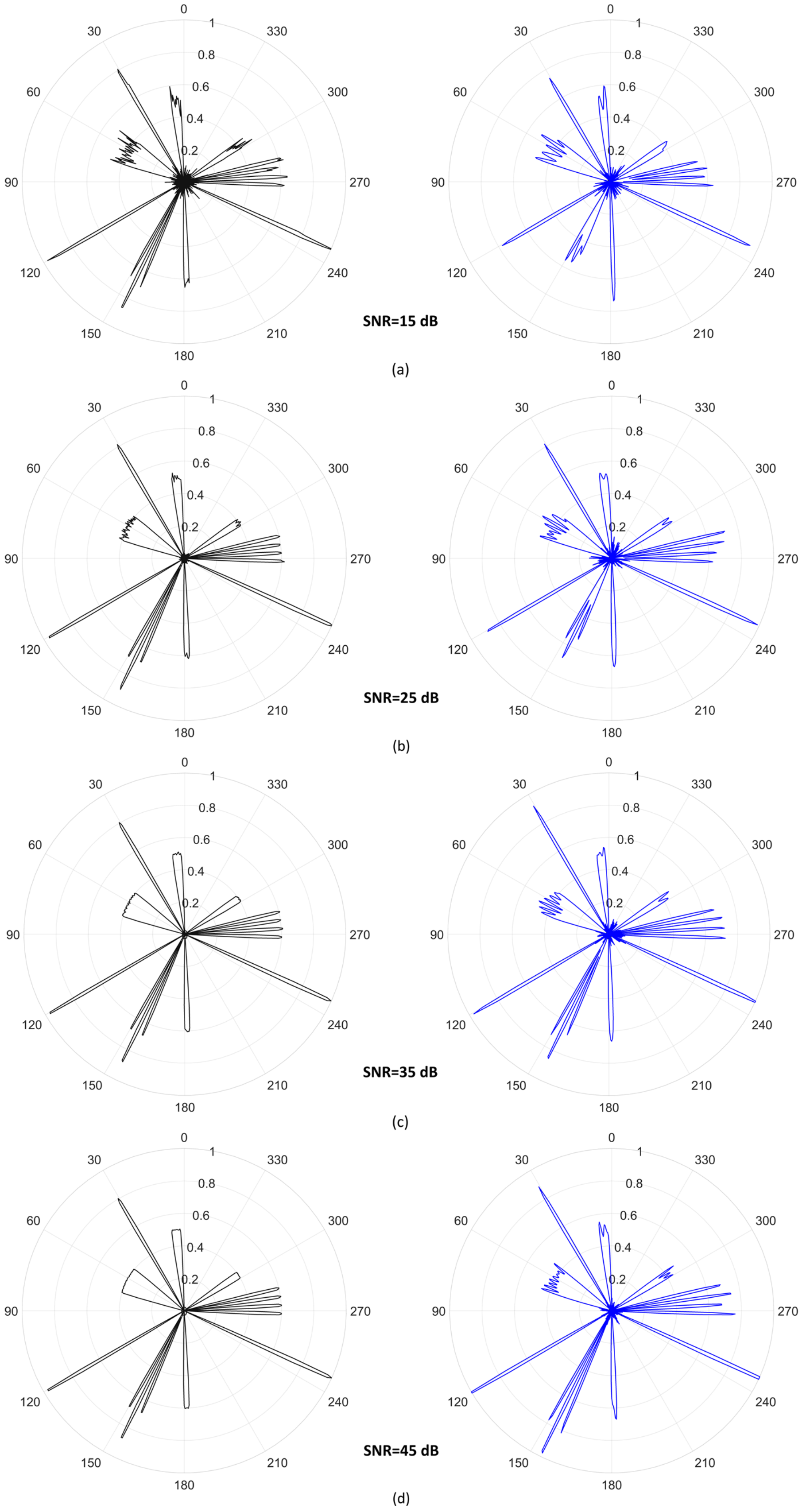

Figure 4.8. Simulation of data acquisition with the antenna beam of BW_{-3dB}=1° (black) and estimation when capturing with the antenna beam of BW_{-3dB}=4° and inverse filtering (blue) for: (a) SNR=15 dB, (b) SNR=25 dB, (c) SNR=35 dB and (d) SNR=45 dB.

matter must be solved with the aid of an inverse function that controls the stability issue and minimizes noise amplification such as the one shown in equation 4.6, where the constant *T* approximates the noise-to-signal power density ratio.

Once again, the objective is to calculate an estimation *f'*[n] of the real scene from de signal captured by the antenna *g*[n], operating in the frequency domain as explained in equation 4.7. The optimum value of the constant *T* is found by minimizing the MSE as much as possible when comparing the original test signal *f*[n] and the estimation *f'*[n] (see equation 4.8).

In this case, in addition to observing the MSE and visualizing graphically the results when using antennas with different angular resolutions, the outcomes will be analyzed in the frequency domain. The fact that the value of *T* represents a compromise between noise amplification and resolution improvement (high values of *T* entail a noise-free but a low performance filter, while a better filtering performance but an excessive noise magnification is obtained with low values of *T*), suggests that in some way emulates the concept of regularization. The introduction of additional information by means of the parameter *T* somehow produces a truncation of the most unstable spectral components corresponding to high frequencies, stabilizing the inverse problem. Therefore, the analysis in the frequency domain becomes interesting, in order to observe the consequences of this spectral truncation on the outcomes.

4.5.1. Simulation Method

Figure 4.9 shows two different original test signals, simulating target distributions over the FOV of 360°. Both signals have an angular resolution of 0.5°, resulting in a signal length of *N*=720 samples. In Figure 4.9 (a) multiple size targets have been located at different ranges and angular

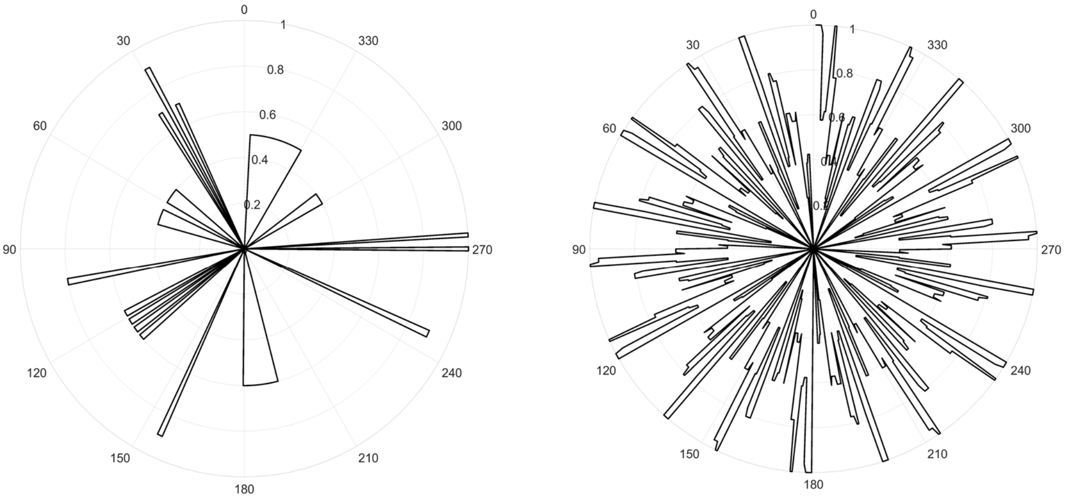

(a) (b)

Figure 4.9. Target distribution over the FOV of 360˚: (a) multiple size targets at different ranges and angular distances; (b) sum of different frequency square waves.

distances trying to emulate realistic objects, and it will be useful to evaluate the improvement of angular resolution of the method. Besides, Figure 4.9 (b) is a sum of different frequency square waves, that is more helpful to evaluate the recovery of spectral components.

The process of data acquisition has been simulated using different angular resolution Gaussian beam antenna patterns with 3 dB beamwidths of 1°, 2° and 4° (see Figure 4.10). Analyzing antenna directivities based on equation 4.2 and associating with the effective area using equation 4.3, it can be deduced that the effective area of the antenna with a BW_{-3dB}=4° would be reduced by a factor of 2 compared to the antenna of BW_{-3dB}=2° and by a factor of 4 in relation with the antenna of BW_{-3dB}=1°. Taking into account the angular resolution of 0.5° of the original signal, is important to note that the resolution of the antenna with a BW_{-3dB}=4° is 8 times lower (4 and 2 times lower for the antennas of BW_{-3dB}=2° and BW_{-3dB}=1° respectively).

The simulated scanning of the FOV is performed by signal spectrum multiplication as explained inequation 4.5 for the different angular resolution antenna beams and adding white Gaussian noise, assuming a SNR of 25 dB, to reproduce more realistic conditions when performing the data acquisition process. Figure 4.11 represents the captured signal $g[n]$ as a result of scanning the multiple target distribution over the FOV shown in Figure 4.9 (a) with antenna beams of BW_{-3dB}=1°, BW_{-3dB}=2° and BW_{-3dB}=4° consecutively (red), together with the original test signal $f[n]$ (grey) to enable better visual comparison and their corresponding spectra in the range $[-\pi,\pi]$. Figure 4.12 displays the analogous results when scanning the signal shown in Figure 4.9 (b), the sum of different frequency square waves. It is possible to appreciate the loss angular resolution and the attenuation of high-frequency spectral components when comparing captured data to the original test signal and its corresponding spectra. This effect becomes more significant the lower the antenna angular resolution is—the wider the 3 dB beamwidth—, being difficult to distinguish contiguous targets in many cases and observing also inaccurate range information, due to the effect of beam overlapping.

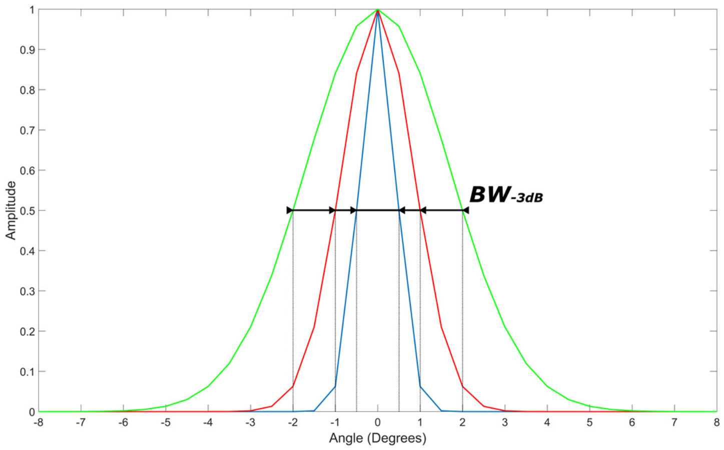

Figure 4.10. Gaussian beam antenna patterns used for simulation. BW_{-3dB}=1° (blue), BW_{-3dB}=2° (red) and BW_{-3dB}=4° (green).

The next step consists of applying the inverse function as previously described in equation 4.7 to achieve an estimation of the real scene *f'*[*n*] and reverse the negative effect produced by the antenna beam during the data acquisition simulation, always considering the limits imposed by the ill-posed system and its related stability and noise amplification problems.

BW_{-3dB}=1°

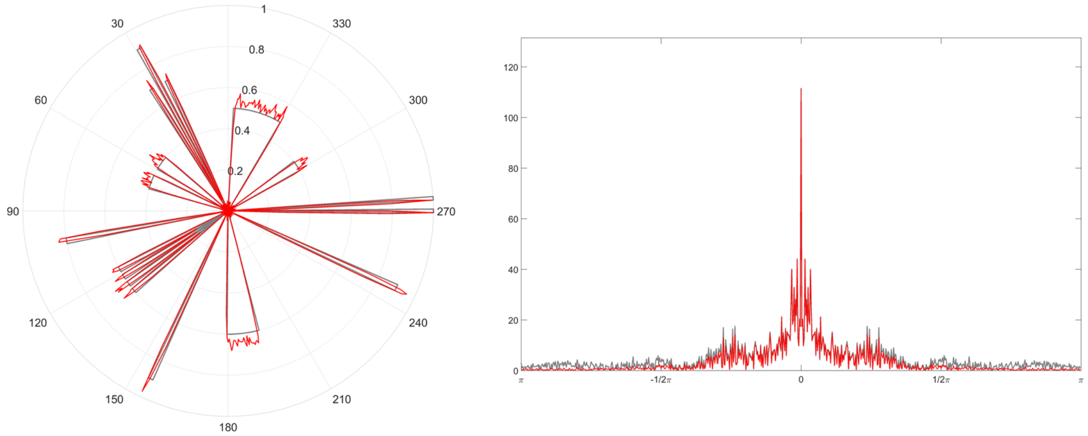

BW_{-3dB}=2°

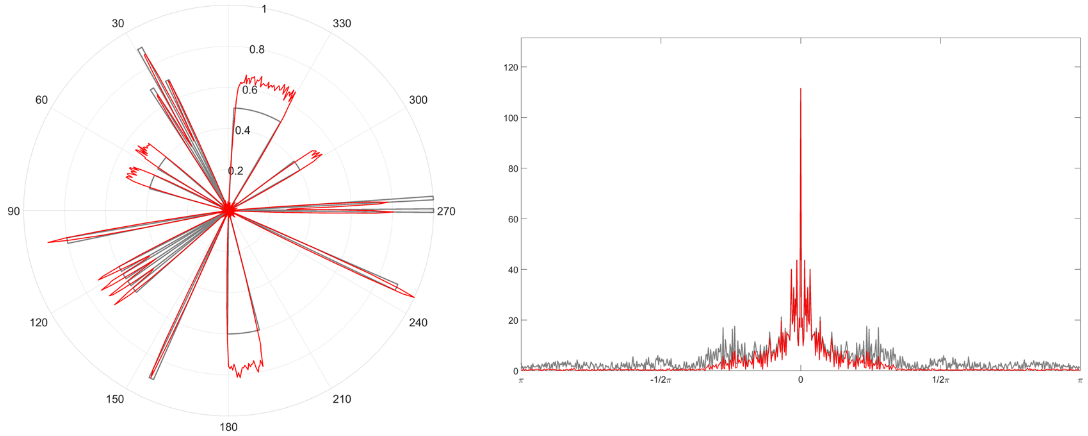

BW_{-3dB}=4°

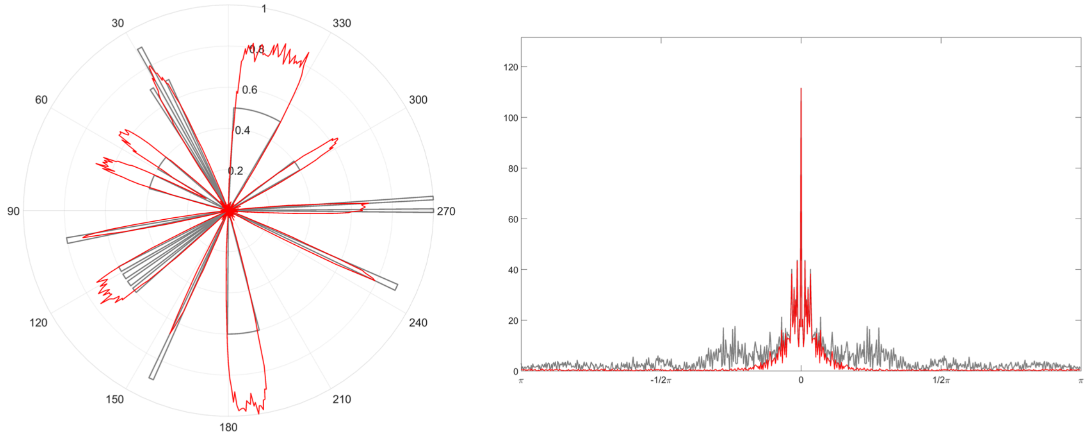

Figure 4.11. Simulation of data acquisition with antenna beams of *BW_{-3dB}*=1°, *BW_{-3dB}*=2° and *BW_{-3dB}*=4° and corresponding spectra (original test signal: multiple size targets at different ranges and angular distances). SNR=25 dB.

BW$_{-3dB}$=1°

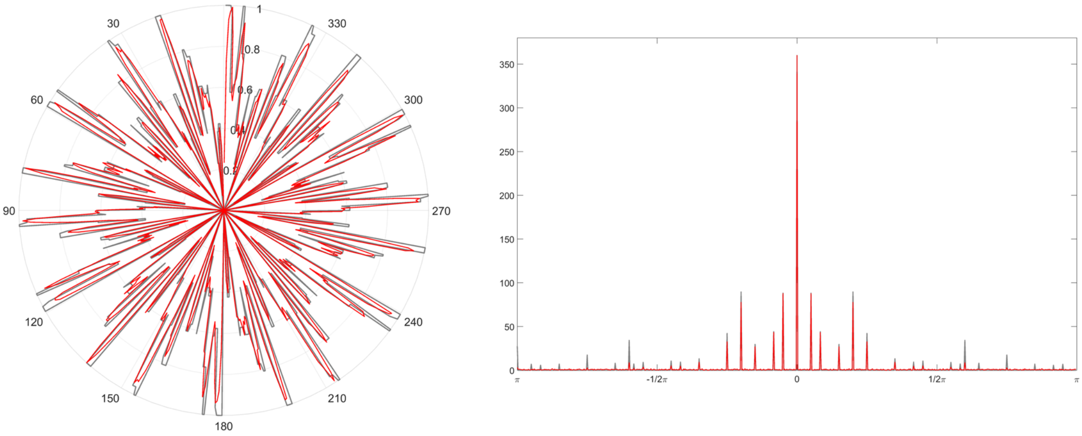

BW$_{-3dB}$=2°

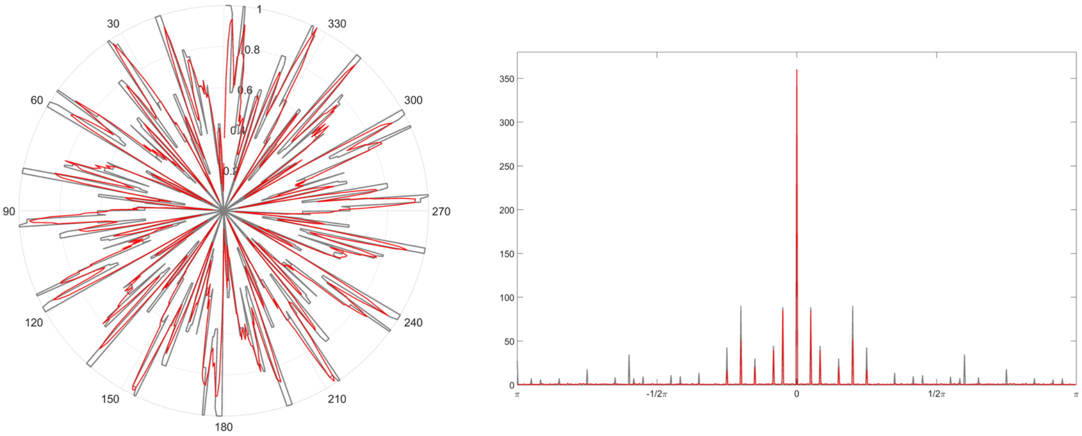

BW$_{-3dB}$=4°

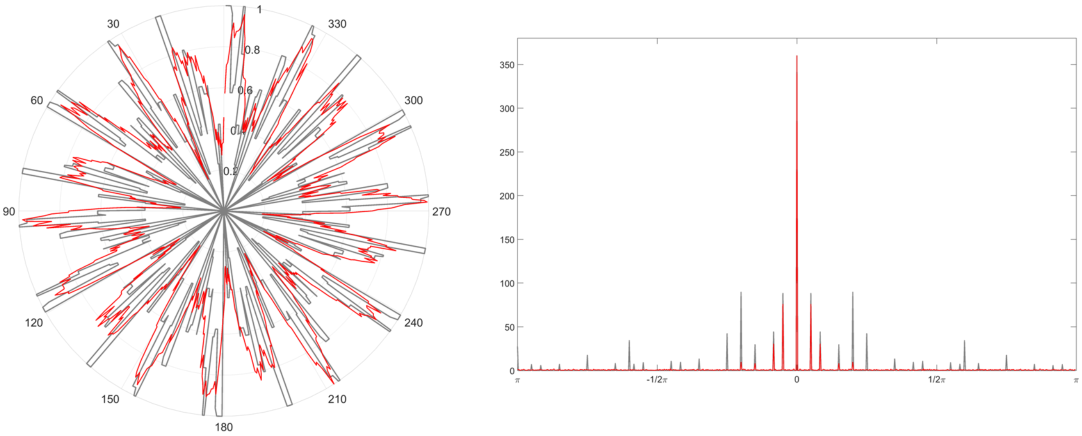

Figure 4.12. Simulation of data acquisition with antenna beams of *BW*$_{-3dB}$=1°, *BW*$_{-3dB}$=2° and *BW*$_{-3dB}$=4° and corresponding spectra (original test signal: sum of different frequency square waves). SNR=25 dB.

4.5.2. Results

The outcomes of implementing the inverse filtering to recover the estimation of the original test signal are displayed in Figure 4.13 (multiple size targets at different ranges and angular distances) and Figure 4.14 (sum of different frequency square waves). Observe how the results are highly satisfactory locating and identifying different targets when related to angular resolution in all cases. Nevertheless, the range information (amplitude) is slightly affected due to the noise amplification associated to the system instability, mostly for signals captured with lower angular resolution antenna beams. It is also possible to observe how the previously attenuated high-frequency components have been recovered, being directly linked with the improvement of angular resolution. Spectral components truncated as a result of the constant T to approximate the noise-to-signal power density ration when applying the inverse filter (the highest frequencies) can no longer be recovered. However, the most important spectral components are in the lower frequencies and the angular resolution does not appear to be influenced too much by this condition, since a good signal reconstruction is achieved.

The MSE values obtained for different signals and antenna beamwidths are shown in Table 4.2. Observe how the error is considerably reduced when comparing the captured data $g[n]$ with the recovered estimation $f'[n]$ after applying the inverse function, demonstrating that noise amplification problem has been controlled in a significant way.

On this occasion as well, it has been demonstrated how it could be possible to get high angular resolution for antenna systems by means of devices with less directive antenna beams, and thus, smaller effective areas or apertures. Antennas with 3 dB beamwidths of 1°, 2° and 4° have been used to capture signals with an angular resolution of 0.5°, achieving successful outcomes.

Data Signal	BW_{-3dB}	T	**MSE $g[n]$** $\times 10^{-3}$	**MSE $f'[n]$** $\times 10^{-3}$
Multiple Targets	**1°**	0.034	15.70	0.82
	2°	0.031	19.60	4.00
	4°	0.020	44.00	9.80
Sum of Squared Waves	**1°**	0.050	29.10	2.20
	2°	0.090	31.10	8.90
	4°	0.060	63.10	12.80

Table 4.2. MSE for different BW_{-3dB} and T values, comparing the captured signal $g[n]$ and the estimation of the original test signal $f'[n]$.

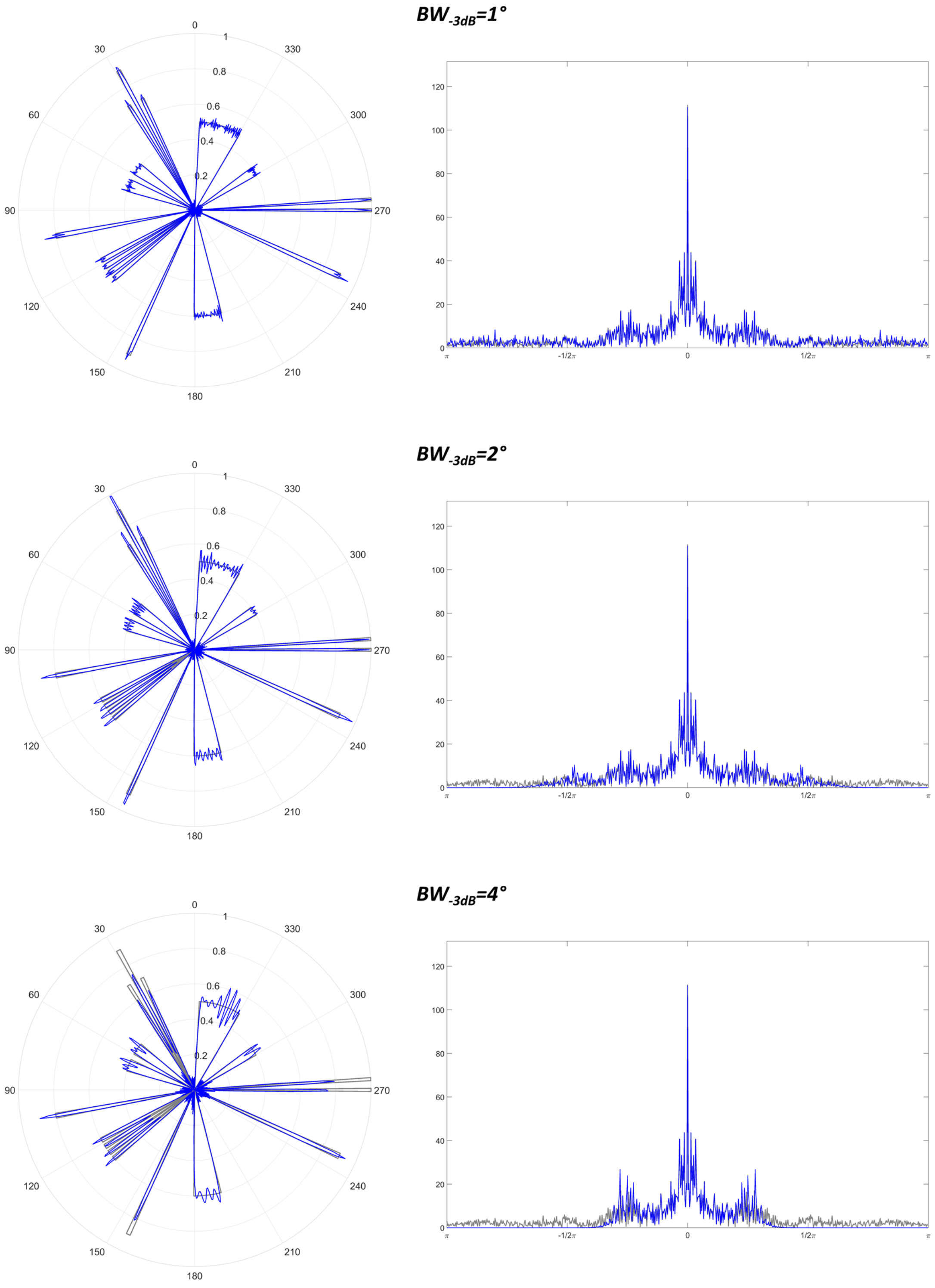

Figure 4.13. Estimation of the real scene after performing the inverse filtering for signals captured with antenna beams of BW_{-3dB}=1°, BW_{-3dB}=2° and BW_{-3dB}=4° and corresponding spectra (original test signal: multiple size target at different ranges and angular distances).

BW_{-3dB}=1°

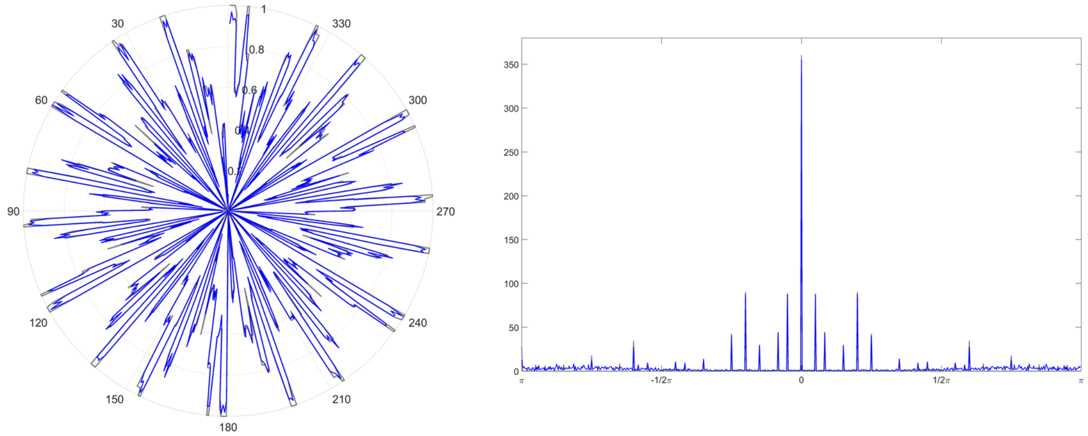

BW_{-3dB}=2°

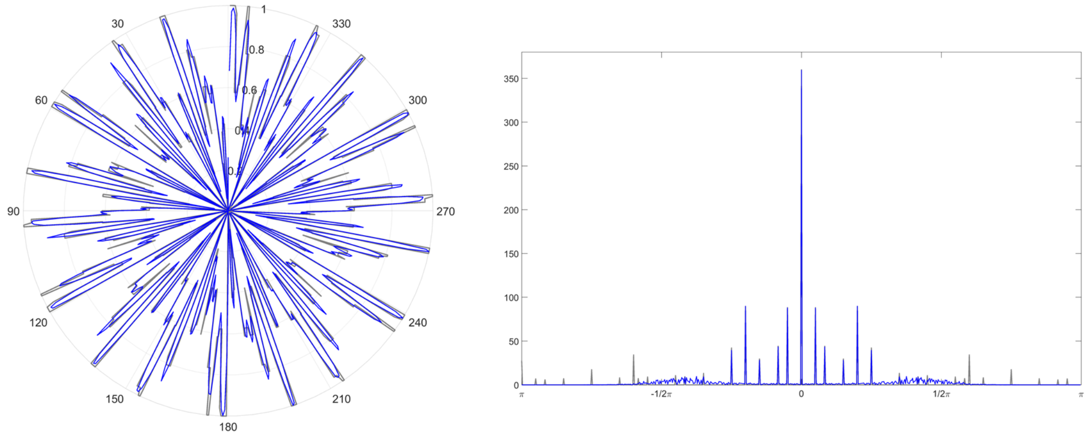

BW_{-3dB}=4°

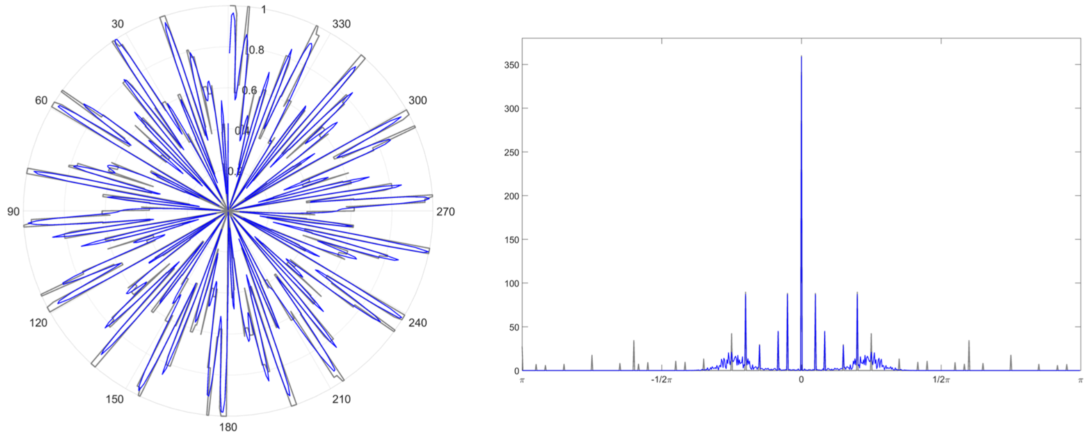

Figure 4.14. Estimation of the real scene after performing the inverse filtering for signals captured with antenna beams of BW_{-3dB}=1°, BW_{-3dB}=2° and BW_{-3dB}=4° and corresponding spectra (original test signal: sum of different frequency square waves).

4.6. Antenna Size Reduction and Subsampling

The previous approaches have shown the possibility of improving the angular resolution of a given antenna system using deconvolution methods, which in turn enables the use of lower angular resolution—and smaller—antennas to achieve outcomes close to the ones obtained with higher performance systems. The beam-overlapping effect produced by the antenna beam in the first instance (Rayleigh criterion is contravened), reduces considerably the angular resolution of the system but, at the same time, taking advantage of the spectral band-limited nature of the captured data [123], it is possible to perform a subsampling process reducing the total data points of the captured signal $g[n]$. In simulation, it would be equivalent to decrease the sampling rate or, in other words, increase the sampling intervals.

The use of a reduced number of samples to reconstruct a high angular resolution signal brings multiples benefits. First of all, the antenna sweep time for scanning the FOV can be greatly shortened, since fewer measurements must be carried out. Analogously, the reduction of the data points required for signal reconstruction allows the system to expend more time in each measurement, thereby improving the SNR and aspects that could be profiting from time integration, such as the range resolution of a radar system, for example. Furthermore, with respect to the method proposed in this section, the process of subsampling practically truncates the most critical spectral components (high frequencies) connected to noise-amplification and stability problems associated to the inverse problem, thus facilitating the implementation of an inverse filtering.

4.6.1. Simulation Method

Target distribution over the FOV of 360˚ considered for simulation (original test signal $f[n]$ in Cartesian coordinates) is shown in Figure 4.15, aiming to simulate realistic objects located at multiple positions. The test signal used for simulation has an angular resolution of 0.5˚, yielding a signal length of N=720 samples.

Two antenna beam patterns $h[n]$ have been used at the data acquisition simulation process. Both are Gaussian functions, but with different angular resolutions defined by the 3 dB

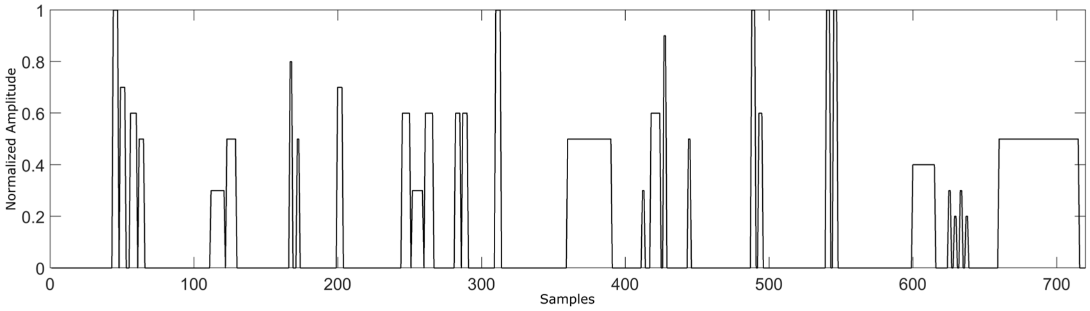

Figure 4.15. Target distribution over FOV of 360˚ (original test signal). N=720 samples.

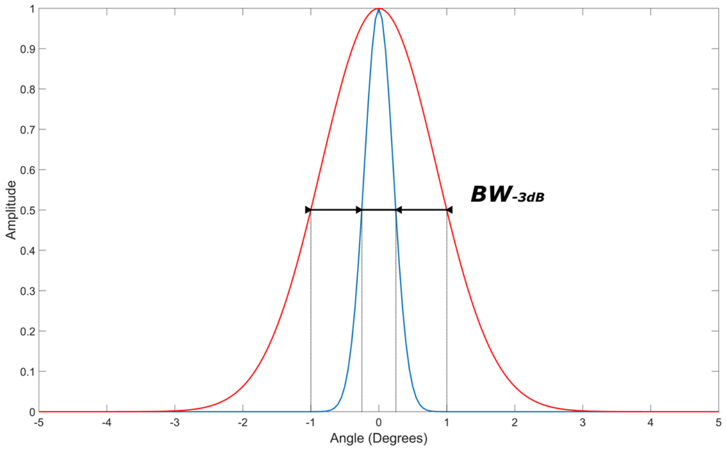

Figure 4.16. Gaussian antenna beam patterns of BW_{-3dB}=2˚ (red) and BW_{-3dB}=0.5˚ (blue) used for simulation.

beamwidth of 0.5˚ and 2˚ (see Figure 4.16). Antenna beams are sampled each at 0.5 degrees, which implies that the BW_{-3dB} are of 1 and 4 samples respectively. The low angular resolution antenna with a BW_{-3dB}=2˚ is four times less directive than the high-resolution one (BW_{-3dB}=1˚). Accordingly, the antenna effective area is also reduced by the same proportion, as the supposed antenna size.

The scanning of the FOV using the previously characterized antenna beams is performed by multiplication of Fourier Transforms, adding white Gaussian noise and assuming a SNR of 25 dB (see Figure 4.17). When capturing the signal with the antenna beam of BW_{-3dB}=0.5˚ and sampling intervals of 1 sample (blue), almost no information is lost due to the high angular resolution of the antenna (Rayleigh is met) and most of the errors are produced by the presence of noise. However, when using the less directive antenna beam of BW_{-3dB}=2˚ and equal sampling intervals of 1 sample (red), each section of the FOV is illuminated by multiple beams (Rayleigh criterion is contravened), creating a significant overlapping effect that corrupts the information on range. Additionally, angular resolution is lost, which renders difficult distinguishing adjacent targets. Both signals have a signal length of N=720 samples.

When analyzing these signals in the frequency domain (observe Figure 4.18), the signal captured using the high-resolution antenna of BW_{3dB}=0.5˚ (blue) captures almost all spectral components of the original test signal (grey). On the contrary, observe the low-pass filter effect produced by the antenna beam of BW_{-3dB}=2˚ (red), attenuating high frequency components and producing a loss of angular resolution: the spectrum drops to very low values from a given spectral index (below -40 dB). Nevertheless, this signal seems to be oversampled (4 samples per antenna beamwidth) and we could subsample it (while still meeting the Nyquist sampling theorem), truncating the high frequency spectral components, the most critical ones when performing an inverse filtering process.

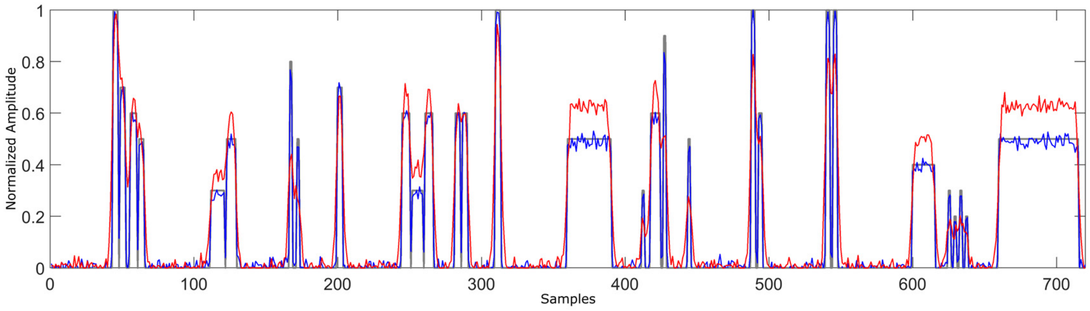

Figure 4.17. Signal acquisition with antennas of BW_{-3dB}=0.5˚ (blue) and BW_{-3dB}=2˚ (red), compared to the original test signal (grey). N=720 samples, SNR=25 dB.

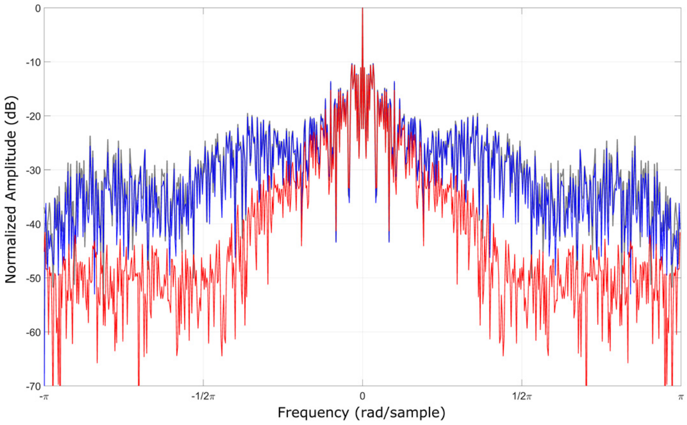

Figure 4.18. Spectra of acquired signals for BW_{-3dB}=0.5˚ (blue) and BW_{-3dB}=2˚ (red), compared to the spectrum of the original test signal (grey).

Figure 4.19 shows the result of applying a decimation factor 2 to the low angular resolution signal, while its spectrum is depicted in Figure 4.20. This subsampling process is equivalent to increasing scanning intervals up to 1˚ (or 2 samples), thereby reducing the signal length down to N=360 samples when the data capturing process is performed. Notice how the signal has not suffered relevant modifications and the most significant spectral components in the passband are kept. The captured signal can now be interpolated by means of the FFT interpolation method, consisting in a simple spectrum zero-padding, to increase the signal data points. In this case, a factor 2 FFT interpolation has been used, obtaining a signal length of N=720 samples.

The last step involves processing through an inverse filter that recovers the signal consisting in a high-resolution estimation of the original test signal $f[n]$. The subsampling process performed in advance greatly reduces instability and noise-amplification issues associated with inverse problems, since high frequency spectral components have been removed. Therefore, specific inverse functions or regularization methods are needless, and the use of an inverse filter is straightforward as outlined below:

$$F'(\omega) = G(\omega) \cdot H^{-1}(\omega) = G(\omega) \cdot \frac{1}{H(\omega)} \tag{4.9}$$

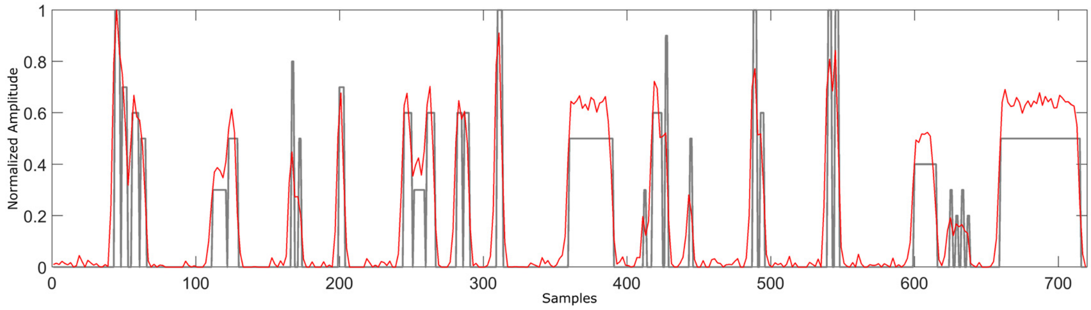

Figure 4.19. Low-resolution subsampled signal of N=360 samples (red) and original test signal (grey).

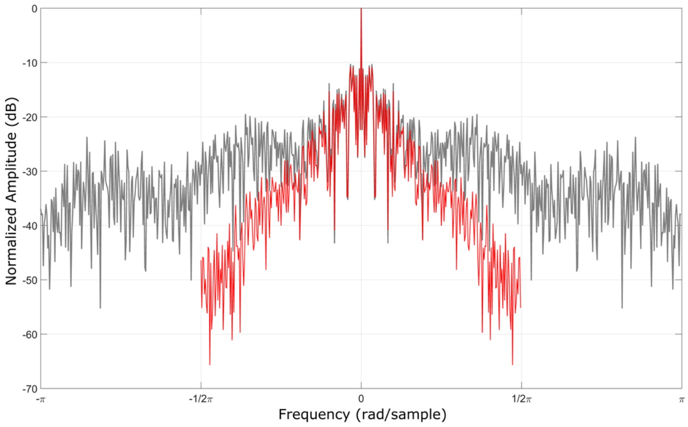

Figure 4.20. Spectrum of the low-resolution subsampled signal (red) compared to original test signal spectrum (grey).

4.6.2. Results

The outcome of implementing the inverse filter is shown in Figure 4.21 (red), together with the signal captured with the high angular resolution antenna (blue) and the original test signal (grey). Even if the information on range (amplitude) is slightly corrupted due to problems associated to the deconvolution process, results are greatly satisfactory regarding target localization and identification or angular resolution. It must be remarked that the results obtained by means of the low angular resolution antenna (BW_{-3dB}=2˚) and scanning intervals of 2 samples (N=360 samples) differs very little from the outcome achieved with the high angular resolution antenna (BW_{-3dB}=0.5˚) and scanning intervals of 1 sample (N=720 samples).

With respect to the spectral components (see Figure 4.22), most of the passband frequencies are successfully recovered, although some high frequencies are slightly overamplified. The spectral components captured by the low angular resolution antenna appear to be enough for a good quality signal reconstruction when applying the post-processing techniques described in the method.

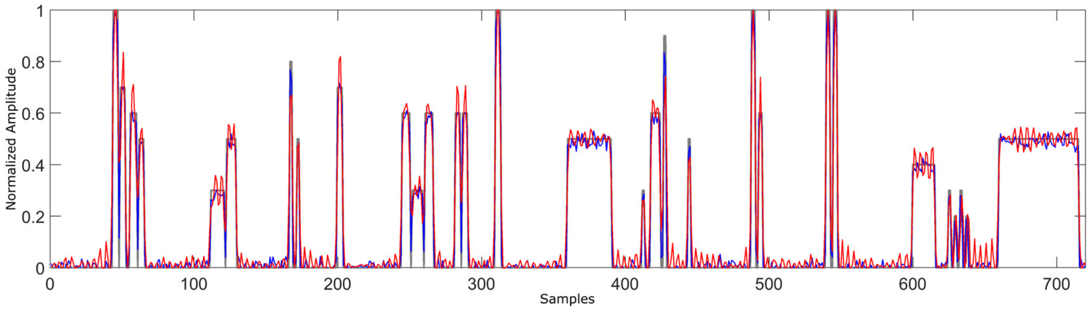

Figure 4.21. Recovered estimation of the original signal (red), signal acquired with BW_{-3dB}=0.5˚ (blue) and original test signal (grey). N=720 samples.

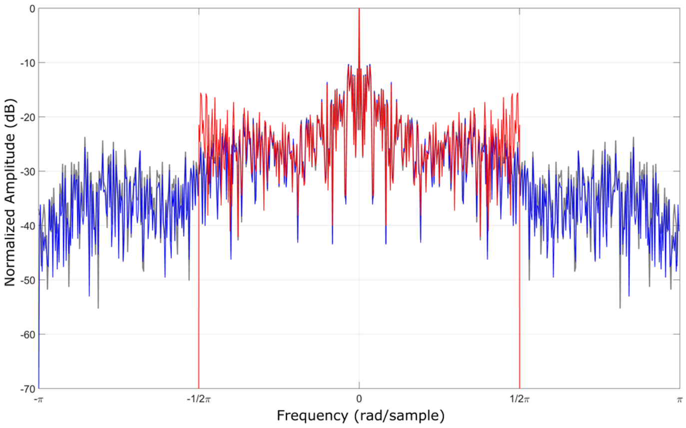

Figure 4.22. Spectra of the recovered signal (red) and the signal acquired with BW_{-3dB}=0.5˚ (blue), compared to the original test signal spectrum (grey).

This section shows once more how significantly the aperture or size of an antenna system can be reduced without any meaningful loss of angular resolution. More specifically, a data capturing process has been simulated using antenna beams of 3 dB beamwidths of up to 0.5 and 2 degrees, achieving quite similar results, even if using a 4 times less directive and smaller aperture size antenna.

In addition, it has been demonstrated how the low-pass filtering effect of the low angular resolution antenna beam makes possible to reduce the sampling rate, i.e., increase the scanning intervals, for subsequent interpolation and inverse filtering, with almost no degradation of the signal quality since the most important information is kept in low frequencies. This reduction of the necessary data points that enable the reconstruction of the signal yields a considerable decrease in the time required to sweep the FOV and could also improve the SNR of the system profiting from time integration techniques. Moreover, the subsampling process helps to avoid stability and noise-amplification problems related to inverse problems, because high-frequency spectral components are truncated.

4.7. Conclusions

The outcomes show that it might be possible to achieve high angular resolution systems using less directive beams, and therefore, smaller effective areas or antenna sizes. Fairly comparable results have been obtained when using antennas up to four times less directive beams, which means that the antenna size (aperture) could also be reduced by a factor of 4 thanks to post-processing techniques. The results are highly satisfactory spatially locating and identifying different size targets in connection with angular resolution. However, in some instances, the range information (amplitude) can be affected as a result of noise amplification problems of inverse problems, mainly when implementing simulations with lower angular resolution antennas.

The low-pass filtering effect produced by antenna beams enables the use of lower sampling rates or, equivalently, larger scanning intervals, while still meeting the Nyquist sampling theorem. This subsampling reduces considerably the data points used to reconstruct high angular resolution signals, since a subsequent interpolation and inverse filtering can be performed with almost no degradation of the signal quality. Consequently, the antenna sweep time can be shortened or, in other cases, the system could take more time in each measurement and improve the SNR of the system or take advantage of time-integration methods, for example. Additionally, subsampling helps to avoid stability and noise-amplification problems related to inverse problems, since high-frequency spectral components are truncated, thus facilitating the implementation of an inverse filtering.

In terms of spectral analysis, high-frequency components attenuated in the data capturing process are mostly recovered, being directly linked with the improvement of angular resolution. Spectral components truncated as a result of the applied inverse functions or due to subsampling are no longer recovered, but most of the frequencies in the passband are successfully recovered. The spectral components kept in the lower frequencies captured by low angular resolution antennas appear to be enough for a highly satisfactory signal reconstruction when applying the post-processing techniques described in the visual hyperacuity simulation method.

It can be said that the proposed approach may have a direct impact on the antenna design process, making it possible to reduce considerably the effective area or aperture, and consequently the antenna size used in many applications, where it is a matter of great importance. This idea could also relax significantly the limitations related to the antenna size and reduces problems associated with the equipment weight, physical dimensions, mechanical scanning difficulties or remote power supply, among others.

Chapter 5

Conclusions and Future Research Lines

upna

Universidad Pública de Navarra
Nafarroako Unibertsitate Publikoa

5.1. Conclusions

This final section aims to provide a general overview of the research work carried out over the previous chapters and summarize the most relevant findings and conclusions.

It seems clear that the human eye shows many parallels and similarities with the conventional digital imaging systems: the structure and dimensions of the optical system, light-sensitive sensors based on the RGB color model, cone densities used for sharp central vision, etc. Conversely, they also have some substantial differences: the area of a cone cell is considerably smaller than the pixel sensors used in imaging devices, which could be a limiting factor when considering the captured photon flux. Nevertheless, the human eye obtains higher dynamic ranges: it is able to see in low-light conditions without the need of long exposure times and it has the ability to avoid saturation in bright environments. But the most striking characteristic is the high-resolution images it can generate thanks to visual hyperacuity: the capability to exceed the limits of resolution established by the number, size and distribution of the photoreceptors. In other words, it largely outperforms the resolution obtained with imaging devices with equivalent characteristics and dimensions.

From this perspective, it is difficult to believe that the eye works under the principles of diffraction-limited systems like most imaging devices. Additionally, the analysis carried out shows that the diffraction produced by the entrance aperture (the pupil) and other contributing factors generates a strongly blurred image over the retina, clearly breaking the Rayleigh criteria. The main hypothesis of this research is based on the fact that the blurring effect produced by diffraction plays a key role in achieving visual hyperacuity: it generates spatial diversity, improves the SNR of the system, makes possible the detection of fine details and relaxes the sampling requirements for data capturing.

The proposed method aims to be an explanation and simulation of the visual hyperacuity, which takes advantage of the introduction of a controlled diffraction to improve the final resolution of signals or images, far from being a limiting factor. The simulation results show that diffraction makes possible the capture of fine details that are lost in absence of diffraction, surpassing the resolution defined by the sensors. This breaks the paradigm of the number of pixel sensors of a given system and the obtained final resolution. The negative note is that the need to implement an inverse filtering process is a complicated matter in many cases: the system can become highly sensitive to the presence of noise or slight modifications in the captured signal, threatening the stability of the whole scheme.

The visual hyperacuity simulation method can deal with many technological challenges of current imaging systems. First of all, some of the hardware-related complications can be faced using signal processing methods and this approach would compensate these limitations with computational load. This is the case of THz imaging, where it is complicated to fabricate devices with a high number of detectors. Therefore, the scheme put forward could be of great help to obtain higher resolution images when the number of available sensors is limited, improve the sensitivity of the system thanks to spatial diversity and replace complex mechanical scanning mechanisms with software-based resolution enhancement techniques. The chance to generate high-resolution images using a low number of sensors makes also possible to increase the size (or area) of each sensor, improving the SNR and the dynamic range of the system. This point can be considered a matter of great importance for vision under poor lighting conditions, the reduction of radiation power in some applications that might be controversial or the increase of the working distance for some specific purposes.

In connection with antenna applications, the results related to angular resolution (spatial location and identification of targets) are highly satisfactory, even if using low directivity antenna beams. However, the range or amplitude information can be slightly affected due to noise amplification and stability problems associated to inverse problems. The low-pass filtering effect produced by the antenna beam can be used as an anti-aliasing filter that allow the reduction of the sampling rate or, equivalently, the captured data points. In any event, the implementation of the proposed method makes possible to obtain high resolution signals, with almost no degradation of the signal quality. Moreover, this subsampling can avoid problems related to inverse problems, since high-frequency spectral components are truncated. The spectral components attenuated in the process of data capturing are mostly recovered, which seem to be enough for improving the final angular resolution.

It has been demonstrated how might be possible to achieve high angular resolution systems using antennas with low directivity beams benefiting, at the same time, from the advantages of smaller effective areas or antenna sizes. The visual hyperacuity simulation method could have a direct repercussion on antenna design and implementations: the reduction of the antenna size could relax significantly the limitations and problems associated with many issues, such as the weight, the general dimensions of the system or the power supply.

5.2. Future Research Lines

Even if a long and hard work has already been done in order to establish the basis of the visual hyperacuity simulation method and its possible applications, it is clear that much remains to be done in this direction.

The multiple tests performed to date are based on software simulations. Therefore, the design, construction and testing of real systems and applications is clearly one of the next steps that should be carried out, both for imaging and antenna systems. Dealing with more realistic approaches would generate new challenges and issues that have not been faced during the simulation phase: the presence of real noise problems and other perturbations in the process of data capturing, the generation of a controlled diffraction, the precise determination of the PSF for an efficient inverse filtering and many other aspects that would arise along the way.

One of the most critical aspect when implementing the method for real applications would be the election of the most appropriate method for solving the inverse problem, since there are many existing approaches in literature. Multiple factors could be considered, such as the nature and power of the diffraction effect, the presence of noise in the system, the resolution enhancement required, the type of images or even the specific application. What is clear is that the algorithm of the method must be computationally efficient, due to the demands of current technological applications, such as real time imaging applications, among many others.

upna

Universidad Pública de Navarra
Nafarroako Unibertsitate Publikoa

Appendix: Testing some Aspects of the Method

This section includes some of the tests carried out from the general method proposed above. These tests are based on the modification of multiple parameters and the application of different deconvolution methods, for the purpose of observing and analyzing the results obtained in each case. Some of the tests have been implemented in 2D using a test pattern image, while others have been performed with 1D signals in order to simplify operations. Notice, that these tests could also be applied to 2D signal or images, operating by rows and columns (or vice versa).

a) The Effect of Variations in the PSF

Deterministic methods require a precise knowledge of both the observation $g[x,y]$ and the kernel or PSF $h[x,y]$. This test consists of introducing a $sinc^2$ type varying-radius diffraction filter (h_1) while the deconvolution is performed by means of a similar filter (h_2), but with a fixed radius. The implementation in the Fourier Transform domain is described as follows:

$$F'[u,v]=F[u,v]\cdot H_1[u,v]\cdot\frac{1}{H_2[u,v]} \tag{A.1}$$

In the example below, the test pattern image shown in Figure A.1 has been filtered using similar $sinc^2$ type diffraction filters (h_1), but with different widths (main lobe radius r of 40, 48, 50, 52 and 60 pixels). The inverse filtering has been carried out in all cases using a filter (h_2) with a fixed radius (main lobe of r=50 pixels).

The results can be observed in Figure A.2. As can be seen, when $h_1=h_2$ (r=50 pixels), the deconvolution is performed successfully. However, when $h_1\neq h_2$, no matter how slightly h_1 it is modified, the result of the deconvolution is not satisfactory. The obtained result shows the importance of determining with high accuracy the diffraction introduced by the PSF when an

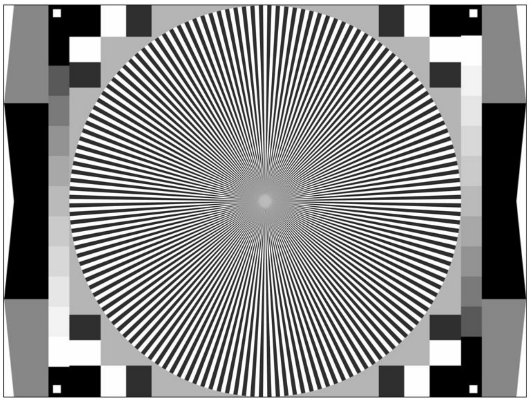

Figure A.1. Original test pattern image.

inverse filtering is needed. In multiple applications, it is not a trivial task and the inverse problem becomes an even more complicated issue.

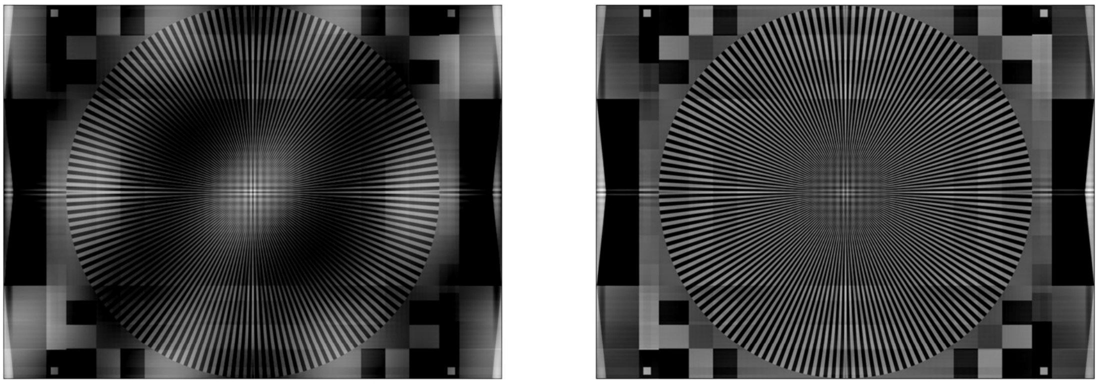

r=40 pixels *r=48 pixels*

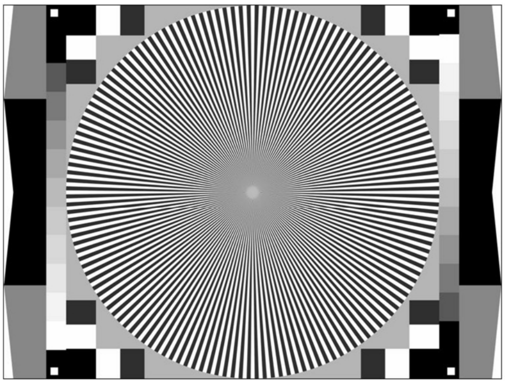

r=50 pixels

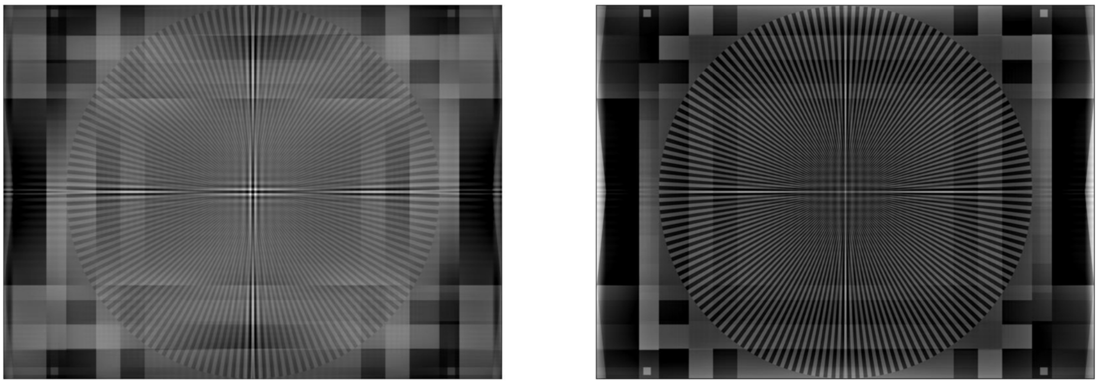

r=52 pixels *r=60 pixels*

Figure A.2. Results of introducing a *sinc*^{2} type varying-radius diffraction filter h_1 with main lobes of 40, 48, 50, 52 and 60 pixels and inversely filtered with a fixed radius filter h_2 of r=50 pixels.

b) TSVD for 1D Signal Deconvolution

In this case, the TSVD will be tested by means of convolution-based methods. Accordingly, the PSF in 1D is transformed into a 2D Toeplitz matrix, necessary to compute the 1D convolution (see Figure A.3).

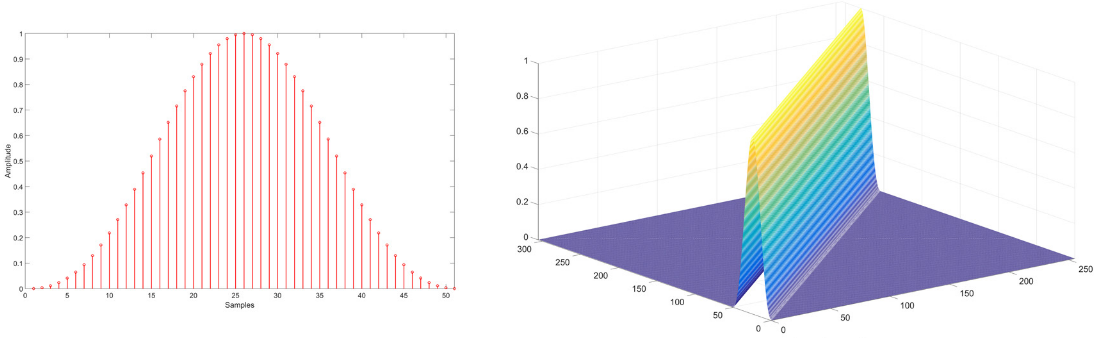

PSF

Toeplitz(PSF)

Figure A.3. 1D PSF and the corresponding Toeplitz matrix.

By a simple matrix-vector multiplication between the original test signal and the Toeplitz matrix of the PSF, the 1D convolution is implemented (Figure A.4). Additionally, some noise has been introduced.

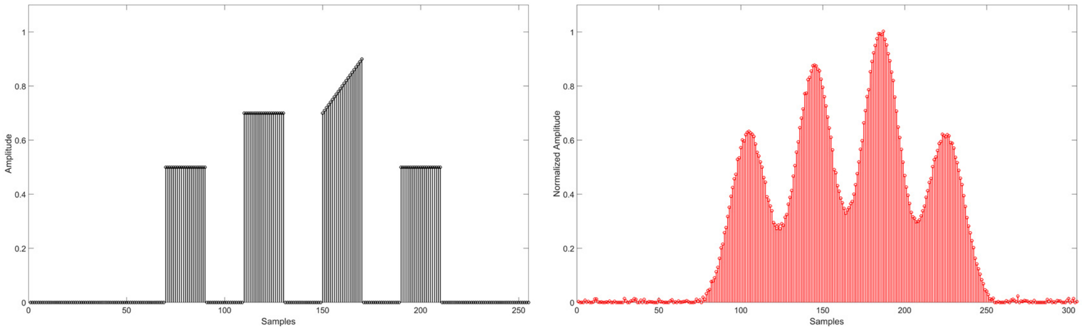

Figure A.4. Original test signal (left) and the blurred and noisy signal (right).

If the Toeplitz matrix is a square matrix, then the inverse can be directly calculated. Nevertheless, when this is not the situation, the inverse function is computed using the formula:

$$H_{inv} = (H^T \cdot H)^{-1} \cdot H^T \tag{A.2}$$

where H is the Toeplitz matrix of the PSF and H^T its transposed matrix. Once again, the deconvolution will be implemented by matrix-vector multiplication. However, the inverse filter cannot be directly applied, since the presence of noise generates important stability problems. Therefore, it is necessary to implement a TSVD regularization, to control the noise amplification matter and stabilize the solution.

The first step is the SVD of the PSF,

$$H = U \cdot S \cdot V^{T} \tag{A.3}$$

where *H* is the Toeplitz matrix of the PSF, *U* and *V* are the left and right singular vectors and *S* is the diagonal matrix containing the singular values (observe Figure A.5).

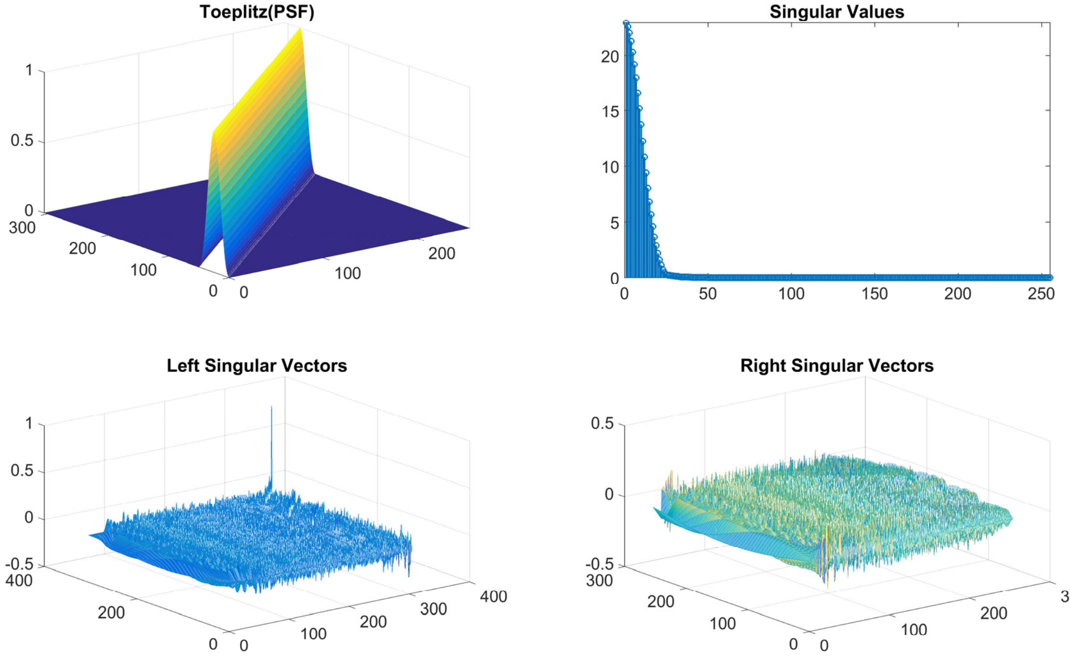

Figure A.5. Singular Value Decomposition of the PSF.

Later, the most unstable singular values are truncated (the smaller ones, corresponding to the high frequencies), while the components related to the most stable singular values (low-frequencies) are reconstructed. Figure A.6 shows the matrices *S*, *U* and *V* when the 50 largest singular values are kept.

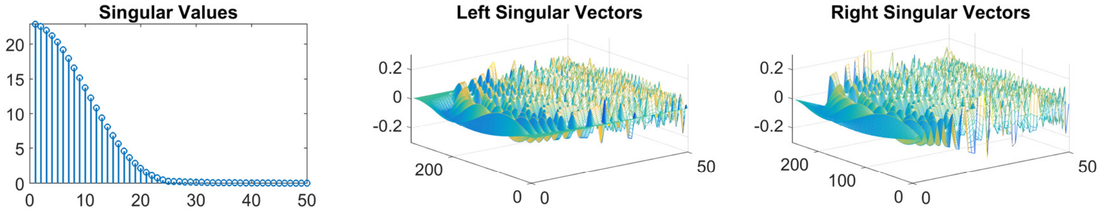

Figure A.6. Truncated singular values and vectors.

The results obtained reconstructing the components corresponding to the 15, 30, 50 and 70 largest singular values are depicted in Figure A.7. Notice how when too many singular values are truncated, the reconstructed signal presents slow and smooth variations, presenting stability against noise but being unable to remove the blur introduced by the PSF. On the contrary, when more singular values are reconstructed, the most unstable components are included in the deconvolution process, producing noise amplification (stability) problems.

It is clear that the choice of the regularization parameter α is critical, considering that it determines which singular values are truncated and, therefore, which components are reconstructed. But this is not a simple issue, since it presents a compromise between the noise suppression and the loss of relevant information.

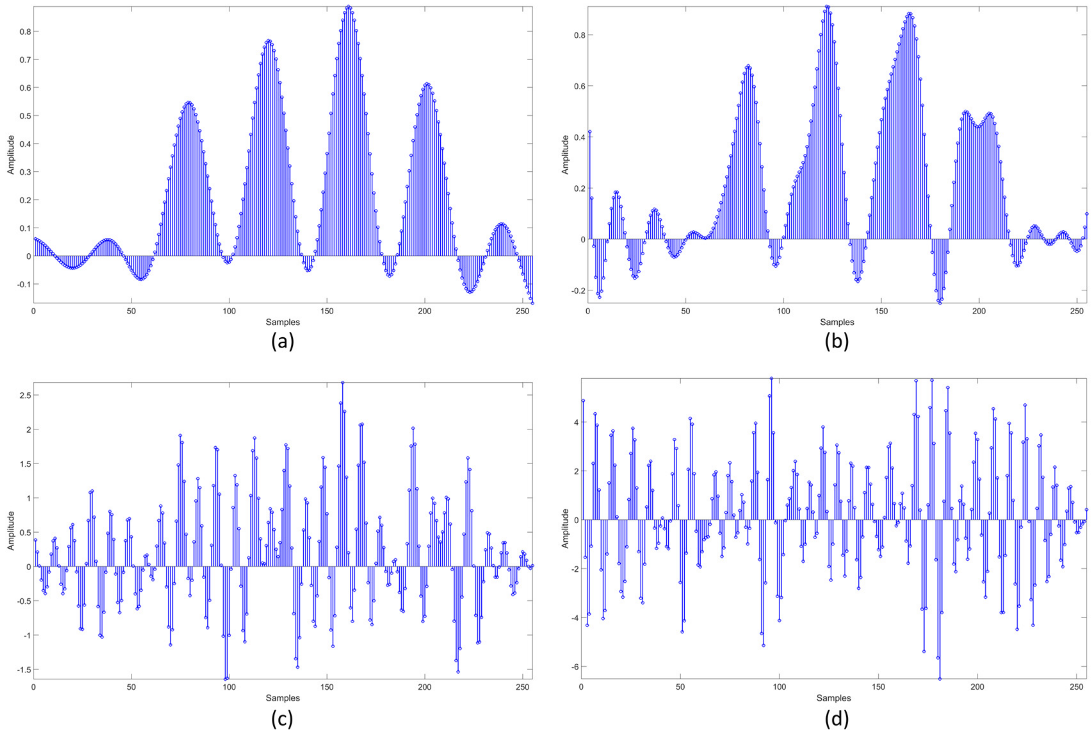

(a) (b)

(c) (d)

Figure A.7. Signal reconstruction by TSVD, including 15 (a), 30 (b), 50 (c) and 70 (d) singular values.

c) Tikhonov Regularization for 1D Signal Deconvolution

Tikhonov regularization aims to find a TSVD solution to $Hf = d$, where the regularized approximation is expressed by:

$$f_\alpha = (H^T H + \alpha I)^{-1} H^T g \quad \text{(A.4)}$$

The regularization parameter α determines the cut-off—or threshold—level of the TSVD filter: when α is too small, the noise is not filtered and f_α is highly oscillatory; by contrast, when α is too large, noise components are filtered out but f_α is excessively smooth. Therefore, it is important to find a compromise solution.

Let us consider the original test signal *f* and the blurred and noisy signal *g* (Figure A.8). The value of α can be determined by minimizing the solution error norm given by $\left\| f_\alpha - f \right\|$ [57], achieving the best possible regularized solution. Figure A.9 shows how the TSVD solution f_α varies with the regularization parameter α. In this case, the optimal solution is obtained for α=0.0389, while oscillating results are obtained when α→0 and the smooth functions when α→1.

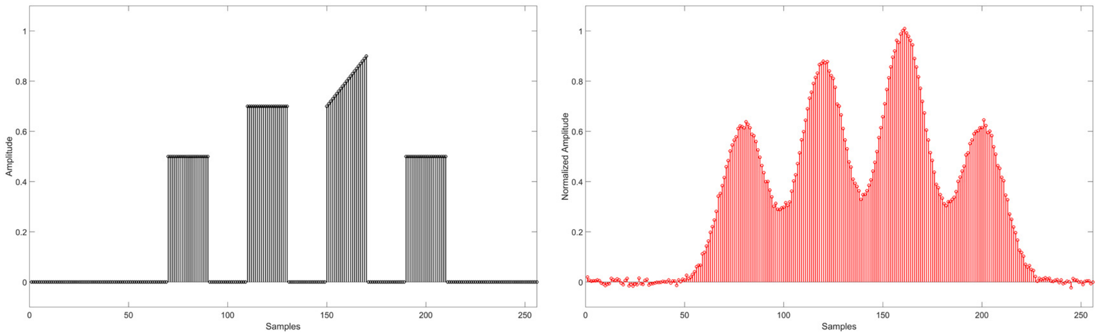

Figure A.8. Original test signal *f* (left) and the blurred and noisy signal *g* (right).

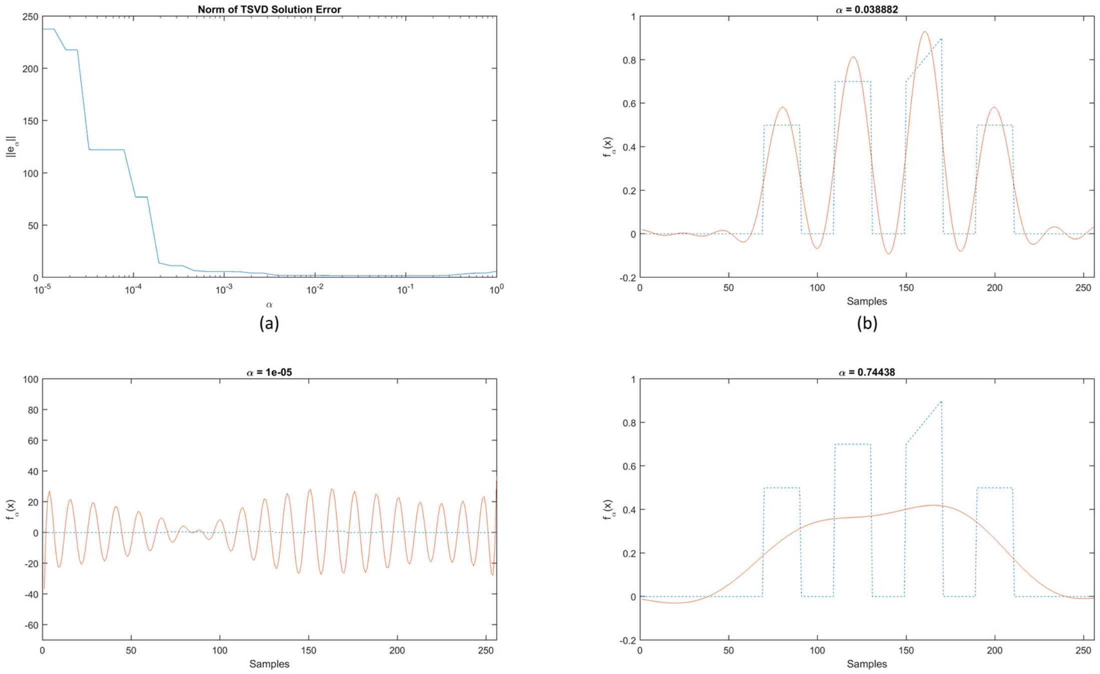

(a) (b)

(c) (d)

Figure A.9. (a) Norm of the solution error, versus the regularization parameter α. (b) f_α for α=0.0389. (c) f_α for α=0.00001. (d) f_α for α=0.7444.

d) Tikhonov Regularization for Image Deconvolution

The Tikhonov regularization method can also be applied to 2D signals or images, using the regularized approximation defined in equation A.4. On this occasion, the original test pattern image has been filtered using a *sinc*^{2} type PSF operating in the Fourier Transform domain and some Gaussian noise has been added to it (Figure A.10).

The blurred and noisy image has been subsampled by means of a factor 2 decimation process and subsequently interpolated (factor 2), creating new data points. The results of reconstructing the image by means of a Tikhonov regularization method can be found below in Figure A.11, when using different values of the regularization parameter α.

Once again, low values of α introduce noisy components in the solution, being difficult to recognize the image. However, larger values of α reduce the effect of noise, but high-frequency components are truncated, obtaining poor results when talking about deblurring.

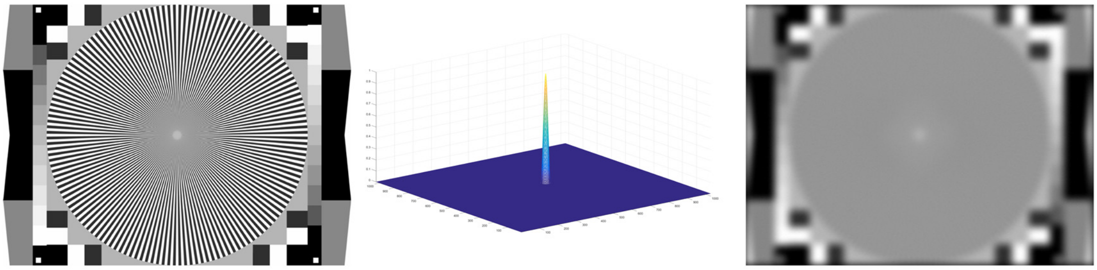
(a) (b) (c)

Figure A.10. (a) Original test pattern image. (b) PSF. (c) Burred and noisy image.

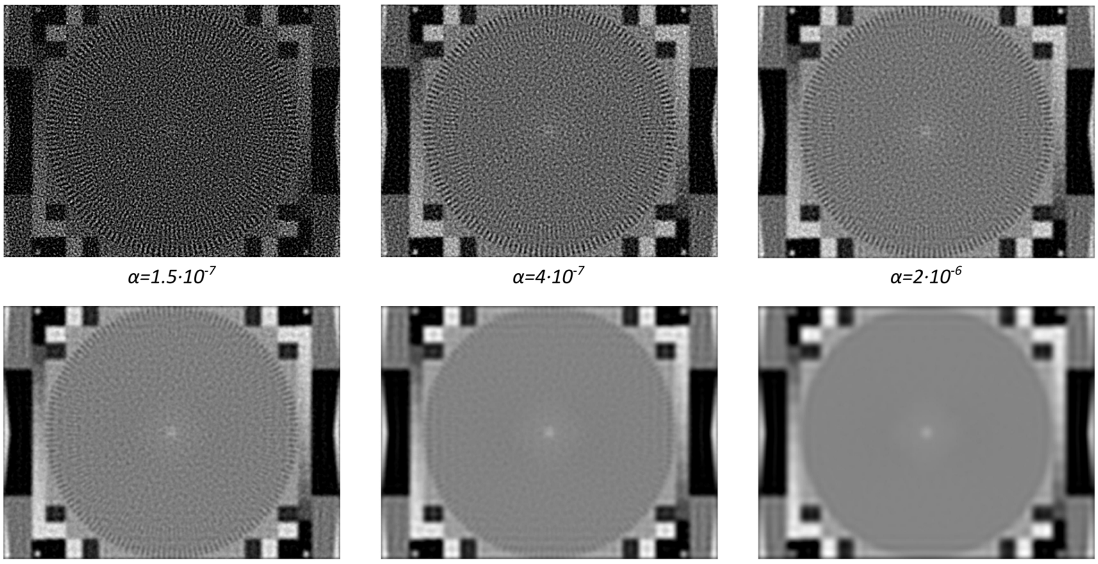
$\alpha=1.5\cdot10^{-7}$ $\alpha=4\cdot10^{-7}$ $\alpha=2\cdot10^{-6}$

$\alpha=4\cdot10^{-5}$ $\alpha=4\cdot10^{-4}$ $\alpha=0.01$

Figure A.11. Results for different values of the regularization parameter α, when applying Tikhonov regularization for image deconvolution.

upna

Universidad Pública de Navarra
Nafarroako Unibertsitate Publikoa

Bibliography

[1] H. Davson, “Human Eye,” *Encyclopædia Britannica, inc.*, 2016. [Online]. Available: https://global.britannica.com/science/human-eye. [Accessed: 10-Jan-2017].

[2] S. N. Fyodorov, M. A. Galin, and A. Linksz, “Calculation of the optical power of intraocular lenses,” *Invest. Ophthalmol. Vis. Sci.*, vol. 14, no. 8, pp. 625–628, 1975.

[3] American Academy of Ophthalmology, *Basic and Clinical Science Course (BCSC), Section 11: Lens and Cataract*. San Francisco: American Academy of Ophthalmology, 2016.

[4] H. Kolb, “How the Retina Works,” *Am. Sci.*, vol. 91, no. 1, pp. 28–35, 2003.

[5] H. Kolb, E. Fernandez, and R. Nelson, *Webvision. The Organization of the Retina and Visual System*. University of Utah Health Sciences Center, 1995.

[6] C. A. Curcio, K. R. Sloan, R. E. Kalina, and A. E. Hendrickson, “Human photoreceptor topography,” *J. Comp. Neurol.*, vol. 292, no. 4, pp. 497–523, Feb. 1990.

[7] E. Hecht, *Optics*. Addison-Wesley, 2002.

[8] K. Matsumoto, T. Nakamura, A. Yusa, and S. Nagai, “A New MOS Phototransistor Operating in a Non-Destructive Readout Mode,” *Jpn. J. Appl. Phys.*, vol. 24, no. Part 2, No. 5, pp. L323–L325, May 1985.

[9] E. R. Fossum, “Active pixel sensors: are CCDs dinosaurs?,” in *IS&T/SPIE’s Symposium on Electronic Imaging: Science and Technology*, 1993, vol. 1900, pp. 2–14.

[10] D. Litwiller, “CCD vs. CMOS: Facts adn Fiction,” *Photonics Spectra*, vol. 35, no. 1, pp. 154–158, 2001.

[11] European Machine Vision Association., “EMVA Standard 1288 Standard, Standard for Characterization of Image Sensors and Cameras,” 2012.

[12] Point Grey, “Color Camera Sensor Review Q2 2016,” 2016.

[13] H. R. Blackwell, “Contrast Thresholds of the Human Eye,” *J. Opt. Soc. Am.*, vol. 36, no. 11, pp. 624–643, 1946.

[14] T. Ivergard and B. Hunt, *Handbook of control room design and ergonomics: a perspective for the future*, 2nd ed. Boca Raton, New York, London: CRC Press, 2008.

[15] E. F. Schubert, *Light-Emitting Diodes*, 2nd ed. New York: Cambridge University Press, 2006.

[16] J. Guo and S. Sonkusale, “A High Dynamic Range CMOS Image Sensor for Scientific Imaging Applications,” *IEEE Sens. J.*, vol. 9, no. 10, pp. 1209–1218, Oct. 2009.

[17] M. Chen, Y. Liu, Z. Li, J. Xiao, and J. Chen, “A High Dynamic Range CMOS Readout Chip for Electrochemical Sensors,” *IEEE Sens. J.*, vol. 16, no. 10, pp. 3504–3513, May 2016.

[18] S. Vargas-Sierra, G. Linán-Cembrano, and A. Rodríguez-Vázquez, “A 151 dB High Dynamic Range CMOS Image Sensor Chip Architecture With Tone Mapping Compression Embedded In-Pixel,” *IEEE Sens. J.*, vol. 15, no. 1, pp. 180–195, Jan. 2015.

[19] G. A. Osterberg, “Topography of the layer of rods and cones in the human retina,” *Acta Ophthalmol.*, vol. 13, no. S6, pp. 11–103, 1935.

[20] G. Westheimer, “Visual Acuity and Hyperacuity,” *Invest. Ophthalmol.*, vol. 64, no. 8, pp. 570–572, 1975.

[21] J. B. Benson, G. P. Luke, C. H. G. Wright, and S. F. Barrett, “Pre-blurred spatial sampling can lead to hyperacuity,” *2009 IEEE 13th Digit. Signal Process. Work. 5th IEEE Signal Process. Educ. Work. DSP/SPE 2009, Proc.*, pp. 570–575, 2009.

[22] G. Westheimer, “Diffraction theory and visual hyperacuity,” *Am. J. Optom. Physiol. Opt.*, vol. 53, no. 7, pp. 362–364, 1976.

[23] G. Westheimer and S. P. McKee, “Spatial configurations for visual hyperacuity,” *Vision Res.*, vol. 17, no. 8, pp. 941–947, 1977.

[24] T. Carney and S. A. Klein, “Resolution acuity is better than vernier acuity,” *Vision Res.*, vol. 37, no. 5, pp. 525–539, 1997.

[25] H. Hartridge, “Visual acuity and the resolving power of the eye,” *J. Physiol.*, vol. 57, no. 1–2, pp. 52–67, Dec. 1922.

[26] S. A. Klein and D. M. Levi, “Hyperacuity thresholds of 1 sec: theoretical predictions and empirical validation,” *J. Opt. Soc. Am. A.*, vol. 2, no. 7, pp. 1170–1190, 1985.

[27] J. Yang and T. Huang, “Image super-resolution: Historical overview and future challenges,” *Super-resolution imaging*, pp. 20–34, 2010.

[28] L. Yue, H. Shen, J. Li, Q. Yuan, H. Zhang, and L. Zhang, “Image super-resolution: The techniques, applications, and future,” *Signal Processing*, vol. 128, pp. 389–408, 2016.

[29] H. L. Averill and F. W. Weymouth, “Visual perception and the retinal mosaic. II. The influence of eye-movements on the displacement threshold.,” *J. Comp. Psychol.*, vol. 5, no. 2, pp. 147–176, 1925.

[30] W. H. Marshall and S. A. Talbot, *Recent evidence for neural mechanisms in vision leading to a general theory of sensory acuity.* Jacques Cattell, 1942.

[31] M. H. Hennig and F. Wörgötter, “Eye Micro-movements Improve Stimulus Detection Beyond the Nyquist Limit in the Peripheral Retina,” in *Advances in Neural Information Processing Systems 16*, 2004, pp. 1475–1482.

[32] S. Martinez-Conde, S. L. Macknik, and D. H. Hubel, “The role of fixational eye movements in visual perception,” *Nat. Rev. Neurosci. Neurosci.*, vol. 5, no. 3, pp. 229–232, 2004.

[33] M. Rucci, R. Iovin, M. Poletti, and F. Santini, “Miniature eye movements enhance fine spatial detail.,” *Nature*, vol. 447, no. 7146, pp. 851–854, 2007.

[34] H.-K. Ko, M. Poletti, and M. Rucci, “Microsaccades precisely relocate gaze in a high visual acuity task.,” *Nat. Neurosci.*, vol. 13, no. 12, pp. 1549–1553, 2010.

[35] H. B. Barlow, “Reconstructing the visual image in space and time.,” *Nature*, vol. 279, no. 5710, pp. 189–90, May 1979.

[36] W. S. Geisler, “Physical limits of acuity and hyperacuity.,” *J. Opt. Soc. Am. A.*, vol. 1, no. 7, pp. 775–782, 1984.

[37] X. Pitkow, H. Sompolinsky, and M. Meister, “A neural computation for visual acuity in the presence of eye movements,” *PLoS Biol.*, vol. 5, no. 12, pp. 2898–2911, 2007.

[38] J. Y. Lee and S. N. Hwang, “A theory on constructing a hyper-acuity electronic device,” *Trans. Korean Inst. Electr. Eng.*, vol. 57, no. 6, pp. 982–984, 2008.

[39] S. Zozor, P.-O. Amblard, and C. Duchêne, “Does eye tremor provide the hyperacuity phenomenon?,” *J. Stat. Mech. Theory Exp.*, vol. 2009, no. 1, p. P01015, 2009.

[40] A. Sommerfeld, *Lectures on Theoretical Physics: Optics*. New York: Academic Press, 1954.

[41] C. Huygens, *Traité de la lumiere*. Leiden, The Netherlands, 1960.

[42] J. W. Goodman, *Introduction to Fourier Optics*, 3rd ed. Englewood, Colorado: Roberts & Company Publishers, 2005.

[43] G. B. Airy, "On the Diffraction of an Object-glass with Circular Aperture," *Trans. Cambridge Philos. Soc.*, vol. 5, pp. 283–291, 1835.

[44] P. K. Ahnelt, H. Kolb, and R. Pflug, "Identification of a subtype of cone photoreceptor, likely to be blue sensitive, in the human retina," *J. Comp. Neurol.*, vol. 255, no. 1, pp. 18–34, Jan. 1987.

[45] L. A. Levin and F. H. Adler, *Adler's Physiology of the Eye*, 11th ed. New York: Saunders Elsevier, 2011.

[46] A. L. Yarbus, *Eye movements and vision*. New York, 1967.

[47] L. A. Riggs, F. Ratliff, J. C. Cornsweet, and T. N. Cornsweet, "The Disappearance of Steadily Fixated Visual Test Objects*," *J. Opt. Soc. Am.*, vol. 43, no. 6, p. 495, Jun. 1953.

[48] F. Ratliff and L. A. Riggs, "Involuntary motions of the eye during monocular fixation," *J. Exp. Psychol.*, vol. 40, no. 6, pp. 687–701, 1950.

[49] S. Martinez-Conde, S. L. Macknik, and D. H. Hubel, "Microsaccadic eye movements and firing of single cells in the striatecortex of macaque monkeys," *Nat. Neurosci.*, vol. 3, no. 3, pp. 251–258, Mar. 2000.

[50] R. W. Ditchburn, "The function of small saccades.," *Vision Res.*, vol. 20, no. 3, pp. 271–2, 1980.

[51] R. S. Harwerth, P. M. Fredenburg, and E. L. Smith, "Temporal integration for stereoscopic vision," *Vision Res.*, vol. 43, no. 5, pp. 505–517, 2003.

[52] J. L. Harris, "Diffraction and Resolving Power," *J. Opt. Soc. Am.*, vol. 54, no. 7, pp. 931–963, 1964.

[53] C. W. Barnes, "Object Restoration in a Diffraction-Limited Imaging System," *J. Opt. Soc. Am.*, vol. 56, no. 5, pp. 575–578, 1966.

[54] K. G. Birch, "Spatial filtering in optical data-processing," *Reports Prog. Phys.*, vol. 35, no. 3, pp. 1265–1314, 2002.

[55] Y. Kamitani and Y. Sawahata, "Spatial smoothing hurts localization but not information: Pitfalls for brain mappers," *Neuroimage*, vol. 49, no. 3, pp. 1949–1952, 2010.

[56] L. J. Gelius and E. Asgedom, "Diffraction-limited imaging and beyond - the concept of super resolution," *Geophys. Prospect.*, vol. 59, no. 3, pp. 400–421, 2011.

[57] C. R. Vogel, *Computational Methods for Inverse Problems*. Society for Industrial and Applied Mathematics, 2002.

[58] M. Bertero and P. Boccacci, *Introduction to Inverse Problems in Imaging*. IOP Publishing Ltd, 1998.

[59] S. Berisha and J. G. Nagy, "Iterative methods for image restoration," *Acad. Press Libr. Signal Process.*, vol. 4, pp. 193–247, 2013.

[60] C. E. Shannon, "Communication in the Presence of Noise," *Proc. IRE*, vol. 37, no. 1, pp. 10–21, Jan. 1949.

[61] T. Engin Tuncer, "A New Method for D-Dimensional Exact Deconvolution," *IEEE Trans. Signal Process.*, vol. 47, no. 5, pp. 1324–1334, 1999.

[62] D. Zazula and L. Gyergyek, "Direct Frequency-Domain Deconvolution when the Signals Have No Spectral Inverse," *IEEE Trans. Signal Process.*, vol. 41, no. 2, pp. 977–981, 1993.

[63] C. Sanchez-Avila, “An adaptive regularized method for deconvolution of signals with edges by convex projections,” *IEEE Trans. Signal Process.*, vol. 42, no. 7, pp. 1849–1851, Jul. 1994.

[64] H. C. Andrews and B. R. Hunt, *Digital Image Restoration*. Prentice-Hall, 1977.

[65] T. K. Sarkar, F. I. Tseng, S. M. Rao, S. A. Dianat, and B. Z. Hollmann, “Deconvolution of Impulse Response from Time-Limited Input and Output: Theory and Experiment,” *IEEE Trans. Instrum. Meas.*, vol. IM-34, no. 4, pp. 541–546, Dec. 1985.

[66] I. Transactions, “Time domain deconvolution when the kernal has no spectral inverse,” *IEEE Trans. Acoust.*, vol. 34, no. 4, pp. 912–918, 1986.

[67] J. S. Lim and A. V. Oppenheim, *Advanced topics in signal processing*. Prentice-Hall, 1988.

[68] N. E. Mastorakis and S. M. Ieee, “On the Design of 2-D Inverse and 2-D Wiener Filters,” pp. 206–209.

[69] H. Marmolin, S. Nyberg, and U. Berggrund, “A Visually Optimized Restoring Filter,” *Photogr. Sci. Eng.*, vol. 22, no. 3, pp. 142–147, 1978.

[70] A. Ahlen and M. Sternad, “Wiener filter design using polynomial equations,” *IEEE Trans. Signal Process.*, vol. 39, no. 11, pp. 2387–2399, 1991.

[71] A. Ahlén and M. Sternad, “Optimal Deconvolution Based On Polynomial Methods,” *IEEE Trans. Acoust.*, vol. 37, no. 2, pp. 217–226, 1989.

[72] M. J. Grimble and A. El Sayed, “Solution of the H optimal linear filtering problem for discrete-time systems,” vol. 38, no. 7, pp. 1092–1104, 1978.

[73] P. C. Hansen, “Deconvolution and regularization with Toeplitz matrices,” *Numer. Algorithms*, vol. 29, pp. 323–378, 2002.

[74] D. L. Phillips, “A Technique for the Numerical Solution of Certain Integral Equations of the First Kind,” *J. ACM*, vol. 9, no. 1, pp. 84–97, 1962.

[75] Tikhonov A., “Solution of Incorrectly Formulated Problems and the Regularization Method,” *Sov. Math. Dokl.*, vol. 5, p. 1035/1038, 1963.

[76] M. Hanke, J. G. Nagy, and C. Vogel, “Quasi-Newton approach to nonnegative image restorations,” *Linear Algebra Appl.*, vol. 316, no. 1–3, pp. 223–236, 2000.

[77] J. Biemond, R. L. Lagendijk, and R. M. Mersereau, “Iterative methods for image deblurring,” vol. 78, no. 5, 1990.

[78] J. G. Nagy, K. Palmer, and L. Perrone, “Iterative methods for image deblurring: a Matlab object-oriented approach,” *Numer. Algorithms*, vol. 36, no. 1, pp. 73–93, 2004.

[79] M. Benzi, “Preconditioning Techniques for Large Linear Systems: A Survey,” *J. Comput. Phys.*, vol. 182, no. 2, pp. 418–477, Nov. 2002.

[80] A. Greenbaum, *Iterative Methods for Solving Linear Systems*. Society for Industrial and Applied Mathematics, 1997.

[81] M. Hanke and J. G. Nagy, “Restoration of atmospherically blurred images by symmetric indefinite conjugate gradient techniques,” *Inverse Probl.*, vol. 12, no. 2, pp. 157–173, 1999.

[82] M. Hanke, J. G. Nagy, and R. J. Plemmons, “Preconditioned iterative regularization for ill-posed problems,” *Numerical linear algebra*. pp. 141–163, 1992.

[83] P. H. van Cittert, “Zum Einfluß der Spaltbreite auf die Intensitätsverteilung in Spektrallinien. II,” *Zeitschrift für Phys.*, vol. 69, no. 5–6, pp. 298–308, May 1931.

[84] W. H. Richardson, “Bayesian-based iterative method of image restoration,” *J. Opt. Soc. Am. A*, vol. 62, no. 1, pp. 55–59, 1972.

[85] L. B. Lucy, “An iterative technique for the rectification of observed distributions,” *Astron. J.*, vol. 79, pp. 745–749, 1974.

[86] D. A. Fish, A. M. Brinicombe, E. R. Pike, J. G. Walker, and R. L. Algorithm, “Blind deconvolution by means of the Richardson – Lucy algorithm,” *J. Opt. Soc. Am.*, vol. 12, no. 1, 1995.

[87] S. C. Park, M. K. Park, and M. G. Kang, “Super-resolution image reconstruction: A technical overview,” *IEEE Signal Process. Mag.*, vol. 20, no. 3, pp. 21–36, 2003.

[88] M. Ben-Ezra, A. Zomet, and S. K. Nayar, “Video super-resolution using controlled subpixel detector shifts,” *IEEE Trans. Pattern Anal. Mach. Intell.*, vol. 27, no. 6, pp. 977–987, Jun. 2005.

[89] L. Zhang, H. Zhang, H. Shen, and P. Li, “A super-resolution reconstruction algorithm for surveillance images,” *Signal Processing*, vol. 90, no. 3, pp. 848–859, Mar. 2010.

[90] M. W. Thornton, P. M. Atkinson, and D. A. Holland, “Sub-pixel mapping of rural land cover objects from fine spatial resolution satellite sensor imagery using super-resolution pixel-swapping,” *Int. J. Remote Sens.*, vol. 27, no. 3, pp. 473–491, Feb. 2006.

[91] K. G. Puschmann and F. Kneer, “On super-resolution in astronomical imaging,” *Astron. Astrophys.*, vol. 436, no. 1, pp. 373–378, Jun. 2005.

[92] S. L. Borison, S. B. Bowling, and K. M. Cuomo, “Super-Resolution Methods for Wideband Radar,” *Lincoln Lab. J.*, vol. 5, pp. 441--462, 1992.

[93] M. A. Tehrani, J. J. Laurin, and Y. Savaria, “Angular superresolution algorithm for frequency scanning array antennas,” in *IEEE National Radar Conference - Proceedings*, 2013, no. 1, pp. 4–7.

[94] H. Greenspan, G. Oz, N. Kiryati, and S. Peled, “MRI inter-slice reconstruction using super-resolution,” *Magn. Reson. Imaging*, vol. 20, no. 5, pp. 437–446, Jun. 2002.

[95] Jiali Cui, Yunhong Wang, JunZhou Huang, Tieniu Tan, and Zhenan Sun, “An iris image synthesis method based on PCA and super-resolution,” in *Proceedings of the 17th International Conference on Pattern Recognition, 2004. ICPR 2004.*, 2004, p. 471–474 Vol.4.

[96] H. Huang, H. He, X. Fan, and J. Zhang, “Super-resolution of human face image using canonical correlation analysis,” *Pattern Recognit.*, vol. 43, no. 7, pp. 2532–2543, Jul. 2010.

[97] R. K. Mantiuk, K. Myszkowski, and H.-P. Seidel, “High Dynamic Range Imaging,” in *Wiley Encyclopedia of Electrical and Electronics Engineering*, Hoboken, NJ, USA: John Wiley & Sons, Inc., 2015, pp. 1–42.

[98] F. Banterle, A. Artusi, K. Debattista, and A. Chalmers, *Advanced High Dynamic Range Imaging: Theory and Practice*. CRC press, 2011.

[99] D. R. DeBoer, R. G. Gough, J. D. Bunton, T. J. Cornwell, R. J. Beresford, S. Johnston, I. J. Feain, A. E. Schinckel, C. A. Jackson, M. J. Kesteven, A. Chippendale, G. A. Hampson, J. D. O’Sullivan, S. G. Hay, C. E. Jacka, T. W. Sweetnam, M. C. Storey, L. Ball, and B. J. Boyle, “Australian SKA Pathfinder: A High-Dynamic Range Wide-Field of View Survey Telescope,” *Proc. IEEE*, vol. 97, no. 8, pp. 1507–1521, Aug. 2009.

[100] C. Sirtori, “Applied physics: Bridge for the terahertz gap,” *Nature*, vol. 417, no. 6885, pp. 132–133, May 2002.

[101] B. B. Hu and M. C. Nuss, “Imaging with terahertz waves,” *Opt. Lett.*, vol. 20, no. 16, p. 1716, Aug. 1995.

[102] C. Jansen, S. Wietzke, O. Peters, M. Scheller, N. Vieweg, M. Salhi, N. Krumbholz, C. Jördens, T. Hochrein, and M. Koch, “Terahertz imaging: applications and perspectives,” *Appl. Opt.*, vol. 49, no. 19, p. E48, Jul. 2010.

[103] J. C. Iriarte, D. Etayo, I. Palacios, I. Maestrojuan, I. Liberal, a. Rebollo, J. Teniente, I. Ederra, and R. Gonzalo, “Water content evolution in leaves based on active THz imaging system,” *Proc. 5th Eur. Conf. Antennas Propag.*, pp. 1049–1050, 2011.

[104] V. Torres, I. Palacios, J. C. Iriarte, I. Liberal, L. G. Santesteban, C. Miranda, J. B. Royo, and R. Gonzalo, “Monitoring Water Status of Grapevine by Means of THz Waves,” *J. Infrared, Millimeter, Terahertz Waves*, vol. 37, no. 5, pp. 507–513, 2016.

[105] V. Petrov, A. Pyattaev, D. Moltchanov, and Y. Koucheryavy, “Terahertz band communications: Applications, research challenges, and standardization activities,” in *2016 8th International Congress on Ultra Modern Telecommunications and Control Systems and Workshops (ICUMT)*, 2016, pp. 183–190.

[106] S.-H. Ding, Q. Li, R. Yao, and Q. Wang, “High-resolution terahertz reflective imaging and image restoration.,” *Appl. Opt.*, vol. 49, no. 36, pp. 6834–9, 2010.

[107] J. Zhao, W. Chu, L. Guo, Z. Wang, J. Yang, W. Liu, Y. Cheng, and Z. Xu, “Terahertz imaging with sub-wavelength resolution by femtosecond laser filament in air,” *Sci. Rep.*, vol. 4, no. January, p. 3880, 2014.

[108] J. Lizarraga and C. Del-Rio, “Resolution capabilities of future THz cameras,” *Radioengineering*, vol. 20, no. 2, pp. 373–379, 2011.

[109] R. Appleby and H. B. Wallace, “Standoff Detection of Weapons and Contraband in the 100 GHz to 1 THz Region,” *IEEE Trans. Antennas Propag.*, vol. 55, no. 11, pp. 2944–2956, Nov. 2007.

[110] H. Quast and T. Loffler, “Towards real-time active THz range imaging for security applications,” in *2009 International Conference on Electromagnetics in Advanced Applications*, 2009, pp. 501–504.

[111] Lord Rayleigh, “Investigations in optics, with special reference to the spectroscope,” *Philos. Mag. Ser. 5*, vol. 8, no. 49, pp. 261–274, Oct. 1879.

[112] M. A. Richards, “Iterative noncoherent angular superresolution (radar),” in *Proceedings of the 1988 IEEE National Radar Conference*, 1988, pp. 100–105.

[113] R. Birk, W. Camus, E. Valenti, and W. J. McCandless, “Synthetic Aperture Radar Imaging Systems,” *IEEE AES Syst. Mag.*, no. November, 1995.

[114] P. Snoeij, E. Attema, A. Pietropaolo, V. Mastroddi, M. L’Abbate, and C. Bruno, “Analysis of Sentinel-1 mission capabilities,” in *2009 IEEE International Geoscience and Remote Sensing Symposium*, 2009, vol. 1, p. I-40-I-43.

[115] J. A. Tauber, “The Planck mission,” in *Advances in Space Research*, 2004, vol. 34, no. 3, pp. 491–496.

[116] P. A. Castleberg and K. M. Xilouris, “The Arecibo Observatory,” *IEEE Potentials*, vol. 16, no. 3, pp. 33–35, 1997.

[117] M. Meeks, J. Ball, and A. Hull, “The pointing calibration of the Haystack antenna,” *IEEE Trans. Antennas Propag.*, vol. 16, no. 6, pp. 746–751, Nov. 1968.

[118] G. Tofani, G. Alvito, R. Ambrosini, P. Bolli, C. Bortolotti, L. Bruca, F. Buffa, A. Cattani, G. Comoretto, A. Cremonini, L. Cresci, N. D’Amico, G. L. Deiana, A. Fara, L. Feretti, F. Fiocchi, E. Flamini, F. Fusi Pecci, G. Grueff, G. Maccaferri, A. Maccaferri, F. Mantovani, S. Mariotti, C. Migoni, F. Messina, J. Monari, M. Morsiani, M. Murgia, J. Musmeci, M. Nanni, V. Natale, A. Navarrini, M. Negusini, R. Nesti, L. Olmi, A. Orfei, A. Orlati, F. Palla, D. Panella, C. Pernechele, S. Pilloni, T. Pisanu, A. Poddighe, M. Poloni, A. Poma, S. Poppi, I. Porceddu, I. Prandoni, J. Roda, M. Roma, P. Sarti, A. Scalambra, F. Schillirò, A. Tarchi, G. P. Vargiu, and G. Zacchiroli, “Status of the Sardinia Radio Telescope project,” in *Ground-based and Airborne Telescopes II.*, 2008, vol. 7012, p. 70120F.

[119] G. Marchiori and F. Rampini, “The European ALMA project: design, manufacturing and performances,” in *Proceedings of the Fourth European Conference on Antennas and Propagation*, 2010, pp. 1–4.

[120] P. J. Napier, A. R. Thompson, and R. D. Ekers, “The very large array: Design and performance of a modern synthesize radio telescope,” *Proc. IEEE*, vol. 71, no. 11, pp. 1295–1320, 1983.

[121] Y. Huang, Y. Zha, and J. Yang, “A truncated singular value decomposition method for angular super-resolution in scanning radar,” in *2015 IEEE International Geoscience and Remote Sensing Symposium (IGARSS)*, 2015, pp. 3560–3563.

[122] Y. Zha, Y. Huang, J. Yang, J. Wu, Y. Zhang, and H. Yang, “An improved Richardson-Lucy algorithm for radar angular super-resolution,” in *IEEE National Radar Conference - Proceedings*, 2014, pp. 406–410.

[123] S. Pivnenko and C. Rizzo, “Advanced data post-processing in modern antenna measurements,” in *2016 22nd International Conference on Applied Electromagnetics and Communications (ICECOM)*, 2016.

List of Publications

Contributions to international journals:

[1] A. Lagunas, O. Domínguez, S. Martinez-Conde, S. L. Macknik, and C. del-Río, “Human Eye Visual Hyperacuity: A New Paradigm for Sensing,” under consideration in *Journal of Applied Physics*. [*submitted for publication*]

[2] A. Lagunas, O. Dominguez, and C. del Rio, “A Critical Review of Angular Resolution vs. Beamwidth in Antenna Systems,” under consideration in *IEEE NEMO2017 Mini-Special Issue in IEEE Transactions on Microwave Theory and Techniques*. [*submitted for publication*]

Contributions to international conferences:

[1] C. del Rio, O. Dominguez, D. Moneo, and A. Lagunas, “Applications of Hyperacuity to antenna systems,” in *36th ESA Antenna Workshop on “Antennas and RF Systems for Space Science”*, Noordwijk, Netherlands, 2015.

[2] A. Lagunas, O. Dominguez, and C. del Rio, “Diffraction as a resolution enhancer: Visual hyperacuity simulation method,” in *2016 22nd International Conference on Applied Electromagnetics and Communications (ICECOM)*, Dubrovnik, Croatia, 2016, pp. 1–6.

[3] A. Lagunas, O. Dominguez, and C. del Rio, “Hyperacuity in antenna systems,” in *2016 22nd International Conference on Applied Electromagnetics and Communications (ICECOM)*, Dubrovnik, Croatia, 2016, pp. 1–4.

[4] A. Lagunas, O. Dominguez, and C. del Rio, “A Critical Review of Angular Resolution vs. Beamwidth in Antenna Systems,” presented at the *2017 IEEE MTT-S International Conference on Numerical Electromagnetic and Multiphysics Modeling and Optimization for RF, Microwave, and Terahertz Applications*, Seville, Spain, 2017.

[5] A. Lagunas, O. Dominguez, and C. del Rio, “4x Reduction in Antenna Size without Angular Resolution Loss,” in *38th ESA Antenna Workshop on “Innovative Antenna Systems and Technologies for Future Space Missions”*, Noordwijk, Netherlands, 2017. [*submitted for publication*]

Contributions to national conferences:

[1] C. del Rio, O. Domínguez, A. Lagunas, and D. Moneo, “Aplicaciones de la Hyperacuity del ojo humano a sistemas de antenas,” *XXXI Simposium Nacional de la Unión Científica Internacional de Radio (URSI 2015)*, 2015.

upna

Universidad Pública de Navarra
Nafarroako Unibertsitate Publikoa